

Light scattering and roughness analysis of optical surfaces and thin films

Dissertation
zur Erlangung des akademischen Grades

doctor rerum naturalium (Dr. rer. nat.)

vorgelegt dem Rat der Physikalisch-Astronomischen-Fakultät
der Friedrich-Schiller-Universität Jena

von Dipl.-Phys. Tobias Herffurth
geboren am 24.03.1984 in Apolda

Gutachter:

1. Prof. Dr. rer. nat. habil. Andreas Tünnermann (Friedrich-Schiller-Universität, Jena)
2. Prof. Dr. rer. nat. habil. Richard Kowarschick (Friedrich-Schiller-Universität, Jena)
3. Prof. RNDr. Miloslav Ohlídal, CSc. (Brno University of Technology)

Tag der Disputation: 16. April 2015

Contents

1. Introduction	1
2. Definitions	4
2.1. Angle Resolved and Total Scattering (ARS, TS)	4
2.2. Surface Power Spectral Density (PSD) function	5
2.3. Roughness parameters	6
3. Light scattering and surface roughness models	7
3.1. Light scattering models for interfaces and defects	7
3.1.1. Single surface scattering theories	7
3.1.2. Multilayer systems	10
3.1.3. Surface defects	11
3.2. Interface roughness models	12
3.2.1. Single surface PSD-models	13
3.2.2. Roughness evolution and roughness correlation in thin film coatings	15
4. Experimental set-ups for angle resolved scattering measurements	18
4.1. Goniometer based set-ups	18
4.2. Multi-detector and integrating systems	20
4.3. Detector matrix based light scattering sensor	21
4.3.1. Sensor concept and comparison to the state-of-the-art	21
4.3.2. Discussion of technical details	24
4.3.3. Uncertainty budget	34
4.3.4. Reliability of roughness measurement results	39
4.3.5. Summary	44
5. Techniques applied for direct roughness and defect assessment	45
5.1. Topography measurement techniques	45
5.2. Surface defect classification	46

6. Light scattering properties of optical surfaces and thin films	48
6.1. Anisotropic light scattering distributions and surface structures	48
6.1.1. Approaches to measure and quantify structure properties of anisotropic surfaces	49
6.1.2. Anisotropic roughness of magnetorheologically finished surfaces	56
6.1.3. Concluding remarks	62
6.2. Roughness evolution of titanium thin film coatings	63
6.2.1. Adaption of the light scattering sensor	63
6.2.2. Roughness and anisotropy evolution of titanium thin films	65
6.2.3. Concluding remarks	70
6.3. Roughness induced scattering of complex multilayer systems	71
6.3.1. Development of the light scattering and interface correlation model	71
6.3.2. Application scenarios for the light scattering sensor	81
6.3.3. Concluding remarks	84
6.4. Light scattering analysis and classification of surface defects	85
6.4.1. Light scattering sensor qualification and applicability evaluation	85
6.4.2. Angle resolved scattering and topographies of surface defects	87
6.4.3. Light scattering modeling to classify defects	90
6.4.4. Concluding remarks	94
7. Summary	95
Bibliography	98
A. Auxiliary calculations	113
A.1. Estimation of fluorescence power in laser scanning microscopy	113
A.2. Asymptotic evolution of correlation length	113

Nomenclature

Acronyms

ACF	surface auto covariance function
AFM	atomic force microscope / microscopy
ARS	angle resolved scattering
BKT	Beckmann-Kirchhoff theory
BRDF	bidirectional reflectance distribution function. Generalized versions are the BTDF or the BSDF with T for transmittance and S for scattering, respectively.
C1, C2	abbreviations for the first or the second illumination channel of the light scattering sensor (C1: $\theta_i=18^\circ$, $\lambda=660$ nm; C2: $\theta_i=50^\circ$, $\lambda=405$ nm)
CMOS	complementary metal-oxide-semiconductor
GV, GV_{HG} , GV_{cor}	gray value (0...255) determined with the CMOS sensor; “HG” stands for the dark signal; “cor” for normalization by dark signal, exposure time, and GV non-linearity
$h\text{ARS}$	“highly” angle resolved scattering obtained with the light scattering sensor
MRF	magnetorheological finishing
NAL	near angular limit
$\text{PSD}_{2\text{D},\text{iso}}$	azimuthally averaged PSD function as a function of the radial spatial frequency f
PSD	power spectral density function of a surface topography as a function of the spatial frequencies f_x and f_y
SPDT	single-point diamond turning
TS	total (integrated) scattering (scattering loss)
VPT	first order Rayleigh-Rice vector perturbation theory
WLI	white-light interferometer / interferometry

Greek symbols

β	roughness evolution exponent in roughness and PSD evolution models
δ	parameter for the deviation of the optical thin film thickness
$\Delta\Omega_s$	solid angle in a light scattering measurement
θ_1^{min}	angular distance between the specular reflex and the first minimum in an ARS distribution of a surface defect
θ_s	polar scattering angle
λ	wavelength of light
σ	surface root-means-square (rms) roughness, also named S_q
$\hat{\sigma}_{\text{std}}$	anisotropy parameter, which is defined as the standard deviation of the normalized directional rms roughness values $\hat{\sigma}_i$
τ_c	correlation length of a surface structure at which the corresponding azimuthally averaged ACF drops to $1/e^2$
τ_x, τ_y	lag or displacement vector in the calculation of the ACF
φ_s	azimuthal scattering angle

Ψ	spherical plane wave, applied in the Beckmann-Kirchhoff theory
Ω, μ, ν	parameters applied in kinetic continuum (“ $\Omega\mu\nu$ ”) and combined PSD models

Mathematical symbols

a	PSD replication factor in kinetic continuum and empirical roughness evolution models
A, B, C	parameters applied in the ABC PSD model
\mathfrak{C}_i	optical factor that describes the field scattered in an observation direction at an interface i in a multilayer system including the transition from the incident field to the scattered field
\mathfrak{d}	feed period in single-point diamond turning
d	thin film thickness
$\mathbb{D}_{ \text{mean-med} }$	anisotropy parameter, which is defined as the difference of the mean and the median of the normalized, directional rms roughness values $\hat{\sigma}_i$
D	diameter of a surface defect
E	incident scalar (plane) wave, applied in the Beckmann-Kirchhoff theory
\mathfrak{f}	focal length
F	Fresnel amplitude, applied in the Beckmann-Kirchhoff theory
$f_{x,y}, f, f_\varphi$	surface spatial frequencies in cartesian (f_x, f_y) or polar coordinates (f, f_φ)
$h(\vec{f})$	Fourier transform of a surface profile $z(x, y)$
\vec{k}	wavevector
K, n_K	parameters applied in fractal PSD model functions. K corresponds to the level and n_K to the slope of the PSD curve in a log-log scaled diagram
\vec{n}	local surface normal in the Beckmann-Kirchhoff theory
P_i / s	power of light (incident or scattered)
$\text{PV}_{\text{ACF}, \hat{\sigma}}$	anisotropy parameter, which is defined as the autocorrelation of the normalized, directional rms roughness values $\hat{\sigma}_i$ as a function of a displacement in azimuthal spatial frequencies φ_f
Q	optical factor determined by scattering geometry, refractive index, and polarization, which relates the ARS and PSD
\vec{r}	position vector, applied in the Beckmann-Kirchhoff theory
\mathbb{R}	ratio of integrated scattering values S of surface positions with and without defects
R	reflectivity
S	(partially) integrated scattering in the scattering angles of the scattering sensor
t_{int}	exposure time of the CMOS sensor
T_{opt}	optical thin film thickness
\mathbb{U}	scattered scalar field in the Beckmann-Kirchhoff theory
U, u	U : combined measurement uncertainty; u : standard deviation (uncertainty) of input quantities for ARS determination
V_{cor}	signal from the CMOS sensor normalized for (global) non-linearity, background signal, and exposure time
x, y, z	Cartesian coordinates

1. Introduction

Technological developments push the challenges for the quality assessment in optical fabrication into two directions. On the one hand, the demands on accuracy and sensitivity are increased; on the other hand, in-line or at least on-line capabilities are required for an efficient inspection of high volume components. Nevertheless, a number of characterization tasks are still restricted to an ex-situ evaluation of few, randomly chosen samples in laboratory environments. This holds in particular for the assessment of surface related quality features such as interface and thin film roughness or surface defects. These imperfections are typically the most critical origins of light scattering [1,2], which can result in contrast degradation, resolution limitation, or optical throughput reduction [3–5]. Therefore, this thesis is focused on the surface quality assessment regarding roughness and defects.

Conventionally, nanostructures of optical surfaces are evaluated by employing direct topography measurement techniques such as stylus profilometry, white light interferometry, or atomic force microscopy. These techniques are, however, restricted to small sections on cooperative samples and require considerable measurement times. Moreover, the basic measurement principles are extremely sensitive towards vibrations or environmental influences and are, hence, not well suited for an application in production environments.

Surface defects can be analyzed using topographic techniques as well. However, since defects constitute singular localized surface features, full surface defect evaluation with these techniques is impractical. Consequently, surface defects are to a large extent visually assessed by trained persons [6–8] or by applying industrial vision techniques in special dark field arrangements [9,10]. Unfortunately, direct, quantitative descriptions of the light scattering impact from imperfections are not available through such approaches.

Light scattering techniques provide the potential to meet the demands of high volume fabrication of optical components and can be a method of choice to overcome the limitations of the assessment procedures mentioned. They are sensitive for extremely low levels of surface imperfections, fast, insensitive to vibrations, and non-contact. Besides the quantification of the negative scattering impact, the results of advanced light scattering techniques provide information about the imperfections from which the scattering originates. This is, in particular, enabled by the high information level obtained from angle resolved light scattering measurements and by corresponding scattering models.

Typical approaches for the angle resolved characterization of scattering are goniometer based laboratory systems, which provide highest sensitivity and highest flexibility [5,11–16]. On the other hand, this flexibility is accompanied by a high complexity and requires time consuming scanning measurement approaches. In particular the latter prevented the

1. Introduction

application of elaborated goniometer based light scattering techniques even for the close to fabrication assessment so far.

To overcome these limitations, approaches such as multidetector arrangements [17–19] or set-ups for fast integrating scattering measurements [20] were developed, which, however, are connected to a loss of the 3D angularly resolved information. The most promising approach, the application of semiconductor matrix devices, can be assumed as a continuation of first approaches to analyze the angle resolved scattering from photographic images [21–23]. A large diversity of instruments that exploit this approach exist for several applications such as scattering measurements of suspensions [24] or airborne particles [25,26], for computational vision related tasks [27], or already for scattering based roughness analyses [28,29]. Nonetheless, developing sensor devices for the assessment of optical surfaces still constitutes a challenging task, although a simple sensor head for light scattering based roughness analysis of rough engineering surfaces was introduced as early as in 1985 [30], and even a hand held sensor head with three detector elements to monitor the degradation of airplane sensor windows was developed in the early 90s [31,32].

Even typical state-of-the-art matrix based scatterometers [27–29,33–38] are either semi-complex laboratory systems, or limited in measurement speed, or lack of the sensitivity required for the characterization of standard and high quality optical components. The third point is the main reason which has impeded the application of sensor type systems in the fabrication of optical surfaces so far. Only multidetector devices for particle and killer defect evaluation in semiconductor industry have been established [39,40], which, however, are seldom compact sensor-like devices and lack of angular resolution.

Besides the technical aspects, elaborated sensor systems would be of reduced value without an appropriate understanding of the structure-scattering-relationships which enable the investigation of quality properties from scattering measurements. Since the advent of the fundamental physical relations, which link surface imperfections and light scattering, at the beginning second half of the last century [41–45], light scattering techniques have been widely applied for surface imperfections analyses, in particular for surface roughness measurement [21,46–52]. However, the lack of practicable frameworks consisting of elaborated, highly sensitive sensor systems and comprehensive analysis methods has been an additional obstacle for the application of light scattering techniques for the close-to or in-process surface characterization in optical fabrication.

Therefore, both aspects will be addressed in this thesis: the development of a compact semiconductor matrix based light scattering sensor concept, which is sensitive enough for the characterization of high quality optical components, as well as the development of corresponding practicable post-measurement analysis approaches by exploiting fundamental structure-scattering-relationships.

The implementation of the sensor concept requires the development of a compact, but elaborated beam preparation system and aims on the application of a commercial CMOS matrix detector for fast and sensitive 3D angle resolved scattering measurements. Besides

the technical aspects, measurement routines to achieve reliable, calibrated measurements have to be developed and evaluated. Once this measurement framework is established, different aspects of surface quality can be analyzed with tailored analysis methods. This task includes the study of the physical relations, which link surface imperfections and scattering, as well as the development of novel analysis methodologies, which only become practicable with the development of a fast sensor concept with 3D measurement capability. On the other hand, the influences of the specific challenges induced by the sensor concept on the application of the structure-scattering-relationships have to be investigated. These are for example the limited angular range or the limited measurement parameters available.

This thesis is organized as follows.

In Sec. 2, the basic definitions required to quantify light scattering and to describe surface structures by stochastic quantities are introduced. Thereafter, in Sec. 3, theoretical approaches to link surface imperfections and light scattering properties are reviewed, summarized, and expanded. In this context different models for the description of random rough single surfaces and rough interfaces in multilayer systems are additionally discussed, which are the key for the practical application of light scattering models.

The semiconductor matrix based light scattering sensor, developed in the course of this thesis, is presented in Sec. 4. Besides the technical details, a review of other state-of-the-art matrix based and conventional light scattering measurement approaches is presented. A primary topic in this section is the reliability of the measurement results obtained with the sensor. This includes the evaluation of the measurement and calibration procedure, the uncertainty budget analysis, as well as the discussion of the applicability for roughness measurements in the context of the sensor specifications.

Section 5 provides a brief overview of direct surface topography measurement approaches which are widely applied to derive stochastic surface properties and of techniques which are typically employed for the assessment of surface defects. These techniques provide light scattering independent nanostructure properties to verify, extend, and refine the modeling and evaluation procedures developed.

In Sec. 6, the light scattering sensor and the introduced structure-scattering-relations are utilized for the characterization of optical surfaces and multilayer systems, for which novel, sensor specific measurement and analysis approaches are derived. These are, in particular, methodologies for the nanostructure investigation of anisotropic surfaces and thin film titanium coatings, approaches to monitor properties of a complex notch-filter multilayer system, and a technique for the reliable assessment and classification of surface defects.

2. Definitions

In the following sections, definitions and abbreviations which are employed to describe light scattering phenomena and the stochastic properties of surfaces are introduced.

2.1. Angle Resolved and Total Scattering (ARS, TS)

The Angle Resolved Scattering (ARS) represents the power ΔP_s scattered into a solid angle $\Delta\Omega_s$ as a function of the scattering angles (θ_s, ϕ_s) . ARS is normalized to the solid angle and to the incident power P_i [53,54]:

$$\text{ARS}(\theta_s, \phi_s) = \frac{\Delta P_s(\theta_s, \phi_s)}{\Delta\Omega_s P_i} \approx \frac{dL_r}{dE_i} \cos \theta_s = \text{BRDF}(\theta_s, \varphi_s) \cos \theta_s \quad . \quad (2.1)$$

ARS is also named cosine corrected BRDF¹ [55] or more generally, if not restricted to the backward hemisphere, cosine corrected BTDF/BSDF¹.

BRDF, which is approximately ARS divided by $\cos \theta_s$, is defined and standardized in [56–58] as the ratio of the surface-related quantities reflected radiance L_r and incident irradiance E_i . Nevertheless, ARS is used in this work, since it is defined in directly measurable quantities, which are not restricted to surface related scattering.

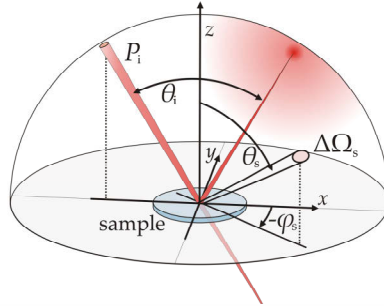


Fig. 2.1.: Light scattering geometry and nomenclature [57,59]. (θ_s, φ_s) - polar and azimuthal scattering angles, θ_i - incidence angle, $\Delta\Omega_s$ - solid angle, P_i - incident power, (x, y, z) - Cartesian coordinates, z -axis corresponds to macroscopic sample normal.

The corresponding definitions of the polar and the azimuthal scattering angles with respect to the sample surface and the coordinate system are given in Fig.2.1. In the following, the angle of incidence θ_i is within the $\varphi_s=0^\circ$ plane, but is counted in the opposite direction than the polar scattering angle θ_s . ARS distributions determined using the newly developed light scattering sensor are abbreviated as *hARS* in order to distinguish them from those obtained with goniometer systems. The "h" can be interpreted as "highly" or the first letter of the sensor acronym *horos*.

¹Bidirectional Reflectance/Transmittance/Scattering Distribution Function

To quantify scattering losses, ARS can be integrated to the Total Scattering (TS) or to partially integrated scattering values (S):

$$S = \frac{P_s}{P_i} = \iint_{(\theta_s, \varphi_s)} \text{ARS}(\theta_s, \varphi_s) \sin \theta_s d\theta_s d\varphi_s \quad . \quad (2.2)$$

With respect to ISO-13696 [60], scattering angles of $\theta_s < 2^\circ$ and $\theta_s > 85^\circ$ have to be included to obtain the Total Scattering of a sample in the backward or forward hemisphere $\text{TS}_{b/f}$ at normal incidence. For oblique incidence this definition can be adapted by defining the minimal acceptance angle with respect to the specularly reflected (transmitted) beam.

2.2. Surface Power Spectral Density (PSD) function

Single surfaces are described in 3D Cartesian coordinates as a function $z(x, y)$ with a mean of $\bar{z}=0$. In this concept, z is assumed as a single-valued function of (x, y) so that the surfaces exhibit neither overhangs nor shadowing. In addition, the surfaces have no tilts or macroscopic curvatures.

Several quantities and functions for a statistical description of a rough surface exist. In this section, the Power Spectral Density (PSD) function and the Auto Covariance Function (ACF) are introduced which include the essential aspects of surface roughness: "roughness heights and lateral dimensions" [61]. In particular the PSD is the most important input for the angle resolved modeling of surface scattering in perturbation theories (Sec. 3.1).

PSD functions describe the power of the individual roughness components of a surface as a function of the spatial frequencies (f_x, f_y) and are defined as the squared modulus of the Fourier transform of a surface profile within the area L^2 [62–64]:

$$\text{PSD}(f_x, f_y) = \lim_{L \rightarrow \infty} \left| \frac{1}{L^2} \iint_{L^2} z(x, y) e^{2\pi i(xf_x + yf_y)} df_x df_y \right|^2 \quad . \quad (2.3)$$

For the discussion of isotropy properties as well as for an easier visualization and comparison of PSD functions, the spatial frequencies can be transformed into polar coordinates (f, φ_f) . This additionally enables to average over the polar frequencies φ_f which yields the 2D isotropic PSD ($\text{PSD}_{2D, \text{iso}}$), a 2D representation in radial spatial frequencies f :

$$\text{PSD}_{2D, \text{iso}} = \frac{1}{2\pi} \int_0^{2\pi} \text{PSD}(f, \varphi_f) d\varphi_f \quad . \quad (2.4)$$

For an isotropic surface and in an ensemble average sense (or $L \rightarrow \infty$), there is no loss of information in this procedure, since the (3D-)PSD is rotationally symmetric [63,65].

The $\text{PSD}_{2D, \text{iso}}$ facilitates single PSD functions, measured at different surface positions or in different spatial frequency ranges², to be combined to Master-PSD functions [63] that

² Different measurement techniques or operation parameters (measurement area, lateral resolution, ...) result in varying spatial frequency ranges (Sec. 5.1).

2. Definitions

cover an extended spatial frequency range and provide averaged information of different positions on the surface. By the application of $\text{PSD}_{2\text{D},\text{iso}}$ functions, complex 3D-stitching procedures in the frequency space are avoided in the combination procedure.

Only Master-PSD functions determined from different measurement areas and with different techniques provide a compact representation of surface roughness properties over a spatial frequency range of more than 6 decades. If this would be aspired in a single measurement, the measurement area has to be as big as the inverse of the lowest spatial frequency and requires a resolution as low as the inverse of the highest spatial frequency. Acquiring this measurement data without changing the operational parameters or the resolution requires the acquisition of at least $(10^6)^2$ data points.

The Auto Covariance Function (ACF) is the Fourier transform of the PSD and describes the self-similarity of the surface as a function of the displacement or lag vector (τ_x, τ_y) [62,66,67]. From a rotationally averaged $\text{ACF}_{2\text{D}}$ the surface correlation length τ_c , a characteristic length of the self-similarity, can be determined [62], which is defined as $\text{ACF}_{2\text{D},\text{iso}}(\tau_c) = 1/e^2 \text{ACF}_{2\text{D},\text{iso}}(0)$.

2.3. Roughness parameters

A variety of statistical parameters are standardized [64,67] to describe and quantify surface roughnesses (e.g. the arithmetic mean deviation S_a or the ten-point height S_z). In this work the surface root-mean-square (rms) roughness σ is applied, since it is proportional to the square root of the total scattering (Sec. 3.1.1).

σ is defined as the mean deviation of a surface profile $z(x, y)$ which has to be corrected for at least tilts and, if relevant, for macroscopic curvatures. Otherwise, these deviations would contribute to σ . Besides the basic definition, the rms roughness can be calculated by integrating the PSD [63,68]:

$$\sigma^2 = \iint_{(f_x, f_y)} \text{PSD} \, df_x df_y = 2\pi \int_f \text{PSD}_{2\text{D}} f \, df \quad . \quad (2.5)$$

A primary aspect, relevant for the comparison of roughness values determined using different measurement techniques, systems, or parameters is the bandwidth limitation of any roughness value. In this context, PSD functions provide one way to calculate rms roughness values with tailored bandwidth limits.

A pure rms roughness value without a frequency range specified omits any information on bandwidths and, moreover, provides no information on anisotropy properties. Concerning anisotropy even the very detailed surface texture parameter standard ISO 25178-2 [67] defines only the direction of the primary roughness component. Therefore, directional roughness values as well as anisotropy parameters will be introduced in Sec. 6.1.1, in which their application to highly anisotropic surfaces will be discussed as well.

3. Light scattering and surface roughness models

Scattered light is the elementary carrier of information for the visual perception of the environment. It contains for instance information about materials, colors, or surface textures. In this context, the majority of surfaces of optical components should be "invisible", since light scattering is an unwanted effect. However, even the lowest levels of surface imperfections act as random phase gratings and produce scattered light, which can be exploited to obtain valuable information.

In this section, relations between the light scattering and imperfections of single surfaces and multilayer systems that will be applied in the experimental part of this thesis are reviewed and summarized. In addition, models to describe the stochastic properties of the surface roughness and the roughness evolution in multilayer systems are presented which are required for a systematic investigation of light scattering mechanisms. Besides the review, approaches developed in the context of this thesis for the expansion, practical application, or software implementation of the theories and models are briefly introduced.

3.1. Light scattering models for interfaces and defects

3.1.1. Single surface scattering theories

Early approaches for the modeling of light scattering at rough optical surfaces with a first order vector perturbation theory are presented by Church and Zavada in [44], [69]. The theory originated from previous work by Rice [41], developed for radar wave scattering, in which the transition conditions of the Maxwell equations at a rough boundary are solved to the second order¹. The work of Rice, on the other hand, is based on publications by Lord Rayleigh [62, Ch.1] on the light scattering at (smooth) gratings [70] or on the scattering of sound and electromagnetic waves at rough surfaces [71, pp.89-96]. Therefore, the theory is also known as first order Rayleigh-Rice vector perturbation theory (VPT).

Different approaches for optically smooth surfaces reveal comparable results and can be found in [45,66,72,73]. The most common representation of the ARS in the far-field of a single metallic or dielectric surface with $\sigma \ll \lambda$ is the following [55,74,75]:

$$\text{ARS}(\theta_s, \varphi_s) = \frac{16\pi^2}{\lambda^4} \cos^2 \theta_s \cos \theta_i Q \text{PSD}(f_x, f_y) \quad . \quad (3.1)$$

λ is the illumination wavelength and Q is an optical factor that is determined by the refractive index, the scattering angles, the angle of incidence, as well as the polarization

¹ First PERTURBATION order. The zero and first order of the BOUNDARY CONDITIONS correspond to the absence of a surface and an ideally smooth, respectively.

3. Light scattering and surface roughness models

states of illumination and detection². Some more details on the optical factor Q for non-magnetic materials are described in [62]. In addition, a reasonable approximation of Q for metallic surfaces by the surface reflectivity is also discussed [62], which holds in particular for scattering close to the specular reflex.

In several publications, the validity of the VPT is referred to $(4\pi\sigma \cos \theta_i)^2 \ll \lambda^2$ [62,76,77]. However, this restriction is further discussed regarding the light scattering sensor in the second part of Sec. 4.3.4.

Equation 3.1, which is sometimes called the "golden rule" [78], is applied to model the scattering in a wide wavelength range from radar [41] over infrared and visible light [15,21,62,63,79–81] to x-ray scattering [72,82,83]. This is to a high level attributed to the linear relation of PSD and ARS, which can be exploited to determine roughness properties by light scattering measurements and vice versa. The corresponding translation of scattering angles and spatial frequencies is given by the grating equation (first order):

$$f_x = \frac{1}{\lambda} (\sin \theta_s \cos \phi_s - \sin \theta_i) \quad f_y = \frac{1}{\lambda} (\sin \theta_s \sin \phi_s) \quad , \quad (3.2)$$

which yields a relevant range of $f \approx 0.01 \mu\text{m}^{-1} \dots 2.6 \mu\text{m}^{-1}$ for the scattering of visible light.

Integration of Eq. 3.1, assuming $Q \approx R$ and dominant scattering close to the specular reflex, reveals a proportionality of TS to the rms roughness squared [62]. This relation is identical to that derived in [42] for smooth surfaces with Gaussian height distributions; furthermore, it is an approximation of a more general exponential relation for arbitrary rough surfaces with Gaussian high distributions and Gaussian ACFs derived in [84, Ch.5]:

$$\text{TS} = R \left(1 - e^{-\left(\frac{4\pi \cos \theta_i}{\lambda} \sigma\right)^2} \right) \approx R \left(\frac{4\pi \cos \theta_i}{\lambda} \sigma \right)^2 \quad . \quad (3.3)$$

However, for smooth surfaces the Gaussian requirements are not necessary, since the approximation can be obtained from Eq. 3.1 for arbitrary PSD functions [62].

Some publications [85,86] describe a different version of the approximated part of Eq. 3.3, which is proportional to λ^{-4} . This is, however, only an analytical expression for surfaces with specific PSD shapes which are almost horizontal in the scattering relevant frequency range ($\tau_c \ll \lambda$; e.g. ABC-model, Sec. 3.2.1). The scaling is a result of the changing relevant roughness for varying PSD integration limits $f = (0, 2\pi/\lambda]$ as a function of λ . However, as pointed out in [87] and already indicated in [74], this different scaling does not contradict the validity of the approximation of Eq. 3.3 if it is applied for the relevant roughness³.

For oblique incidence [85] and sections of the scattering hemisphere (symmetrical to the specular reflex) the approximated version of Eq. 3.3 also holds for the partially integrated scattering values S if the correct relevant roughness is applied. Therefore, this equation

² Q is often replaced by Q_{kl} that can be linearly combined to describe arbitrary polarization [62]. k and l represent the polarization states (s-pol, p-pol) of illumination and detection, respectively.

³ Integration over $f = [\sin \theta_s^{\min}/\lambda, 2\pi/\lambda]$, with θ_s^{\min} the lowest accessible scattering angle.

can also be exploited for roughness measurements in the limited angular range of the light scattering sensor.

The second theory applied to model the ARS of single surfaces in this thesis is the scalar Beckmann-Kirchhoff Theory (BKT). The theory is based on the Kirchhoff integral theorem, from which the well known (Fresnel-)Kirchhoff diffraction integral is derived [88, Ch.10.4]. In contrast to diffraction from planar screens with apertures, the varying local normal of a rough surface complicates the evaluation of the original integral [89]. Consequently, Beckmann applied the Kirchhoff theorem with stochastic assumptions about the distribution of the surface normal and derived closed solutions for single (opaque/metallic) surface scattering. The basic equations include a tangent plane approximation [84,89] which is applied to the fields in the Kirchhoff integral formula:

$$\mathbb{U} = \frac{1}{4\pi} \iint_{\mathbb{A}} E \frac{\partial \Psi}{\partial \vec{n}} - \frac{\partial E}{\partial \vec{n}} \Psi \, d\mathbb{A} \quad . \quad (3.4)$$

with $E \propto e^{i(\vec{k}_1 \vec{r}_1 - \omega t)}$, $\left(\frac{\partial E}{\partial \vec{n}} \right)_{\mathbb{A}} \approx (1 - F) E$, $\Psi = \frac{e^{i\vec{k}_2 \vec{r}_2}}{r_2}$

Moreover, a limitation to smooth surface curvatures with radii r_c larger than the wavelength [84,90,91] is inherent to the tangent plane approximation [84]:

$$4\pi r_c \cos \theta_{\vec{k}, \vec{n}_{\text{local}}} \gg \lambda \quad . \quad (3.5)$$

Additional information on the geometry and nomenclature of the BKT is illustrated in Fig. 3.1 on p. 10. \mathbb{A} is the evaluated surface area; E the incident plane wave; F the Fresnel reflection amplitude of the ideal surface at the local incidence angle; and Ψ a scattered spherical wave. r_1 and r_2 are vectors on the surface and from a position on the surface to the observation point, respectively. For an ideal metallic surface, F is 1 for a p-polarized incident wave and -1 for an s-polarized incident wave, respectively.

The BK-theory is based on scalar diffraction; hence polarization as well as multiple scattering or shadowing effects are not included. Therefore, problems concerning the energy balance are mentioned in [92] and an additional paraxial limitation is inherent. For moderately rough surfaces, for which shadowing as well as multiple scattering are of reduced concern, these limitations are not critical. This should hold in particular for the scattering at moderate angles of incidence and close to the specularly reflected beam - the geometrical conditions present for the light scattering sensor. At least the limitations of the smooth surface approximation should be extended to moderately rough (metallic) surfaces if the BKT is applied.

Closed mathematical (invertible) solutions of the BKT exist only for $\sigma \ll \lambda$ and $\sigma \gg \lambda$ for surfaces which exhibit specific stochastic properties such as a Gaussian height distribution and a Gaussian ACF [84,93,94] or an exponential ACF [95]. For a Gaussian surface with $\sigma \approx \lambda$ the solution is an infinite series. However, these stochastic properties are only

3. Light scattering and surface roughness models

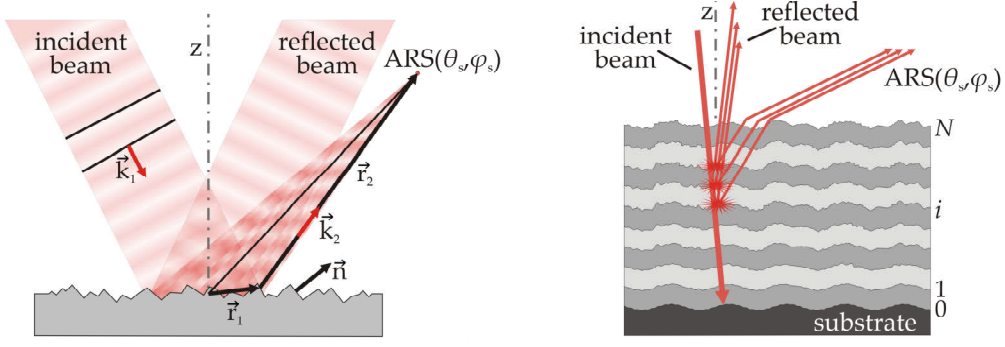


Fig. 3.1.: Geometry and variables used in Beckmann-Kirchhoff theory (left) and in multilayer scattering theory (right).

valid for a limited number of surfaces [96]. Moreover, forward scattering calculations would require knowledge of the correlation length τ_c and of the entire ACF including the "complete" range of spatial frequencies.

To avoid these limitations in this thesis, Eq. 3.4 is evaluated numerically for surface profiles which are measured or generated numerically from PSD models (Sec. 3.2.1). Following the math in [97], the ARS is calculated from the scalar field \mathbb{U} to compare the results to that of the VPT and to measurements:

$$ARS(\theta_s, \varphi_s) = |\mathbb{U}(\theta_s, \varphi_s)|^2 \frac{\cos \theta_s}{r_{\text{det}}^2 \iint_{\mathbb{A}} E_0^2 d\mathbb{A}} \quad (3.6)$$

E_0 is the field intensity distribution of the illuminating beam and r_{det} the distance of the relevant detector element.

Similar numerical BKT based modeling results of 2D-surface scattering are presented in [17] derived with a Fraunhofer far-field approximated version of Eq. 3.4.

3.1.2. Multilayer systems

Besides a few scalar modeling approaches [98,99], most models for interface roughness scattering in multilayer systems [100–106] can be assumed as further developments of the VPT. In these terms the scattering of a multilayer system is represented by the superposition of the fields scattered at the single interfaces considering the relevant interference effects of incident and scattered light fields as well as the interface roughness correlation properties [54,103]:

$$ARS(\theta_s, \varphi_s) = \frac{4\pi^2}{\lambda^4} \mathcal{K} \sum_{i=0}^p \sum_{j=0}^p \mathfrak{C}_i \mathfrak{C}_j^* \text{PSD}_{ij} \quad (3.7)$$

This relation is implemented in a corresponding software developed at the Fraunhofer IOF [107]. The factors \mathfrak{C} , which are calculated by the admittance formalism [108], describe the propagation and transition of incident and scattered fields within the multilayer system [103]. The cross-correlation Power Spectral Density functions PSD_{ij} are the products of the Fourier transforms of the i -th and the complex conjugated pendants of the j -th interface, which is identical to the PSD of the i -th interface for $i=j$.

The cross-correlation properties of the interfaces (in ergodic sense) can significantly influence the light scattering distributions by additional constructive or destructive interference effects. Therefore, specific simplified models to describe PSD_{ij} functions are presented in Sec. 3.2.2 in the context of roughness evolution in multilayer systems.

To enable extended analyses of the field distributions within multilayer systems and to handle complex systems with an increased number of interfaces, another theory [104] was implemented in Matlab in the context of this thesis. This theory applies the matrix formalism [109, Ch.1.6] to calculate the field distributions within the multilayer. Although the basic approaches are different, the ARS results are identical to those of Eq. 3.7⁴ and some rearrangements of the equations in [104] result in a similar double sum.

The main advantage of this theory is its ability to include the thin film bulk as source of light scattering as for example demonstrated by the author of this thesis in [110] for graded index thin film systems. In addition, the accessibility of the entire code facilitates additional analyses of the light scattering properties within the multilayer system. In particular the complete distributions of the incident and scattered wave fields can be analyzed; even the field within a single layer is accessible by inducing virtual interfaces without refractive index contrast.

3.1.3. Surface defects

Compared to the measurement of surface roughness by light scattering techniques, there has been considerably less theoretical and experimental work to assess typical defects in optical surfaces from their scattering distributions [2,18,52,74,111]. This may have been attributed to the fact that typical pits, digs, or scratches do not fulfill the restrictions of the VPT. Consequently, in [2] and in [18], the Kirchhoff diffraction integral was applied to model the scattering of scratches with rectangular shape or of defects with arbitrary surface profiles, respectively. However, the modeling was limited to 2D surface profiles.

Within the limitations discussed in Sec. 3.1.1, there is no general restriction for the application of the VPT to predict the scattering of elementary single surface defects. If the VPT is applied for this purpose, it is also referred to as "shot model" with PSD functions describing single (nano-)defects or distributions thereof [74]. A similar application of the VPT is presented in [52] to model scattering distributions of single or homogeneously distributed cylindrical pits or refractive index inhomogeneities. An elementary result of this approach is the prediction of characteristic oscillations in the ARS of defects with diameters D those minima correspond to zeros of the Bessel function of first kind and first order [52]. Hence, the angles of the minima, in particular of the first minimum, can be calculated [52]:

$$\sin \theta_1^{\min} = \frac{1.22 \lambda}{D} . \quad (3.8)$$

⁴ Deviations of ARS results were observed for "pp-polarized" scattering. These could be corrected by a modification to the permittivity in the corresponding transition matrix (Eq. (35d) in [104]).

3. Light scattering and surface roughness models

This result for normal incidence is identical to the Rayleigh criterion for the angular resolution.

For oblique incidence, it is possible to exploit the similarity of Eq. 3.8 to the grating equation. As will be demonstrated in Sec. 6.4, $f_{x/y}$ and $\sin \theta_1^{\min}$ can be replaced by $1.22/D_{x,y}$ and by the corresponding scattering geometry terms of Eq. 3.8, respectively. Nonetheless, θ_1^{\min} will be applied as abbreviation for the angular distance of the first minimum to the specular reflex in the following.

The most critical defects, in particular those specified in the corresponding quality assessment standards [8,112–114], and the defects presented in Sec. 6.4.2 are beyond the smooth surface criterion; hence, the VPT is not applicable. On the other hand, the application of the BKT is less restrictive, since there is no general limitation concerning the roughness amplitudes or the vertical defect dimensions. However, secondary limitations as the local surface curvatures, in particular close to steep edges, or the validity of the Fresnel factor F in the defect may be violated.

Thus, the numerical evaluation of scattering modeling results of elementary pits or humps that are not within the validity range of the shot model should be possible, but needs to be verified. This is done in Sec. 6.4.3 by comparison of modeled and measured h ARS distributions. The BKT modeling of defects, which is applied in the context of this thesis for the first time, can be assumed as a continuing step following the work of [2] and [18] which was restricted to 2D defect profiles.

For singular surface flaws, the modeling of ARS distributions that are comparable to other modeling results or to measurements constitutes a complex issue, whichever model is applied. This is not a restriction of the models themselves. It is attributed to normalization issues induced by the non-ergodic, singular nature of defects in comparison to random rough surfaces. The differential scattering cross section DSC, which includes an additional normalization of the ARS to the illuminated surface area, is applied in some publications to overcome these problems [62,115]. However, it is not applied in this thesis for reasons that are discussed in Sec. 6.4.1.

3.2. Interface roughness models

PSD models that describe the stochastic properties of surface structures which are typical for optical components are required for comprehensive analyses of surface roughness and for the modeling of light scattering. The models presented in this section enable random rough surfaces as well as roughness evolution and roughness correlation properties in multilayer systems to be described with reduced parameter sets. With these sets, physical relations and properties can be identified and compared. In addition, the models can provide access to the roughness of buried interfaces and facilitate the extension of the accessible frequency ranges in measurements, as will be demonstrated for the light scattering sensor.

3.2.1. Single surface PSD-models

ABC and K-correlation model: The development of simplified model representations of random rough surfaces, in particular for PSD and ACF, was driven in parallel to the development of scattering models. For instance, the BKT requires special ACFs to derive analytical solutions. These were first of all Gaussian ACFs [84] followed by exponential ACFs [43] that should be applicable to a wider range of polished optical surfaces [93]. Exponential surface ACFs can also be derived from stochastic processes, such as the Poisson distribution of zero crossings or the normal Markov process [66,116–118].

These proven ACFs were transferred into PSD functions with the upcoming of the VPT. The Lorentzian PSD ($\approx \frac{a}{a^2+f^2}$) is the corresponding result for the exponential ACF [62], which is applied to model roughness induced light scattering in [21,66,74,119–121]. However, maybe driven by the need to describe a broader variety of surfaces with more flexible PSD models [62,122], the step from the Lorentzian PSD to the K-correlation or ABC model was done in Church et al. [123] by adding a flexible power to the denominator^{5,6}:

$$\text{PSD} = \frac{A}{\left(1 + (Bf)^2\right)^{(C+1)/2}} \quad (3.9)$$

In a log-log scale diagram (Fig. 3.2, p. 14) the ABC-PSD is similar to a knee with A determining the PSD level. C and B are responsible for the slope and the transition to the cut-off at high spatial frequencies (Fig. 3.2), respectively. In the spatial domain, this transition determines the typical lateral dimensions of the surface structures; therefore, the parameters B and C correspond to the correlation length τ_c [62, Ch.4].

ABC-PSD functions were first applied to model the roughness of polished substrate structures which show the beginning cut-off at low spatial frequencies [21,93]. If the cut-off transition is located at frequencies below the light scattering relevant range ($f < 0.01 \mu\text{m}^{-1}$, visible light), the ABC-model can be approximated by its limit for large B - the fractal PSD [62,76]⁶:

$$\text{PSD} = \frac{K}{f^{n_K+1}} \quad (3.10)$$

Later it was recognized that the ABC-Model fits the intrinsic roughness of thin film coatings as well [5,124,127,128]. In this case, the characteristic cut-off is typically at higher spatial frequencies.

Intrinsic roughness values and correlation lengths of the roughness structures can be determined for the ABC model [125,128]:

$$\sigma^2 = \frac{2\pi A}{B^2 (C-1)} \quad \tau_C^2 = \frac{(C-1)^2 B^2}{2\pi^2 C} \quad (3.11)$$

⁵ In [124] a more formalized derivation of the ABC model is provided, which is based on stationary stochastic processes. Moreover, the "fractal dimensions" of the model are discussed.

⁶ Eqs. 3.9 and 3.10 exist in different notations or versions for 2D or 3D surfaces [62,96,124–126]. Hence, comparison of parameters from different publications might require further mathematical effort.

3. Light scattering and surface roughness models

whereas the diverging integrals prevent this for the fractal approximation [76]. Hence, it is only possible to determine bandwidth limited values.

Kinetic continuum ($\Omega\nu\eta$) model: In contrast to the more or less empirically determined K-correlation model, the following model is the result of a discussion of thin film growth as kinetic continuum process by evaluation of the Langevin equation [129,130] or the KPZ equation [131]. In the case of a linear evolution model, the differential equations give the following PSD for a thin film of thickness d [102]:

$$\text{PSD} = \Omega \frac{1 - \exp[-2\nu |2\pi f|^\eta d]}{2\nu |2\pi f|^\eta}, \quad (3.12)$$

with parameters representing relevant physical quantities: Ω stands for the average size of the thin film constituting particles (clusters, molecules, atoms); ν for occurring relaxations processes [102]. The positive integer η can be associated with the kinetic mechanisms that dominate the high spatial frequency smoothing process such as evaporation and condensation ($\eta=2$), bulk diffusion ($\eta=3$), or surface diffusion ($\eta=4$) [102].

The progress of the resulting PSD curve is rather similar to that of the ABC model, besides a stronger curvature in the transition region (Fig. 3.2, left).

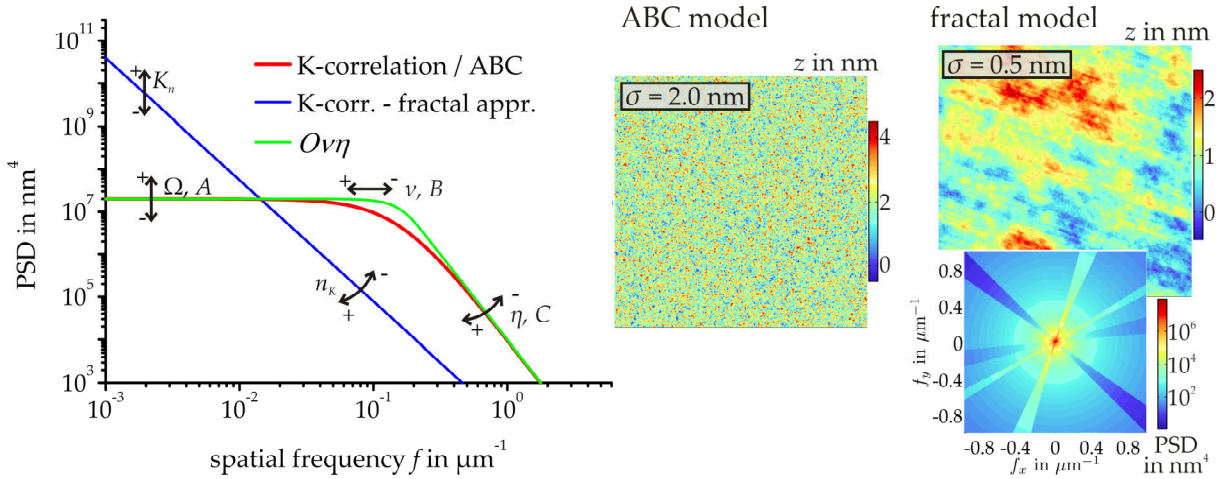


Fig. 3.2.: Examples of PSD-model curves (left) and generated surface topographies (right, $512 \times 512 \mu\text{m}^2$). Arrows indicate the influences of the model parameters. The generated surfaces correspond to the ABC model (red curve) and to an anisotropic fractal model (PSD_{2D,iso}: blue curve; 3D-PSD: inset).

Generation of model surfaces: The models presented can be (additively) combined [127–129,132–135] to approximate the often more complex progress of measured PSD functions. In particular the sum of a fractal and an ABC or an $\Omega\nu\eta$ model is well suited to describe the scattering relevant spatial frequency range of coated substrates.

For the numerical analyses of the BKT in the sections 4.3.4 and 6.4, it was necessary to generate 3D surface profiles that correspond to specific PSD models. Therefore, PSD models were evaluated on a rectangular grid and transferred into a surface Fourier trans-

form h by applying a random uniformly distributed [116] phase ψ :

$$h(\vec{f}) = \sqrt{PSD(\vec{f})} e^{i\psi(\vec{f})} \quad \text{with} \quad \psi(\vec{f}) = -\psi(-\vec{f}) \quad . \quad (3.13)$$

The surface profile $z(x, y)$ is generated by the inverse Fourier transform of $h(\vec{f})$; the correct symmetry properties ensure non-complex surface coordinates. Even surfaces with anisotropic surface properties as those in Sec. 6.1.1 or as the example in Fig. 3.2 can be generated by this approach.

3.2.2. Roughness evolution and roughness correlation in thin film coatings

Beyond single surfaces, PSD based roughness evolution models provide valuable information on the roughness development of growing single thin films or on the evolution of the interface roughness and its correlation properties in multilayer coatings. The models introduced here are based on the assumption that the PSD of a thin film surface represents an additive superposition of the substrate PSD and an intrinsic thin film PSD [127,129,132–135]. This implies the evolution mechanisms of the thin films or the intrinsic thin film PSD functions to be independent from the underlying roughness structure.

The main reason for introducing PSD evolution and cross-correlation models in this thesis is the assignment of the PSD_{ij} functions in multilayer scattering models (Eq. 3.7) with realistic quantitative values and to exploit the corresponding relations in roughness measurements. This is in particular necessary, since the interfaces within multilayer stacks are, if at all, only accessible by extremely high experimental efforts [136,137].

Empirical model: Different publications report that the evolution of the intrinsic thin film rms roughness as a function of the film thickness d follows power laws [131,138]: $\sigma \propto d^\beta$. In particular $\beta=1/2$ is referred to as the random deposition limit [139].

An empirical model that utilizes an ABC model for the intrinsic thin film roughness was introduced in [5] by replacing A in Eq. 3.9 with $\hat{A}d^{2\beta}$:

$$PSD(f, d) = PSD_{\text{sub}} + \frac{\hat{A}d^{2\beta}}{(1 + B^2 f^2)^{(C+1)/2}} \quad . \quad (3.14)$$

Consequently, the proportionality of the intrinsic rms roughness yields $\sigma \propto \sqrt{\hat{A}d^\beta}$. The position of the cut-off in the PSD (Fig. 3.3, left), and, hence, the correlation length (Eq. 3.11), is unaffected by the film thickness in this modification, although the lateral dimensions are related to power laws as well [138]. However, this is not necessary as long as the cut-off is not within the light scattering relevant spatial frequency range (Eq. 3.2).

Within this simple model, the roughness contributions of the substrate are perfectly replicated through the entire multilayer stack. Therefore, the combined roughness can be calculated as $\sigma = \sqrt{\sigma_{\text{sub}}^2 + \sigma_{\text{film}}^2}$ [132].

3. Light scattering and surface roughness models

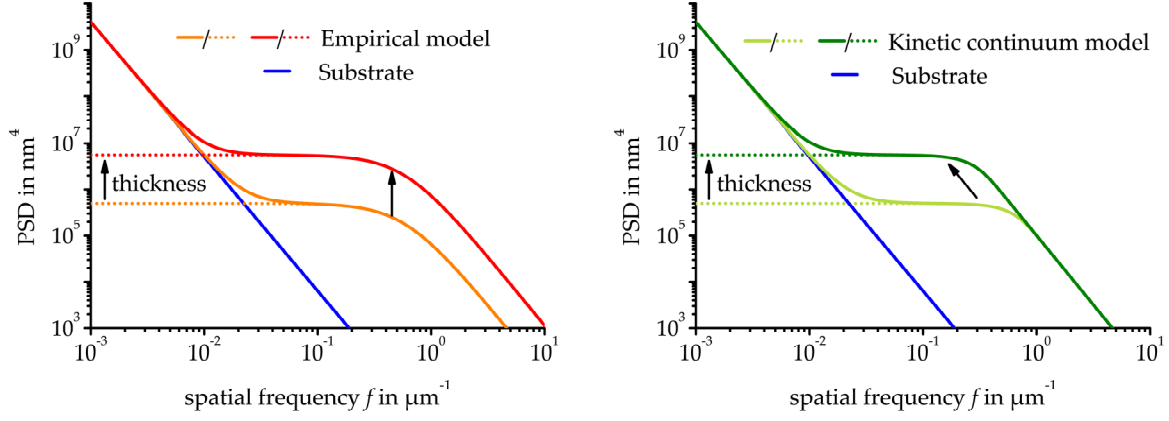


Fig. 3.3.: Example of PSD functions for the roughness evolution models. Empirical model (left); Kinetic continuum / combined model (right); dotted curves indicate the intrinsic thin film PSD functions

Kinetic continuum model: The PSD evolution (Fig. 3.3, right) that is inherent to the results of the kinetic continuum model (p. 14) [102,129] includes an evolution of the roughness with a fixed power of $\beta=1/2$. In addition, this evolution model comprises smoothing effects for the underlying roughness structures, which corresponds to a low pass filter included as the replication factor a . Hence, the PSD of a thin film of thickness d on a substrate is given as:

$$\text{PSD}(f, d) = a^2 \text{PSD}_{\text{sub}} + \left[\Omega \frac{1 - \exp[-2\nu |2\pi f|^\eta d]}{2\nu |2\pi f|^\eta} \right] \quad \text{with } a = e^{-\nu |2\pi f|^\nu d} . \quad (3.15)$$

Within this thesis the evolution parameters of thin films of different materials are not distinguished; therefore, the complexity of Eq. 3.15 is considerably reduced compared to [102]. In particular, there are no smoothing effects between the different materials so that the replication factors of the intrinsic thin film PSD functions have vanished. These assumptions are reasonable for thin film roughness components as long as the thin film structure of the materials is similar.

Combined model: The kinetic continuum model can be modified for different roughness evolution exponents simply by replacing d with $d^{2\beta}$:

$$\text{PSD}(f, d) = a^2 \text{PSD}_{\text{sub}} + \left[\Omega \frac{1 - \exp[-2\nu |2\pi f|^\eta d^{2\beta}]}{2\nu |2\pi f|^\eta} \right] \quad \text{with } a = e^{-\nu |2\pi f|^\nu d^{2\beta}} . \quad (3.16)$$

For this model, the bandwidth limited roughness for spatial frequencies lower than the inverse of the correlation length is proportional to $\sigma \propto \sqrt{\Omega} d^\beta$. In addition, the correlation length is (asymptotically) proportional to d^β as well (derivation in App. A.2).

This novel, empirically modified evolution model is applied in this thesis to analyze rather rough titanium coatings (Sec. 6.2) and the complex interference coating discussed in Sec. 6.3. Moreover, it was used previously by the author of this thesis in [110].

Roughness correlation: The cross-correlation functions $\text{PSD}_{ij} = \langle h_i h_j^* \rangle$ (Eq. 3.7), with h_i the Fourier transform of the i -th interface, have to be assigned with quantitative values under consideration of basic thin film evolution principles. For $i=j$, the PSD models of the previous paragraphs can be applied because they correspond to physically existing interfaces in the multilayer stack. In case of $i \neq j$, the assignment of the PSD_{ij} has to be discussed in more detail, since the cross-correlation can have tremendous influence on the light scattering properties [54,132,140]. The basic correlation models [132]: uncorrelated, fully correlated, and partially correlated roughness - a mixture of the uncorrelated and fully correlated models - were introduced in the late 1970s and are briefly summarized in the following. The kinetic continuum model and the combined model additionally exhibit specific correlation properties that are summarized as well:

- **Uncorrelated:** $\text{PSD}_{ij}=0$ for $i \neq j$ [132,141] so that both interfaces are stochastically independent. This relation exists only in the sense of an ergodic ensemble average, which is induced by large illumination spots in ARS measurements. $h_i h_j^*$ would only be zero for all frequencies if one of the surfaces exhibits no roughness.
- **Partially correlated:** The underlying roughness is perfectly replicated and stochastically independent roughness components are added by the intrinsic thin film roughness for each interface. Therefore $\text{PSD}_{ij} = \min(\text{PSD}_{ii}, \text{PSD}_{jj})$ [132,142].
- **Fully correlated:** No roughening is present within the multilayer stack and the PSD functions for all i and j are identical to that of the substrate: $\text{PSD}_{ij} = \text{PSD}$ [132,141].
- **Continuum partially correlated:** Within the kinetic continuum model [102] (and the combined model) the partially cross-correlation PSD functions are given as:

$$\text{PSD}_{ij} = a^2 \text{PSD}_{ij} = \left(e^{-\nu |2\pi f|^\nu (d_j - d_i)^{2\beta}} \right)^2 \text{PSD}_i \quad \text{with } i < j, \quad (3.17)$$

including the replication factors and potential smoothing effects. This model shows a transition from partially to uncorrelated roughness components with increasing f , since $a^2 \rightarrow 1$ and $a^2 \rightarrow 0$ for low and high spatial frequencies, respectively. The transition corresponds to the beginning cut-off region of the PSD functions.

4. Experimental set-ups for angle resolved scattering measurements

Different approaches for light scattering measurements, focusing on angular resolving measurement systems, are summarized in this chapter. In the first subsection, goniometer based measurement systems - the conventional approach for ARS measurements - are briefly discussed to reveal advantages, but also disadvantages that led to the development of the scattering sensor. To complete the summary of conventional light scattering measurement approaches, the second subsection presents set-ups which comprise multi-detector arrangements as well as set-ups for integrated scattering measurements.

In Sec. 4.3, the light scattering sensor developed in the course of this work is presented in detail including the analyses of system components, system parameters, set-up, and comparable state-of-the-art developments. In addition, physical relations of the general applicability to light scattering and roughness measurements are critically analyzed and the uncertainty budget is discussed.

4.1. Goniometer based set-ups

Goniometer based measurement systems are the most common approaches for angle resolved scattering measurements on optical surfaces [5,11,12,16,143–145], which are utilized since the first half of the last century [146–149]. These systems can provide highest flexibility and sensitivity, which are necessary for the characterization of scattering phenomena from a variety of sources such as interface nanostructures, bulk imperfections, particles, or even liquids and suspensions. Because of this plurality of applications, the system elements (e.g. detector, light source, beam preparation) and the degrees of freedom provide a wide spectrum of implementations and performance levels. However, goniometer type scatterometers usually consist of three main parts: the beam preparation system with the light source; the sample and its adjustment or positioning stages; as well as the detection unit with detector positioners, light analyzing components, and signal processing components.

To obtain the angle resolved scattering, the detector is moved by one of the goniometer arms in a constant radius around the sample. This time-consuming scanning detection is an essential disadvantage of goniometer systems which has prevented the extensive application of light scattering techniques outside the laboratory. For instance a single in-plane scan ($\varphi_s=0^\circ$, $\theta_s=-90^\circ\dots90^\circ$, $\Delta\theta_s=0.5^\circ$; Fig. 4.1, definitions: Sec. 2.1) can take up to 10 minutes; the scan of a complete hemisphere requires between 4 hours and 48 hours,

depending on the angular resolution.

Moreover, the adjustment of goniometer based systems is challenging due to the number of degrees of freedom for sample adjustment and positioning, incidence angle, scattering angles, as well as polarization. Nevertheless, highest sensitivities down to ARS levels below 10^{-8} have been reported [5,11]: It is possible to measure the complete scattering distributions of super-polished surfaces ($\sigma \lesssim 0.1$ nm) [150] or of optical components with sub-ppm scattering losses ($TS < 10^{-6}$) [110].

A state-of-the-art goniometer for 3D-ARS measurements [5], which was developed at the Fraunhofer IOF, is presented in more detail (Fig. 4.1). This system and a recently developed table-top version [11,149,151] were applied in this thesis for cross check measurements and for more extended analyses of scattering models.

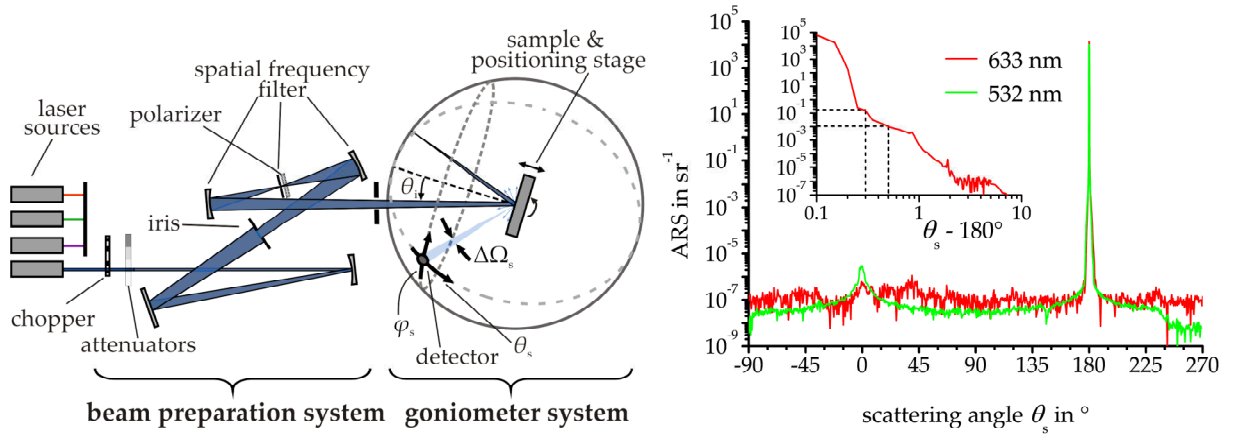


Fig. 4.1.: Left: Scheme of the scatterometer developed at the Fraunhofer IOF - a typical goniometer based instrument for 3D-ARS measurements. Right: Corresponding instrument signatures for 532 nm and 633 nm. Inset to demonstrate the near angular limit.

The scatterometer (Fig. 4.1) is equipped with several laser light sources ranging from the UV over the VIS to the IR spectral regions. Within the beam preparation system, the laser light passes an attenuator stage, necessary to achieve the dynamic range; an iris aperture, to adjust the illumination spot size on the sample; and a mirror based spatial frequency filter, to block system internal stray light and to provide a clean illumination beam profile. In addition, the beam preparation system provides options to include polarizing components or to focus the illuminating beam on the sample surface, if a high local resolution is required.

The diagram in Fig. 4.1 shows instrument signatures for 633 nm and 532 nm that serve to quantify the scatterometer performance. The curves reveal a dynamic range of up to 14 orders of magnitude between the specular power and lowest detectable ARS levels, which is achieved by the attenuators. Moreover, ARS signals as low as 10^{-8} sr^{-1} are accessible by means of lock-in amplification and a photo-multiplier tube, the typical detector for visible wavelengths. The lowest ARS level at 532 nm is determined by the Rayleigh scattering of air molecules [143,144], whereas the lower laser power at 633 nm limits the sensitivity to the electronic noise floor of the detector.

4. Experimental set-ups for angle resolved scattering measurements

Spatial frequency filtering is, in particular, crucial to improve the near angular limit (NAL). The NAL is defined by the scattering angles at which the ARS of a sample in directions close to specular beams and the instrument signature are overlapping. This fact is illustrated by the signature measurement close to the beam (log-log inset, Fig. 4.1): The scattering of samples with ARS levels of 10^{-2} sr^{-1} can be measured up to an angular distance of about 0.5° from the specular beam¹.

The time consuming measurements and the complexity refuse the application of goniometer systems for a high volume of samples in on-line or in-line quality assessment. Even in laboratory applications 3D-ARS measurements are often omitted, while single in-plane ARS scans are preferred. The light scattering sensor developed in the scope of this work is one approach to overcome these limitations.

4.2. Multi-detector and integrating systems

Integrating [20,85,154–160] or multi-detector [17–19,31,161,162] arrangements are two approaches to reduce the time for light scattering measurements. These systems are mentioned to complete the overview about non semi-conductor matrix based scatterometers.

Typical set-ups for integrating TS measurements apply Ulbricht/integrating spheres or Coblentz/imaging spheres to collect the light scattered into a hemisphere onto a single detector. For low scattering samples imaging spheres are preferred, since they provide a higher sensitivity [157,158] as well as noise levels which are less influenced by Rayleigh scattering from air molecules in the specular beam paths [149]. The reduced effort for the data acquisition with integrating set-ups can extremely speed up the measurement rate. For example the system for TS measurements described in [20] is capable to scan a complete 22 mm diameter surface with a high resolution in less than 400 s. However, any isotropy or angularly resolved information is lost and in scattering based roughness measurements only the rms roughness is available.

Intermediate systems between integrating and angle resolving goniometer set-ups are multi-detector arrangements [19,31,162], in which single detectors are positioned at scattering angles that are significant for the measurement task. This concept is for instance widely applied in particle scanner systems [39,40,163] and was, for example, implemented as compact sensor head to monitor the degradation of airplane sensor windows [31].

Other arrangements combine advantages of multi-detector and goniometer set-ups [17, 18,161]: To obtain in-plane ARS distributions in a single shot, detector elements are regularly distributed on a yoke. By moving this yoke, the scattering in the entire hemisphere is accessible in a moderate measurement time.

¹ In a measurement the scaling of the signature by the reflectance or transmittance of the sample will change this level. Moreover, a convolution of the detector field of view with the incident, transmitted, and reflected beams has to be taken into account if the signature floor is determined by Rayleigh scattering from air [152,153].

4.3. Detector matrix based light scattering sensor

4.3.1. Sensor concept and comparison to the state-of-the-art

The basic concept of the light scattering sensor [164,165] that was developed in the course of this thesis consists of two modules: the illumination module to provide a clean beam and the detection module to record a section of the ARS distribution in a single shot measurement. In contrast to conventional goniometer-based set-ups, no moving parts or actuator components are implemented in the modules.

Within the illumination module, the light emitted by a laser diode module passes a compact beam preparation system to reduce system internal stray light and to optimize the instrument signature. The detection module consists of a CMOS detector matrix and an arrangement of beam dumps, which absorb and redirect re-reflexes of the specular beam from the detector matrix. In general, the arrangement of the two modules is flexible regarding incidence angle, covered scattering angles, or illumination wavelength. Nevertheless, fixed arrangements that can be implemented in compact housings (Fig. 4.2) are required for the final applications as easy to handle light scattering sensor for in-line quality assessment.

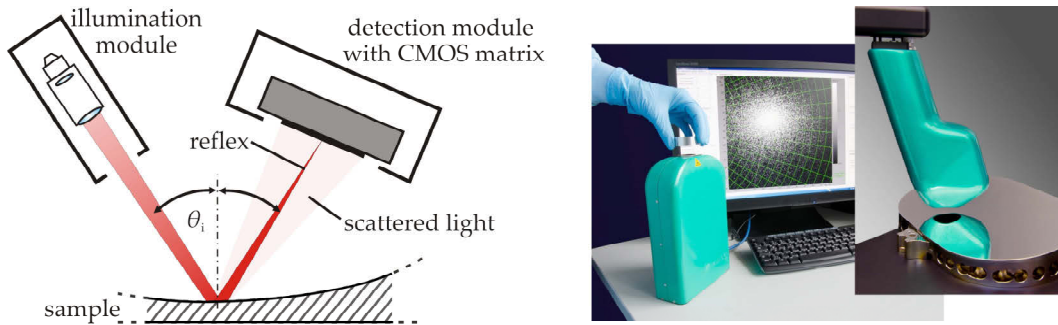


Fig. 4.2.: Left: Scheme of the modular sensor concept. Right: Two implementations of the concept in form of compact scattering sensor heads.

Through the application of a CMOS detector matrix, the sensor concept provides the capability to measure a section of the 3D-ARS distribution - the h ARS - within a single shot measurement. However, the scattering angles covered by the detector module are limited, since commercial planar CMOS camera chips provide only few square centimeters of sensitive area. Nevertheless, it will be demonstrated that this limited part of the ARS is sufficient for elaborated roughness, anisotropy, and defect analyses, since essential information is located in the scattering close to the specularly reflected beam.

The application of semiconductor matrices for light scattering measurements has been reported in a number of publications. In the following paragraphs, different approaches and systems are reviewed, for which the best reported operation parameters are summarized in Tab. 4.1. In particular two measurement systems those basic approaches are similar to the sensor system presented here are presented and analyzed in detail.

In 1985 [30,166] one of the first applications of a photo-diode line to assess nanostructure

4. Experimental set-ups for angle resolved scattering measurements

properties of rough surfaces (minimal $R_a \approx 10$ nm,² [166]) from scattering distributions is reported. Almost identical applications of diode or CCD lines are presented in [90,167–171] and were implemented as commercial sensor devices [172–174] for fast in-line scattering based measurements of technically rough surfaces.

So far, only uncalibrated scattering distributions were reported for these systems; therefore, their sensitivity in terms of ARS or BRDF is not accessible. However, since the measurable roughness, which is determined using the semi empirical facet model [166], seems to be limited to values of about $R_a \gtrsim 10$ nm, the application for optically smooth surfaces ($\sigma < 1$ nm) is not possible. In addition, the scattering data is limited to the in-plane ARS with angular resolutions of only 1° . Consequently, the evaluation of naturally three dimensional ARS distributions [175] with a fine structure, in particular those of anisotropic surfaces or defects, is not practicable.

For the systems described in [30,166,168,169] an additional sensitivity limiting factor is the application of optical elements to image the scattering distribution on the detector. The negative impact, which is in particular relevant for the instrument signature and the NAL, is caused by the scattering from the imaging elements and by internal reflections [167]. Moreover, pattern distortions [167] as well as radiometric and angular distortions [57] can be induced.

Imaging elements are also limiting factors for the multiplicity of measurement systems that use a combination of imaging spheres, non-spherical mirrors, lenses, or objectives with 2D semiconductor matrices to record the scattering of the complete hemisphere [24,29,37,38,176–178] or of sections of the hemisphere [33,115,179–182]. This limitation is either caused by obscuration [24,29,37,177] or by scattering and multiple reflections from the imaging elements [183].

Systems utilizing a combination of an imaging sphere and a semiconductor matrix for ARS measurements, first reported in [176], can be rather similar to imaging sphere based TS measurement set-ups; only the integrating detector has to be replaced by a spatially resolving detector module close to the conjugated focal point [176,178].

These systems can be quite sensitive (Tab. 4.1, [29]) and are applied to characterize various scattering phenomena: for instance the scattering from particle chains in magnetorheological suspensions [24] or from airborne particles [25,179]. The application to the 3D analysis of surface roughness induced scattering was reported in [29,37,38,180] with achieved sensitivities down to roughness levels in the nanometer regime [29]. However, the systems are often non-compact laboratory systems [24,37,38] and, therefore, not suited for in-line applications.

For systems that employ optical elements, an additional sub-class exists with at least four instruments described in [34,36,184–188]. By these systems the scattered light distributions are recorded from diffusing screens or hemispheres. Hence, blurring effects of

² R_a is the 2D version of S_a (arithmetic mean deviation of a 3D surface profile). For surfaces with a Gaussian height distribution: $\sigma \approx \sqrt{\pi/2} S_a$ [62].

the specular beam within the imaging screens constitute additional sources of interfering light that limits the capabilities to evaluate the scattering close to the specular direction.

Besides for the systems in [29,34,37,177], neither calibrated ARS nor BRDF measurements were presented in the reviewed publications and only in [29] the rms roughness was determined from the measured TS values. Therefore, the structure-scattering-relationships presented in Sec. 3.1, which require calibrated scattering data, have not been applicable so far for the other systems.

Tab. 4.1.: The upper part of the table compares semiconductor matrix based concepts for light scattering measurement and lists their best reported performance parameters. The lower part compares performance parameters of sensors whose basic concepts are similar to the sensor in this work. "DR in OoM" - dynamic range in orders of magnitude; "Sens in sr^{-1} " - sensitivity down to ARS levels in sr^{-1} ; * no calibrated ARS/BRDF data available; † determined from the bit depth of the semiconductor sensor device.

Sensor concept	Advantages	Disadvantages	θ_s range / $\Delta\theta_s$ in $^\circ$	Sens in sr^{-1}	DR in OoM	Lowest σ or R_a in nm
2D-ARS (detector line) [30,167–169,172,189]	+ compact + very fast	– resolution – dynamic – θ_s, φ_s -range	$\pm 15^\circ \dots \pm 20^\circ$ $\Delta\theta_s = 1^\circ$ [30,172]	n.a.*	4.6 † [30]	$R_a = 5$ [168]
3D-ARS + imaging element [25,29,37,38,115, 176,179–183,190]	+ sensitivity + fast + (θ_s, φ_s -range)	– NAL – (size)	$\theta_s = 6^\circ \dots 90^\circ$ $\Delta\theta_s = 0.4^\circ$ [29]	$< 10^{-5}$ [29]	7 † [182]	$\sigma = 2$ [29]
3D-ARS + image screen [34,36,184,185, 187,188,191]	+ fast + (θ_s, φ_s -range)	– NAL – (dynamic) – (size)	$\theta_s = 0^\circ \dots 85^\circ$ $\Delta\theta_s = 0.35^\circ$ [191]	10^{-3} [34, 184]	6 [184]	$R_a = 12$ [185]
3D-ARS, direct measurement	+ dynamic + sensitivity + NAL + compact + fast	– θ_s, φ_s -range	9° around reflex $\Delta\theta_s < 0.01^\circ$	5×10^{-5}	7.6	$\sigma < 0.5$
Set-ups for direct 3D-ARS measurements	Detector	Source, λ in nm	θ_s range / $\Delta\theta_s$ in $^\circ$	Sens in sr^{-1}	DR in OoM	Lowest σ or R_a in nm
PSS [28,192]	retina shaped CMOS matrix, 8013 elements	laser diodes, 686, 820	8° around reflex $\Delta\theta_s = 0.03^\circ \dots 0.38^\circ$ $\Delta\varphi_s = 2^\circ$	4×10^{-3}	7	$\sigma = 5$
by Lu, Tian [193,194]	rectangular CCD matrix	n.a.	n.a.	n.a.*	2.4 †	$R_a = 50$
scattering sensor	rectangular commercial CMOS matrix	laser diodes, 660, 405	9° around reflex $\Delta\theta_s < 0.01^\circ$ $\Delta\varphi_s < 0.03^\circ$	5×10^{-5}	7.6	$\sigma < 0.5$

So far not mentioned, since to less data on the working approaches are available, were the commercial systems "MiniDiff" [35] and "OMS2" [27]. With both systems, calibrated BRDF distributions can be determined. However, from the applications presented, it seems that both systems are intended for the photometric rendering related evaluation

4. Experimental set-ups for angle resolved scattering measurements

of surfaces and, therefore, do not provide the sensitivity and illumination beam quality required for the characterization of optically smooth surfaces.

There are only two light scattering measurement systems known to the author, presented in [28,192] and [193,194], which apply (2D-)semiconductor matrix detectors in a similar configuration as the scattering sensor in this thesis (directly, without any imaging elements). In the lower part of Tab. 4.1 (p. 23) the reported performance parameters of these systems are compared to the novel sensor developed in the course of this thesis.

For the set-up described by Lu and Tian in [193,194], the characterization of surfaces with rather high roughness values not below $\sigma=50$ nm was demonstrated. For this purpose, the uncalibrated scattering distributions were evaluated with a model [195] that is comparable to the facet model [166].

Calibrated BRDF measurements down to levels of $\text{BRDF} \approx 4 \times 10^{-3} \text{ sr}^{-1}$ and obtained 3D-PSD functions of medium rough surfaces ($\sigma \approx 5$ nm) were reported for the system "PSS" described in [28,192]. In this sensor a specially developed retina shaped CMOS sensor [28] with a radial arrangement of the single CMOS elements and logarithmic response is implemented. However, no scattering measurements were reported for samples with roughness values lower than $\sigma \approx 5$ nm and the measurements presented indicate a NAL not better than $\text{ARS} \approx 1 \text{ sr}^{-1}$ at $\theta_s = 0.5^\circ$.

In order to characterize the scattering of typical optical surfaces a sensitivity of at least $\text{ARS} \lesssim 10^{-4} \text{ sr}^{-1}$ is necessary. An estimation based on Eq. 7 for pure roughness induced scattering from surfaces with a fractal PSD and a scattering relevant roughness³ $\sigma = 0.4$ nm reveals a required sensitivity down to $\text{ARS} \approx 10^{-4} \text{ sr}^{-1}$ for an ideally reflecting surface and even $\text{ARS} \lesssim 10^{-5} \text{ sr}^{-1}$ for an identically rough glass substrate with a reflectivity of 4 %. Therefore, a sensitivity of $\text{ARS} \lesssim 10^{-4} \text{ sr}^{-1}$ is sufficient for commercial mirrors and even partially for super-polished RG1000 substrates or silicon wafers, as will be demonstrated.

On the other hand, a NAL of $2 \times 10^{-2} \text{ sr}^{-1}$ and a dynamic range of at least 3 orders of magnitude are required to cover the scattering of this model surface up to 0.5° close to the specular direction. An even higher dynamic range would be necessary for the characterization of smooth and moderately rough surfaces with the same instrument. These requirements are fulfilled by the scattering sensor presented in this thesis, which is the most sensitive sensor known to the author with 3D capability and without interfering imaging elements in front of the detector.

4.3.2. Discussion of technical details

General set-up

In the basic set-up (Fig. 4.3) an angle of incidence of $\theta_i = 18^\circ$ was chosen and the specular reflected beam is focused on the center of detector matrix in a distance of 52 mm from the sample. This arrangement results from a tradeoff concerning coverage of an

³The PSD parameters were: $K=5000$ and $n_K=1$; $\lambda=660$ nm

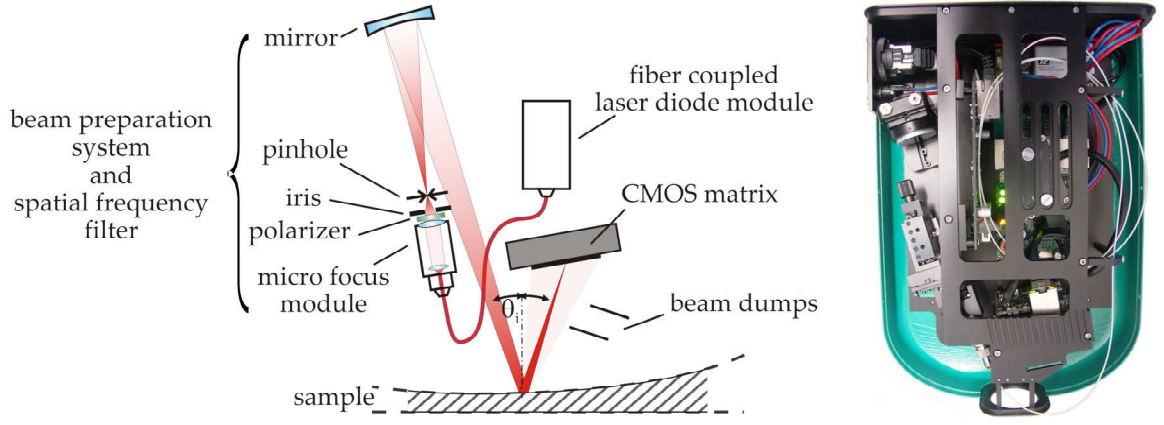


Fig. 4.3.: Scheme of the basic set-up (left) and photography of the corresponding sensor head (right).

extended section of the scattering hemisphere, collection of significant information, and implementation of a compact sensor head.

PSD functions are typically plotted in double logarithmic diagrams and, therefore, bandwidth limits of the related roughness values are given in decades. This fact is presumably a result of the fractal nature of many (polished) surfaces. In consequence, light scattering measurements should span a wide range in logarithmic spatial frequencies, too.

The grating equation (3.2) reveals that within a fixed, limited angular range the highest spatial frequency range (log scale) is achieved close to the specularly reflected beam. In addition, it is advantageous to cover a solid angle symmetrically centered on the reflex for the anisotropy analyses and for the defect assessment presented later. Consequently, the specularly reflected beam is positioned in the center of the CMOS matrix.

A short distance between the sample and the detector matrix increases the covered section of the scattering sphere and increases the solid angle per pixel. The latter is advantageous for the sensitivity, since the power of scattered light per pixel is increased. However, at least several centimeters of working distance are required to handle parasitic reflections from the detector matrix and to implement a compact sensor head with a moderate angle of incidence. With a distance of 52 mm and $\theta_i \geq 18^\circ$ the illumination beam can pass the rather large solid angle covered by the electronics ($\Delta\Omega \approx 0.9$ sr) which surround the active CMOS area ($\Delta\Omega \approx 0.1$ sr).

In contrast to goniometer systems, the sensor concepts omits any moving system components. The solely mandatory requirement is the correct positioning of the sample in front of the sensor on a (adjustable) sample stage.

Illumination module

The illumination module is designed to provide a clean beam that is focused on the detector, has a defined divergence, and provides a defined spot diameter on the sample surface. The focus on the detector is necessary to detect the scattering close to the specular direction and to ensure the far-field regime inherent to Eqs. 3.1 and 3.7 (see p. 39). The quality of the focus as well as the level of system internal stray light determine the near

4. Experimental set-ups for angle resolved scattering measurements

angular limit (NAL) and the other parts of the instrument signature; hence, they define the angular range in which the sensitivity of the system is not limited by signature effects. The specific requirements to the beam preparations system in the compact sensor design are discussed in the following paragraphs.

Laser diode modules, emitting at $\lambda=405$ nm or 660 nm, with powers of 75 mW or 40 mW, respectively, were applied as light sources. For both wavelengths, compact modules with sufficient powers are available, since their development presumably profited from the application of these wavelengths in DVD or BluRay players. In addition, the detector matrix has its quantum efficiency maximum (50%) at about 670 nm and provides an acceptable quantum efficiency of 25% at its lower band edge at 405 nm [196].

The following paragraphs deal with the optimization of the instrument signature for the 660 nm module in the primary illumination channel. Information on the application of the 405 nm module, in a secondary illumination channel, can be found in Sec. 6.2.1, in which its application for the characterization of titanium films is discussed.

In Fig. 4.4 measured instrument signatures for beam preparations modules with a lens or a mirror as final element of the spatial frequency filter are anticipated. These elements image the intermediate focus in the pinhole over the (reflecting) sample on the detector matrix. In addition, modeling results which combine VPT and Zemax ray-tracing results are depicted to identify the contributions of different set-up elements to the signature.

In a first set-up (Fig. 4.4, left), whose signature was dominated by a disk like ghost image with an $hARS$ of about $5 \times 10^{-2} \text{ sr}^{-1}$, the last imaging element was a super-polished fused silica plano-convex lens ($\sigma \lesssim 0.3 \text{ nm}$,⁴ $f=39 \text{ mm}$). The different contributions to this signature were identified from the modeling as lens-internal reflexes, re-reflexes from both lens surfaces over the pinhole, as well as roughness induced scattering from the lens. In particular the re-reflections emerging from the plane lens side provide the dominating contributions to the more than 4° wide disk in the signature. Even if a blackened pinhole was applied, the scattering level of the disk only drops less than two orders of magnitude to $hARS \lesssim 10^{-3} \text{ sr}^{-1}$.

For a tilt of the lens of 10° , the re-reflex contributions could be considerably reduced; only a decentered but with $hARS \approx 10^{-3} \text{ sr}^{-1}$ lower disk is still formed by the re-reflexes from the convex lens side⁵. However, additional effects not revealed in the modeling and aberrations still limit the NAL to a cone of up to more than 1° with $hARS > 1 \text{ sr}^{-1}$. In particular the extended tail in the near angular profile, possibly caused by multiple reflections of the element scattering, was only indicated by the aberrations in the modeling.

Further deviations of measurement and modeling are attributed to sources not included in the modeling such as lens bulk scattering or re-reflections from other mounting elements. Thus, in the context of scattering measurement systems, ray tracing simulations can only

⁴ relevant roughness at $\lambda=660 \text{ nm}$

⁵ Lenses with anti-reflective coatings also caused re-reflexes, showed increased sensitivity to contamination, and were less resistant to cleaning. The latter facts are mentioned, since it was recognized that even small particles or slight contamination significantly increase the instrument signature.

reveal an incomplete prediction of possible instrument signatures, which is only as good as the number of contributions included. Nevertheless, ARS based PSD determination had been already possible with the lens based set-ups for medium rough surfaces.

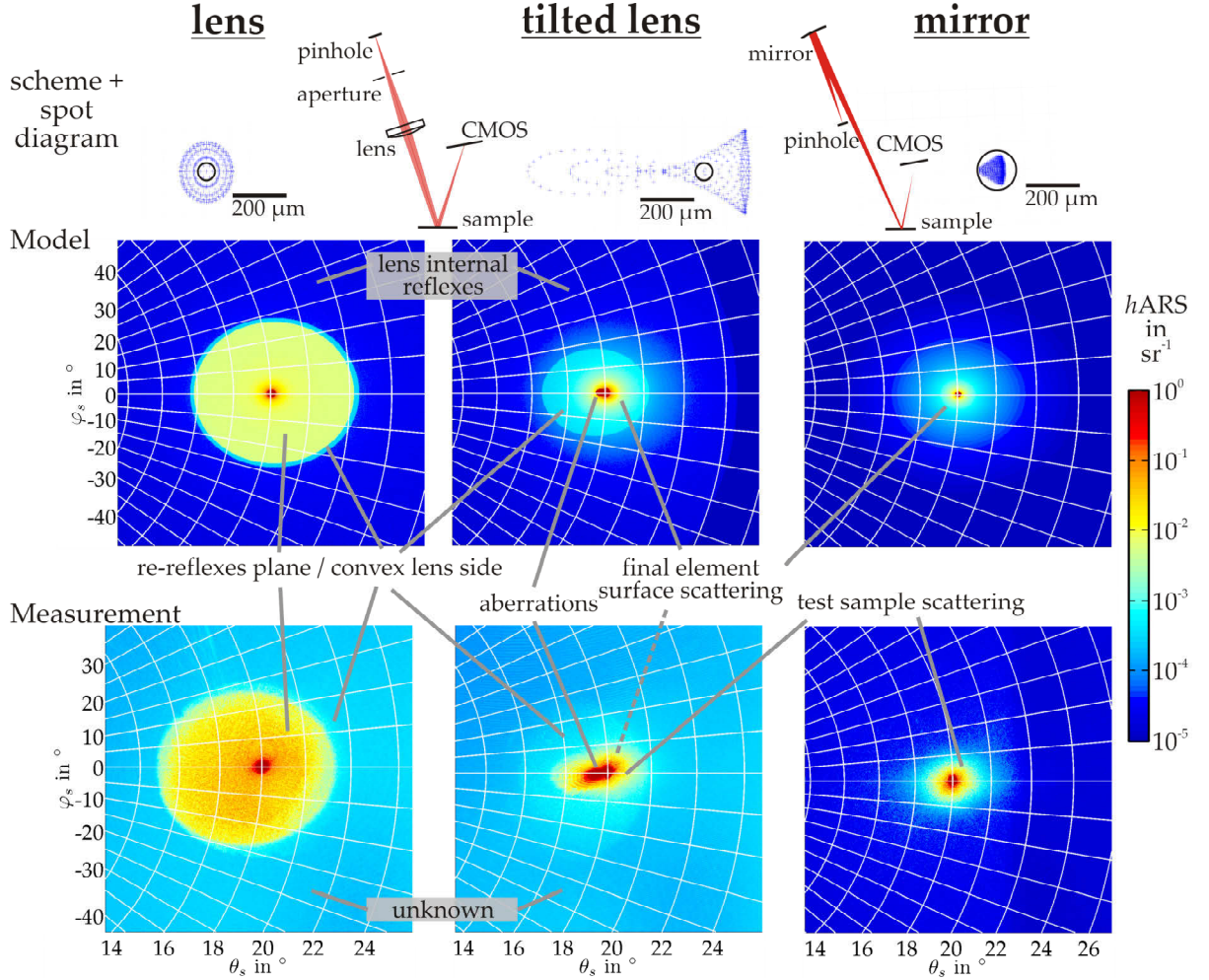


Fig. 4.4.: Chain of beam preparation and signature optimization; from left to right: plano-convex lens and tilted plano-convex lens based systems, both with pinhole diameters of $150\mu\text{m}$; mirror based system with a fiber coupled laser diode module and $70\mu\text{m}$ pinhole diameter.

A mirror based beam preparation system, as typical for highly sensitive goniometer systems [5,13,62], with a concave mirror ($f=62.5\text{ mm}$) as imaging element was analyzed and implemented in the final sensor. Ray-tracing revealed that at an angle of incidence of 3° the corresponding aberrations are within the limit of the Airy disk; hence, the spot on the CMOS matrix is diffraction limited and the NAL is not influenced by aberrations. However, an off-axis pinhole adjustment stage had to be developed to fold the beam path and to achieve a module size as compact as the lens based illumination module.

The increased distance between the final imaging element and the detector has two effects on the instrument signature: On the one hand, the influence of the element scattering is decreased, since its signature relevant ARS has to be down-scaled by the ratio of the squared distances of sample-detector and element-detector. On the other hand, the scattering angles are spread by the increased distance; an effect that can counteract the down-scaling if the slope of the imaging element PSD exceeds $n_K > 1$ [149]. Since the n_K

4. Experimental set-ups for angle resolved scattering measurements

of the mirror is 0.9, increasing the distance should improve the signature.

VPT modeling with identical PSD functions for all surfaces revealed that the scattering of a mirror is about ten times higher than that of a lens in the transmission hemisphere. However, the surface PSD of the mirror is about ten times lower than that of the lens surface⁶ so that the modeling revealed a signature relevant scattering that is slightly below that of the lens (Fig. 4.4).

Additional advantages of the mirror based beam preparation are the reduced aberrations, the single scattering surface, the absence of bulk scattering, and the reduced sensitivity towards contamination and particles, recognized in the application tests. Disadvantages, however, are the higher magnification of the pinhole image on the detector and the increased Airy disk, which both slightly reduce the near angular limit.

Differences of measurement and model in the near angular scattering for the mirror based system are caused by roughness of the silicon wafer, which was applied as "ideally smooth" sample for the signature tests. Hence, close to specular reflex it is even possible to measure the scattering of superpolished silicon wafers (see Fig. 4.8, on p. 32).

In the lens set-ups and the first mirror set-up, a very compact but simple laser-diode module with a focusing lens and an elliptical beam profile [197] was implemented. In the final illumination module it was replaced by a slightly bigger, fiber-coupled laser-diode module [198]⁷. The polarization maintaining single mode fiber acts as an additional beam shaping element that provides an almost Gaussian beam profile. In combination with a micro-focus module, the diameter of the pinhole could be reduced from 150 μm to 70 μm . This results in an additional reduction of the focus diameter on the detector by a factor of 2 from 420 μm to 210 μm ; hence, the theoretical near angle limit (in absence of element scattering) is improved to about 0.12°. The illumination spot on the sample is only reduced by 20 % from 1.9 mm to 1.5 mm.

At the aperture of the micro-focus module, an iris and a polarizer are located to adjust the spot diameter on the sample and to increase the polarization contrast, respectively.

Detection module

To maintain the simplicity of the sensor concept, a commercial CMOS detector matrix (Photon Focus MV1-D2080-160G2-12 [196]) was implemented into the set-up. Key parameters of this module are: an active area of 16.64×16.64 mm², 2080×2080 detector elements, and an exposure time range from 10 μs to 419 ms. The corresponding sensitivity should be below $h\text{ARS}$ level of about $5\times 10^{-5} \text{ sr}^{-1}$, which corresponds to a gray value (GV) of 66. In this rough estimation a laser power $P_i=40 \text{ mW}$, the maximum exposure time $t_{\text{int}}=0.419 \text{ s}$, a solid angle $\Delta\Omega=2.4\times 10^{-8} \text{ sr}$, and a CMOS pixel responsivity $\Re=210\times 10^3 \text{ DN m}^2/\text{J}$ [196] were assumed.

⁶ 0.1 nm compared to 0.3 nm relevant roughness at $\lambda=660 \text{ nm}$, although mirror and lens were purchased from the same supplier.

⁷ The fiber port facilitates the application of wavelengths for which no compact sources are available.

Although CCD matrices provide higher sensitivities, higher fill factors, and less noise, they are prone to blooming or smearing effects if they are illuminated by high intensities [199–202]. In combination with the high integrations times, which are required to record low level scattering, extremely high saturated pixels have to be expected in the specular reflex. Therefore, CMOS matrices whose images are not prone to smearing and much less prone to blooming are necessary⁸.

Even 16 bit sensors cannot cover the full dynamic range of the ARS between the specular power and low scattering levels. Therefore, an image series obtained over the entire range of exposure times extends the dynamic range of only 8 bit per image⁹ to about 7 decades (≈ 23 bit, Sec. 4.3.2). A good linearity of the detector over this entire dynamic range is mandatory for reliable ARS results. To correct possible non-linearities, the response characteristics of the CMOS matrix were analyzed by using the set-up sketched in Fig. 4.5 and the procedure described in the following:

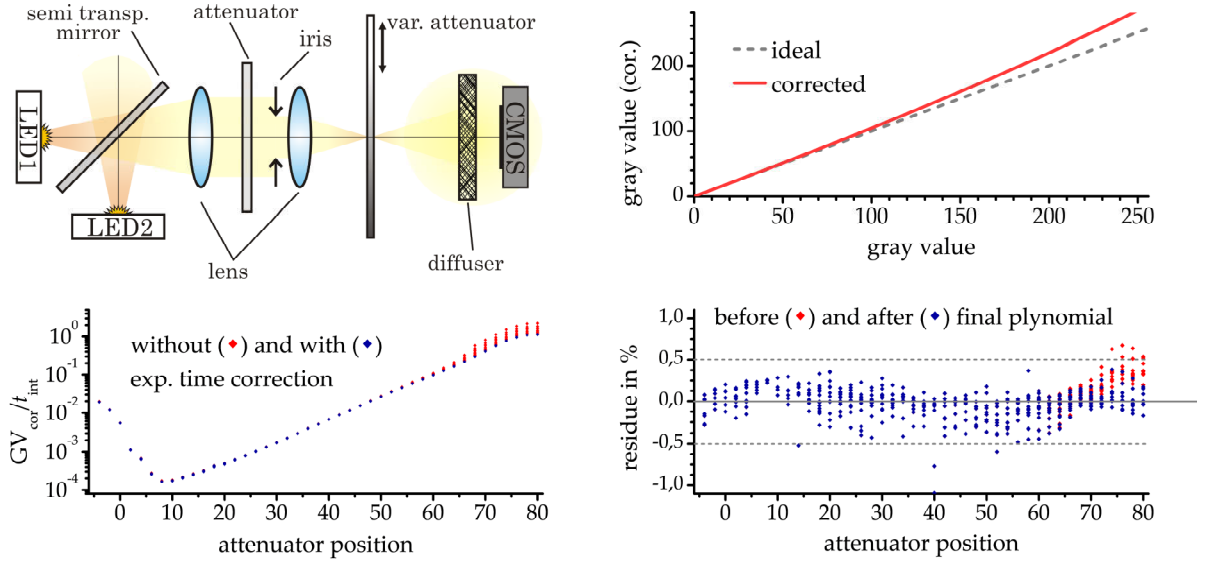


Fig. 4.5.: Results of CMOS matrix linearity analysis: Scheme of the set-up (top left); diagram of the correction polynomial for the background corrected gray values (applied for all integrations times). The diagrams in the lower row demonstrate the necessity for the exposure time correction (left) and summarize the remaining residue (right) after all correction steps.

The CMOS matrix was illuminated by two high power LED sources whose light was combined by a semitransparent mirror. The light passes a variable attenuator¹⁰ in an intermediate focus to generate different illumination powers, which is followed by a transparent diffuser to homogenize the illumination. According to the superposition method described in [204–206], the primary aspect in the linearity test is the comparison of the sensor output obtained with both LEDs switched on to the sum of the gray values ob-

⁸ Nevertheless, even this matrices are not applicable in general. For example a CMOSIS CMV4000 chip [203] tested showed the black sun effect if illuminated by the focused laser beam.

⁹ The 8 bit mode was applied, since the 12 bit mode primarily increases the resolution of noise.

¹⁰ The (unknown) attenuation is not required for the procedure. Hence, only the attenuator positions are given.

4. Experimental set-ups for angle resolved scattering measurements

tained for either LED 1 or LED 2 switched on. This has to be done for integration times and attenuation levels that cover the entire dynamic range.

In contrast to photo multiplier tubes and photo diodes, which produce continuous signals, the CMOS detector elements collect the generated charges over the exposure time and a digitized gray value (0...255) proportional to t_{int} is returned. A further major difference is the high dark signal which can range from 7 % to 35 % of maximum gray value $\text{GV}=255$. Therefore, the linearity of the signal is analyzed as a function of the gray value and the exposure time, considering a pixel-wise subtractive background correction. Following the superposition method [204–206], a correction polynomial for the signals is set up, which is directly applied to the background corrected gray values GV^* . The coefficients b_i are determined by minimizing the sum of the resulting residue for different illumination levels: $\text{GV}_{1\&2}^* - \text{GV}_1^* - \text{GV}_2^* + \sum_i b_i \left((\text{GV}_{1\&2}^*)^i - (\text{GV}_1^*)^i - (\text{GV}_2^*)^i \right) = 0$. For the exposure times tested, the b_i revealed only slight deviations; therefore, the identical second grade polynomial was applied for all exposure times (Fig. 4.5, top right).

The GV_{cor} signal, corrected by the polynomial and divided by the integration time, revealed a remaining non linearity that became evident in the comparison of identical signals for different exposure times (Fig. 4.5, bottom left) in particular for $t_{\text{int}} < 200 \mu\text{s}$. These deviations were corrected by adding a constant $t^* = 20 \mu\text{s}$ to t_{int} , which primarily influences the signals at low exposure times and significantly minimizes the deviations. The success of this procedure indicates possible deviations in the sensor chip timing.

After both corrections, the remaining residue $\text{GV}_{\text{cor},1+2} - \text{GV}_{\text{cor},1} - \text{GV}_{\text{cor},2}$, which are given in Fig. 4.5, are already below 1 %. By applying an additional polynomial, the remaining deviations (right part, Fig. 4.5, bottom left) drop to an average residue level below 0.5%. The final corrected signal is determined as:

$$V_{\text{cor}} = \text{GV}_{\text{cor}} + \sum_j c_j \text{GV}_{\text{cor}}^j \quad \text{with} \quad \text{GV}_{\text{cor}} = \frac{\text{GV} - \text{GV}_{\text{HG}} + \sum_i b_i (\text{GV} - \text{GV}_{\text{HG}})^i}{t_{\text{int}} + t^*} \quad . \quad (4.1)$$

Although the CMOS matrix has an anti-reflective coating, a diffraction pattern emerges from the reflex position on the grating like matrix structure. Without countermeasures, scattering or retroreflection of these reflexes at the housing or the sample considerably contribute to the instrument signature. To avoid this, the matrix normal is tilted by 28° with respect to the specular reflex; then, the most intense orders of the diffraction pattern are removed from the sensor field of view by an arrangement of opaque, low reflecting RG1000 glass surfaces (Fig. 4.3, p. 25).

Measurement and calibration procedure

For measurements of the $(h)\text{ARS}$, the quantities ΔP_s , $\Delta \Omega_s$, and P_i in Eq. 2.1 have to be determined. The corresponding procedure with the specifics required for sensor measurements are described in the following and are illustrated in Fig. 4.6.

The scattered power ΔP_s is proportional to the corrected signal V_{cor} (Eq. 4.1). However,

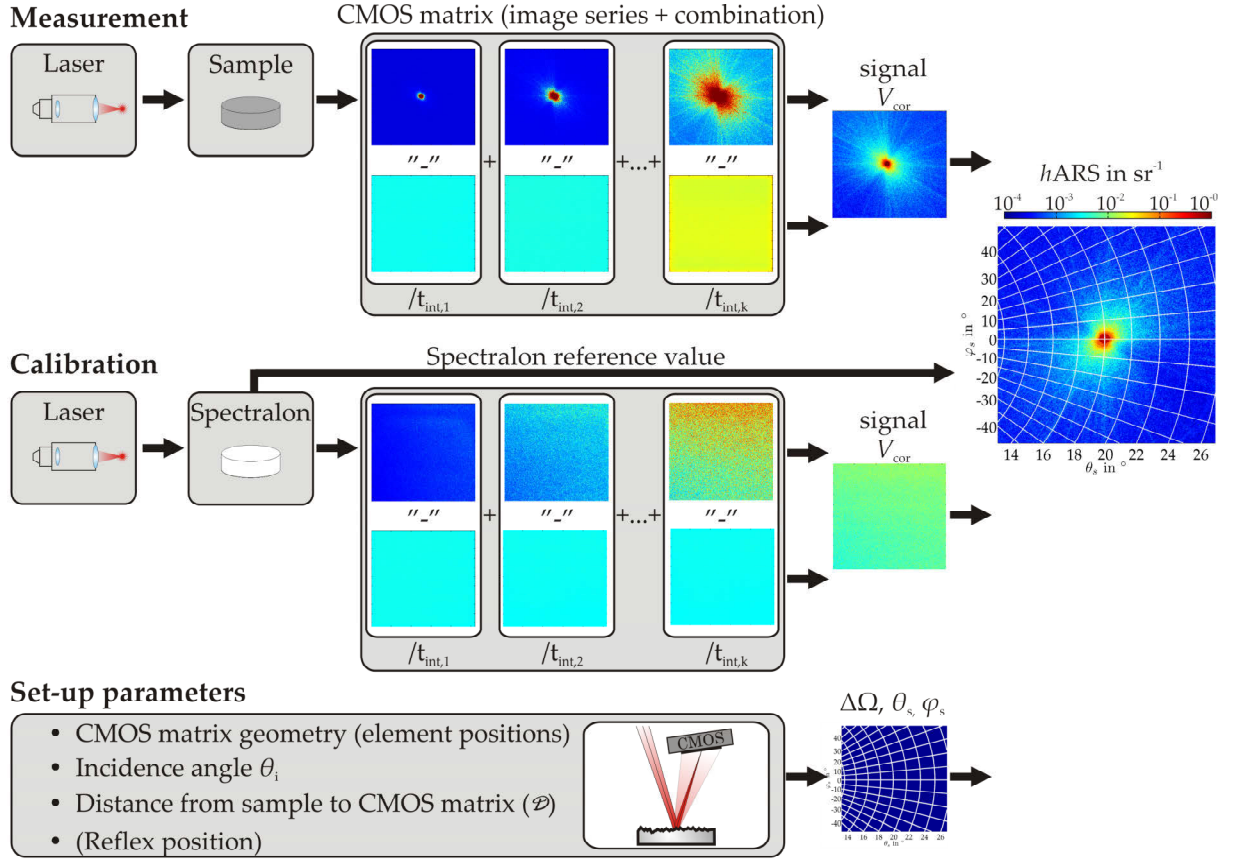


Fig. 4.6.: Scheme to illustrate the measurement procedure

a series of scattering images with different exposure times has to be recorded and combined to cover the high dynamic range of ARS distributions:

$$\Delta P_s \propto \frac{1}{\sum_k I_k} \sum_k I_k V_{\text{cor},k} \quad \text{with} \quad I_k = \begin{cases} 0 & \text{for } GV_k > 250 \\ 1 & \text{else} \\ 0 & \text{for } GV_k < 1.3 \langle GV_{\text{HG},k} \rangle \end{cases} . \quad (4.2)$$

The function I_k ensures that only gray values that are neither saturated nor close to the noise level are included in the determination of the scattering signal. To further extend the measurement dynamic, it is possible to change the laser power from 1 mW to 40 mW and to combine the resulting $h\text{ARS}$ curves as well.

The direct measurement of a signal proportional to the incident power P_i is impossible, since the power in the focused specular beam exceeds the saturation level of the CMOS chip¹¹. Therefore, as common for ARS measurements, a highly-scattering reference sample (e.g. spectralon®) with a known scattering distribution ARS_{Ref} is used to determine a signal proportional to P_i via the ARS definition (Eq. 2.1):

$$P_i = \frac{\Delta P_s}{\text{ARS}_{\text{Ref}} \Delta \Omega_s} \propto \frac{1}{\text{ARS}_{\text{Ref}} \Delta \Omega_s} V_{\text{cor}} . \quad (4.3)$$

¹¹ Attenuation of the incidence power would reduce the robustness of the calibration procedure, since the small number of pixels covered by the focused beam would induce additional uncertainties.

4. Experimental set-ups for angle resolved scattering measurements

ARS_{Ref} of the spectralon was determined from a BRDF measured at normal incidence at the Physikalisch Technische Bundesanstalt, Braunschweig¹². The deviation \mathfrak{s} from an ideal Lambertian BRDF, which is approximately constant within the angular range of the scattering sensor, is determined so that $\text{ARS}_{\text{Ref}} = \mathfrak{s} (\cos \theta_s / \pi)$. In addition, a goniometer system was used to verify the negligibility of differences in the ARS_{Ref} for $\theta_i = 18^\circ$ compared to normal incidence [207]. To reduce the influence of speckles and detector noise, an averaging over the incident power determined for each detector pixel is performed.

For the determination of the ARS and the evaluation of Eq. 4.3, the solid angle of each pixel has to be determined. This is done by a geometrical analysis of the tilted CMOS matrix plane within the scattering geometry and by the transformation of the matrix coordinates into the spherical scattering coordinates. Spherical geometry [Sec. 3.4 in 208] enables the determination of the corresponding $\Delta\Omega_s$ from the pixel grid.

To correct for slight deviations of the specular reflex position, the coordinate system is calculated by performing a virtual shift of the CMOS matrix in its plane and by setting the current reflex position as ideal reflex position. This reflex tracking is further justified in the context of the uncertainty evaluation (Sec. 4.3.3, p. 38).

For an in-line or in-situ application of the sensor, the presented procedure can be simplified if uncalibrated, relative measurements or reduced dynamic ranges are sufficient. The reduced computational effort increases the measurement speed so that the measurement rate can reach the frame rate of the CMOS matrix (25 fps). To further reduce the amount of data and to speed up post measurement calculations, a combination (binning) of 4×4 pixels is an additional software option.

Measurement results and performance parameters

The h ARS measurements of a diamond turned aluminum sample, a superpolished silicon wafer, and the direct beam profile are illustrated in the Figs. 4.7 and 4.8 to demonstrate the dynamic range, the instrument signature, and the sensitivity of the sensor. In addition, a comparable ARS section of the diamond turned sample recorded with a goniometer system is depicted in Fig. 4.7. In order to obtain a similar resolution for the central ARS part (green frame), the smallest detector aperture ($\varnothing = 0.2 \text{ mm}$, $\Delta\Omega = 5.9 \times 10^{-7} \text{ sr}^{-1}$) and angular steps of $\Delta\theta_s = 0.025^\circ$ and $\Delta\varphi_s = 0.1^\circ$ were applied. This highly resolved goniometer scan lasted already 30 hours, whereas the sensor measurement took only 8 seconds.

The PSD_{2D,iso} functions in Fig. 4.8 are shown to demonstrate the spatial frequency range covered in sensor measurements and the PSD relevant instrument signature.

- The **time** for a measurement with the highest resolution, including the exposure time series and computation time of h ARS and PSD, is about 8 s. However, this time can be reduced by more than a factor of 10 through omitting the exposure time series and calculating the roughness from an integrated S value (Eq. 3.3). In this configuration

¹² Measurements were performed in the context of the scatterometer development in [149].

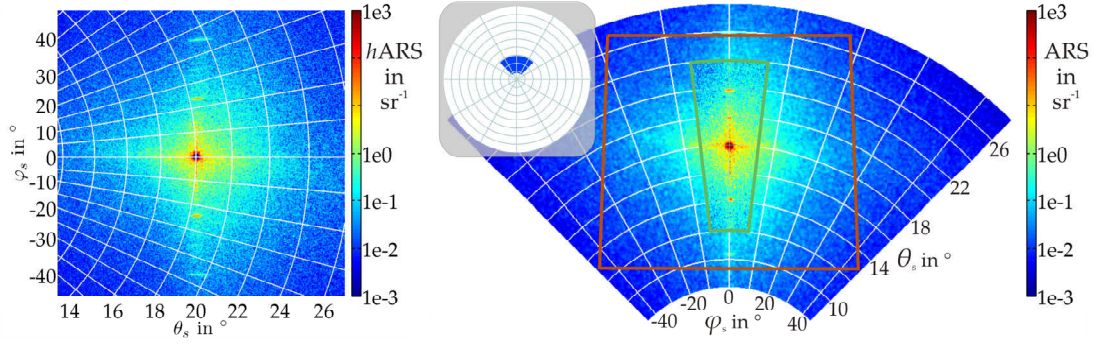


Fig. 4.7.: Scattering distribution of a diamond turned aluminum surface measured with the light scattering sensor (left) and the table-top goniometer (right). The red frame indicates the section which is covered by a sensor $hARS$; the inset the section of the scattering hemisphere covered by the goniometer measurement. The data in the green frame was obtained in a 30 hours goniometer measurement ($\Delta\theta_s=0.025^\circ$, $\Delta\varphi_s=0.1^\circ$).

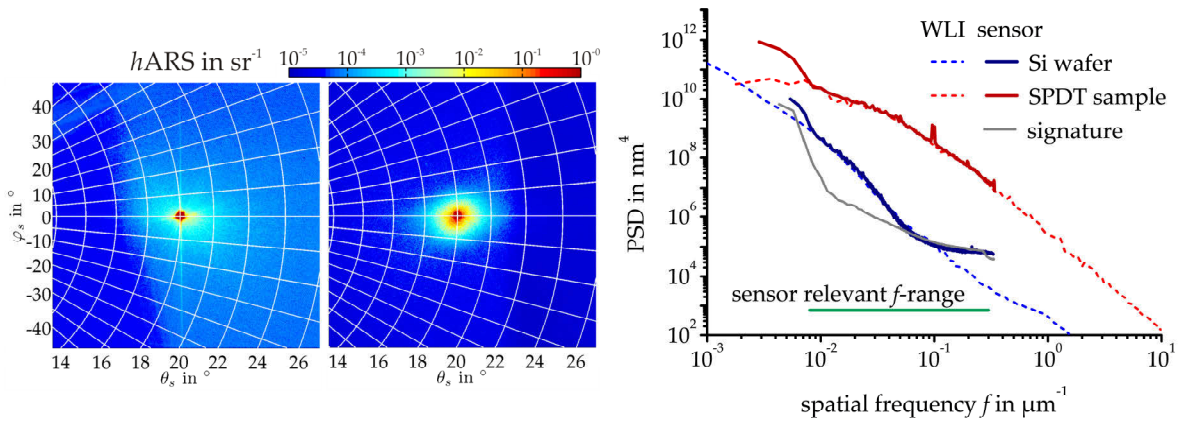


Fig. 4.8.: Instrument signature obtained with the CMOS matrix positioned in the transmission hemisphere (left) and $hARS$ of a silicon wafer (center). PSD functions determined from these measurements and the diamond turned sample (SPDT sample, right).

more than 6 measurements per second become possible. Moreover, the sensor enables uncalibrated scattering images or S values to be observed in real-time (25 fps).

- **Angular resolution:** Caused by the projection of the plane CMOS grid into the light scattering hemisphere, the resolution is changing over the matrix. Nonetheless, a fine average angular resolution as low as $\Delta\theta_s \approx 0.0075^\circ$ and $\Delta\varphi_s \approx 0.025^\circ$ is achieved. The corresponding average solid angles are about $\Delta\Omega \approx 2.1 \times 10^{-8} \text{ sr}^{-1}$ per detector element. In combination with the fast measurement, these performance parameters are not achievable with conventional goniometer based systems.
- **Angular range:** The covered scattering angles are best demonstrated by the measurement results in Fig. 4.7 and are about $\theta_s \approx 10^\circ \dots 26^\circ$ and $\varphi_s \approx -30^\circ \dots 30^\circ$. This corresponds to about 1.4 % or 0.09 sr of the $2\pi \text{ sr}$ scattering hemisphere.
- **Near angular limit (NAL):** The visibility of the central plateau in the signature $hARS$ as well as the first deviations between the $PSD_{2D,iso}$ from topography and sensor data reveal a near angular limit of $\theta_s \approx 0.3^\circ$. The $hARS$ level in the signature at this angle is about 10^{-1} sr^{-1} . At $\theta_s \approx 0.5^\circ$ an $hARS$ level of only $5 \times 10^{-3} \text{ sr}^{-1}$ is achieved.

4. Experimental set-ups for angle resolved scattering measurements

These values, that define the low spatial frequency limit for roughness measurements, are even slightly better than that of the goniometer system in Fig. 4.1.

- **Spatial frequency range:** From the $\text{PSD}_{2\text{D},\text{iso}}$ a spatial frequency range of 1.5 decades from $f=0.008\text{ }\mu\text{m}^{-1}$ to $f=0.3\text{ }\mu\text{m}^{-1}$ is readable. This is below the 2 to 2.5 decades of direct topography measurement approaches, but is also less influenced by artifacts (p. 68). However, the lower frequency limit may change with the ratio between sample ARS and NAL.
- **Dynamic range:** The combined dynamic range covers more than 7.6 decades comprising 6 decades from the CMOS matrix (maximal and minimal V_{cor}) and 1.6 decades added by the adjustable power of the laser diode module. The $h\text{ARS}$ distributions of the silicon surface and the diamond turned sample cover this full dynamic range.
- **Noise floor:** The right part of the silicon wafer $h\text{ARS}$ (at $\theta_s \gtrsim 22^\circ$) reveals the highest sensitivity down to $h\text{ARS}$ of $5 \times 10^{-5} \text{ sr}^{-1}$. In this region, the dominating signature contributions from the final mirror, which cause an $h\text{ARS}$ level $8 \times 10^{-5} \text{ sr}^{-1}$, are obscured¹³. Evaluation of the PSD obtained from the signature $h\text{ARS}$ revealed a noise/NAL equivalent roughness of only 0.26 nm for an ideally reflecting sample.

Although the sensitivity and the dynamic range are below those of goniometer systems, they are sufficient for scattering measurements of a large spectrum of samples. In particular the limited sensitivity is partially compensated by the generally higher scattering levels close to the specular direction for which a very high angular resolution is available. Above all, the fast 3D measurement capabilities facilitate the development of novel analysis techniques, as will be demonstrated.

4.3.3. Uncertainty budget

The uncertainty budget development follows the "Guide to the expression of uncertainty in measurements" (GUM) that was introduced as standard to estimate the measurement uncertainties in 1998 [209,210].

The primary result of a light scattering sensor measurement is the $h\text{ARS}$ from which the PSD or the rms roughness are obtained. Following the procedure described in Sec. 4.3.2, uncertainties of the gray values, integration time, spectralon calibration value, solid angles, and laser power, as well as the sensor non-linearity provide the primary uncertainty contributions to the $h\text{ARS}$.

Moreover, any misalignments of the sample or the sensor cause misassignments of the scattering angles and change the effective solid angles in the measurement or the calibration path. These geometrical contributions were so far only investigated for goniometer based 2D-ARS measurements [13,211–213] including the uncertainty of $\Delta\theta_s$ onto the calculation of the BRDF by conventional error propagation. However, in particular the small

¹³ This obscuration is not present for scattering that emerges directly from the sample.

working distance and the reduced degrees of freedom for sample alignment¹⁴ can increase the misalignment contributions in comparison to goniometer systems. If for example the sample distance is changed by 1 mm, the solid angle of the laboratory goniometer is altered by about 0.4%, whereas it is altered by 4% in the sensor set-up.

To handle scattering angle misassignments and the complex angular relations in the determination of $\Delta\Omega_s$, the entire measurement procedure was implemented as a virtual measurement process in Matlab. Following the measurement scheme in Fig. 4.6, the model includes the measurement, the calibration, as well as the system parameter path with the corresponding misaligned set-up. This virtual measurement scheme is employed for Monte Carlo simulations, as proposed in [215] for GUM conform uncertainty evaluation, to obtain the contributions to the combined uncertainties of $hARS$ and σ .

In the uncertainty analysis the stochastic distributions of the contributing quantities have to be assigned, and categorized as type A or B uncertainties depending on whether the assignment is based on statistical analyses or other methods. The corresponding experimental results and assumptions are summarized in Tab. 4.2 (p. 37) and are described in the following¹⁵.

Laser power: The primary contributions of the laser source are attributed to the drift and noise of the emitted power between the image acquisitions. These contributions are enhanced by switching the laser off and on for the background determination. To imitate this operation regime, two experiments were performed for different laser powers: I - recording the laser power as a function of time; II - recording the laser power after a sequence in which the laser was switched off and on for random times (uniformly distributed in [0.2 s, 10 s]) until the measurement. Within these experiments, the laser beam was expanded on the CMOS matrix by a diffuser to record an averaged background corrected gray value with reduced influences from detector noise¹⁶ and speckles.

The measurements revealed an acceptable mean deviation of $<1.3\%$ for operation regime II, which is however factor four higher than in regime I. The corresponding noise value provided by the supplier for cw operation was given as $<2\%$ [198]. In addition, a significantly higher noise level was observed for low laser powers (e.g. 5.3% mode II, 1.2% mode I, at 2 mW). Therefore, laser powers below 5 mW should be avoided for measurements. The empirical distribution function obtained from the mode II experiments was approximated by a corresponding shifted gamma distribution, which was implemented as type A uncertainty in the Monte Carlo modeling.

CMOS / detector noise: The noise of the gray values per pixel (ΔGV , ΔGV_{HG}) is ob-

¹⁴ Typically the goniometer positioners can be employed for this purpose [214]. E.g.: laser based triangulation at different angles of incidence.

¹⁵ Integration time errors are included in the determined nonlinearity and in the GV noise. In the model, speckle are no origin of uncertainty, since they are inherent to the scattering of a rough surface [74]

¹⁶ The noise uncertainty is reduced by a factor of $1/\sqrt{\text{number of pixels}} \approx 1/2080$ (central limit theorem).

4. Experimental set-ups for angle resolved scattering measurements

tained by repeated measurements with and without illumination¹⁷. Within these experiments slight differences in the absolute gray value noises per pixel as functions of the incident power and the exposure time were observed. However, the standard deviations did not exceed $\Delta\text{GV}=1$. The empirical probability distributions could be approximated by a corresponding discrete binomial distribution, which was applied as uncertainty of type A in the Monte Carlo modeling.

In addition, the spatial distribution and the mean gray values of the dark signal were analyzed to include realistic background levels into the modeling. Within these investigations, the pixel-wise correction of the noise was justified. The GV mean deviation for a single pixel is less than $\Delta\text{GV}<1$ (2.1 % to 0.9 %, depending on GV), whereas, driven by the inhomogeneous background, the deviations as a function of the position on the chip can range from less than $\Delta\text{GV}\approx 1$ to 10 (3 % to 15 %, depending on t_{int}).

CMOS linearity: With the assumption that the remaining residue after the non linearity correction (Fig. 4.5, p. 29) are a result of the noise of sensor and LED sources, an additional type B uncertainty contribution with a rectangular distribution and a global uncertainty per image of 0.5 % is added to V_{cor} in the modeling.

ARS reference: The combined uncertainty of the spectralon reference was provided by the PTB as $U=0.005$ ($k=2$) for $\lambda=633\text{ nm}$. In addition, a goniometer system was applied to check the calibration curve for deviations if illuminated at 18° at 648 nm . The recognized deviations are below the measurement uncertainty of the goniometer system and primarily attributed to speckle. Therefore, the PTB calibration uncertainty of $u=U/k=\Delta h_{\text{ARS}}=0.25\%$ was applied in the modeling as type B contribution.

Sensor sample positioning: Uncertainties in the sample positioning result in different effects on the measurement results: On the one hand, the solid angles of the detector elements are changed; on the other hand, misassignments of the scattering angles are caused. The contributions themselves can be divided into two coupled sub-parts, caused by angular misalignment and deviations in the working distance¹⁸:

- **Working distance:** Without additional means, as for example alignment points, the fine adjustment of the working distance is possible with the help of a caliper, avoiding a contact to the optical surface, and by adjusting the reflex diameter on the CMOS image to its minimum. Tests revealed a typical distance $\Delta\mathcal{D}\approx 2\text{ mm}$ at which a misaligned working distance becomes visible. The same uncertainty is assumed for the spectralon, although no specular reflex is present, since sample and spectralon can be adjusted to the same distance. Therefore, a corresponding normal distribution for the working distances was included in the modeling as type B uncertainty.

¹⁷ A Schott LLS3 LED source was applied to reduce the influence of the illumination power noise and of speckle. The LED noise level was determined to less than 0.1 % for different power levels.

¹⁸ Deviations of the mechanical components provide similar contributions. These are neglected, since they should provide considerably lower uncertainties.

- **Angular alignment:** The tilt of the sample is coupled to the misaligned working distance, since a working distance induced error of the reflex position on the CMOS matrix can be partially compensated by an additional sample tilt and vice versa. Therefore, first the sample distance is misaligned in the modeling; then, the changing reflex position is compensated by an additional sample tilt. Thereafter, an additional random tilt error (Type B uncertainty) with a normal distributed polar deviation of the surface normal (mean deviation of 0.5°) and a uniformly distributed azimuthal deviation is applied. Higher polar deviations would be easily recognized by the operator, since for 0.5° the specular reflex is decentered on the matrix by about 60 pixels. For the spectralon, the working distance is not compensated, because a specular reflex is not present.

The determination of the combined measurement uncertainties for $hARS$ and σ are presented for the example of a medium rough surface with a fractal PSD ($K=5.9 \times 10^5$, $n_K=0.1$) and a relevant roughness of $\sigma=1$ nm. The actual ARS that would be measured in the misaligned geometry is calculated using the VPT and transferred to noise and background affected CMOS matrix images. The same procedure is performed for the calibration path with an incidence angle invariant ARS_{Ref} . Finally, the resulting gray values are converted into $hARS$ distributions employing the measurement scheme for the "undisturbed" sensor.

Tab. 4.2.: Contributions to the measurement uncertainties and corresponding sensitivity coefficients for $hARS$ and σ ; † mean deviation that corresponds to a uniform distribution in $[0^\circ, 180^\circ]$; * average of distributions in Fig. 4.9.

Uncertainty source	Uncertainty u	Distribution	Type	Sensitivity to $hARS^*$	Sensitivity to σ
CMOS (GV and GV_{HG})	$u_{GV}=1$	binomial	A	3.3 %	7.3×10^{-4} %
laser	$u_{P_i}=1.3$ %	shifted gamma	A	1.6 %	0.8 %
CMOS non-linearity	$u_{V_{cor}}=0.3$ %	uniform in [0.995, 1.005]	B	0.3 %	0.2 %
spectralon	$u_{ARS_{Ref}}=0.25$ %	Gaussian	B	0.25 %	0.12 %
working distance $\Delta \mathcal{D}$	$u_{\mathcal{D}}=2$ mm	Gaussian	B	4.5 %	2.2 %
angular misalignment	polar tilt $u_{\theta_i}=0.5^\circ$	Gaussian	B	1.8 %	0.4 %
	tilt azimuth $u_{\zeta_i}=52^\circ$ †	uniform in $[0^\circ, 180^\circ)$			
\boldsymbol{u}				6.5%	2.4 %

Figure 4.9 shows the corresponding spatially resolved mean deviations of the $hARS$ per pixel for the different contributing parameters. In particular the image for the angular misalignment without reflex tracking reveals an extraordinary high uncertainty in the central image region. This is caused by the moving specular reflex on the CMOS matrix.

4. Experimental set-ups for angle resolved scattering measurements

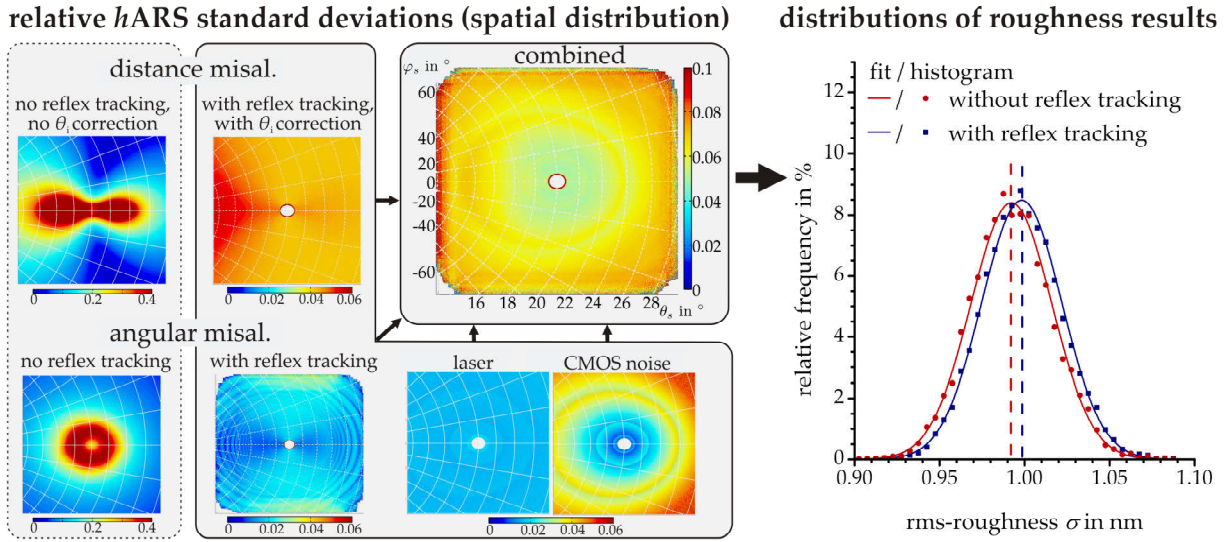


Fig. 4.9.: Left: Distributions of the $hARS$ mean deviation on the CMOS matrix for different uncertainty contributions (contributions of non linearity and spectralon have a spatially constant uncertainty distributions in a single measurement - therefore, no image); Right: Histogram of the rms roughness results with and without reflex tracking. For both histograms the same area of saturated pixels around the reflex was excluded in the calculation of σ .

To reduce this unacceptable uncertainty level, a tracking of the misaligned reflex position was implemented; the current reflex position is set to the ideal position ($\theta_s=18^\circ$, $\varphi_s=0^\circ$) by a virtual shift of the CMOS matrix in its plane.

Although the angular misassignment is only virtually compensated, a minor systematic error of σ is reduced, as visible in the histograms in Fig.4.9. This improvement can be attributed to the improved correlation between the "new" scattering angles and the ideal spatial frequencies, since both are directly associated to the distance to the specular reflex. In fact, this is a consequence of the shift invariance of the BRDF discussed in several publications [216,217].

The remaining minor underestimation of the expected value of σ in the blue histogram is less a systematic error; it is caused by the changing spatial frequency range for the misaligned sensor. Sections of the PSD that leave the angular range of the sensor are primarily replaced by sections with lower PSD values due to the monotonically decreasing model PSD¹⁹.

From the results illustrated in Fig.4.9 and in Tab.4.2, it is obvious that the alignment uncertainties, in particular those of the sample distance, provide the highest contributions to the uncertainties of $hARS$, PSD, and rms roughness. Therefore, in an implementation of the sensor for in-line measurements the set-up should have means such as limit stops or distance sensors to reduce these contributions or to include a determined deviation in the calculation of the $hARS$, respectively.

The rings which are visible in the mean deviation of the ARS correspond to the overlapping regions of images with different exposure times in the HDR image series. They are

¹⁹ If the determined σ is compared to the σ that corresponds to the spatial frequencies of the misaligned system this minor deviation vanishes.

primarily influenced by the sensor noise, but also by fluctuations of the laser power. The latter contributions to measurement and calibration would be reducible with a mechanical shutter, which is however a moving component.

Kolmogorov-Smirnov tests for normal distribution with a significance level of 0.95 were positive for the histograms of the roughness, whereas they were only just rejected for single $hARS$ values²⁰. Therefore, the coverage factor for the 0.95 significance level of the roughness can be set to $k=2$, and the combined measurement uncertainty is calculated to only $U_\sigma=2u_\sigma=0.048$ nm (4.8 %). Assuming $k=2$ also for the $hARS$, the average combined uncertainty would be about 13 % per $hARS$ pixel, which is comparable to goniometer systems [5,11,149,212].

4.3.4. Reliability of roughness measurement results

The characterization of surface-related scattering phenomena, such as scattering from interface roughness and surface defects, will be the primary application area of the scattering sensor. Therefore, a revision of the validity of basic structure-scattering-relations in the context of the specific sensor configuration is presented to improve the understanding for the sensor application. This includes the determination of the upper roughness limit that is measurable with the VPT and the discussion of the VPT inherent far-field properties. The latter is often taken for granted in conventional light scattering experiments. However, results of virtual experiments with the BKT shall demonstrate the risk of potential errors which are in particular relevant for compact sensor systems.

Far-field properties

The application of the VPT requires the scattered power to be recorded in the far-field of the sample surface [83,103,132,218,219]. For example in [103], the scattered (far-)field, that emerges from a virtual roughness induced interface current density, is calculated by a Fourier transform of the current density. On the other hand, the detector matrix of the scattering sensor is located in a distance of only 52 mm, which is rather close to the sample surface, and violates the conventional Fraunhofer far-field requirements. Nevertheless, the excellent correlation of the PSD functions obtained from the $hARS$ and topographic PSD data was already demonstrated in the previous section (Fig. 4.8).

The Fraunhofer criteria $r\lambda/d^2=52\text{ mm }660\text{ nm}/(2\text{ mm})^2=8.6\times10^{-3}\not\gg1$, with r the detector distance and d the spot diameter, is violated for the scattering sensor. On the other hand, the scattering problem is not exactly identical to the diffraction from a plane screen; the relevant phase fluctuations are induced by the vertical roughness components and not by the lateral dimension of the illuminated spot, in particular if higher spatial frequencies are considered. Therefore, d should be replaced by the highest expectable vertical dimension

²⁰ This discrepancy illustrates the central limit theorem. The roughness, which was positively tested for normal distribution, is calculated from the integral (sum) of non-normally distributed $hARS$ values.

4. Experimental set-ups for angle resolved scattering measurements

or by the highest spatial wavelength. For both values 10 μm is a reasonable suggestion; hence, the Fraunhofer criteria would be satisfied ($343 > 1$).

In [161] the far-field concern was mentioned as well: Although the presented detector yoke with a sweep radius of 164 mm and a wavelength of 633 nm should operate in the Fresnel region, the measured scattering patterns were not distinguishable from Fraunhofer scattering distributions [161]. However, since the detectors were positioned on the circumference of a yoke and not on a plane, which would intensify the paraxial limitation of the Fraunhofer approximation, the disturbing phase variations can be neglected if the surface is illuminated by a spherical wave [94,216,220].

The scattering sensor, just like most goniometer systems, comprise a lens or a mirror in the beam preparations system to set the focus of the incident beam on the detector sweep radius. This optical component ensures the spherical wave illumination and implicates the far-field properties, since it has a similar function as the lens in a 2f-arrangement that causes an optical Fourier transform. This optical Fourier transform is also present if the object is located in between the focusing element and the focal spot [221, pp106].

On the other hand, the detector of the scattering sensor is plane, even closer to the sample than the yoke in [161], and is, moreover, not tangential to the scattering sphere. For further studies into the far-field properties, in particular into how the measurement results are influenced by the specific geometrical properties of the scattering sensor, *hARS* distributions that would be obtained with different detector configurations (Fig. 4.10 c) were modeled employing the BKT. Besides the specifics mentioned, the influence of the focused illumination beam is additionally investigated.

Corresponding results for a sinusoidal grating with an additional random roughness are summarized in Fig. 4.10 a) and b). To include the focusing element, the incident plane wave in Eq. 3.4 was replaced by a spherical wave with a curvature \vec{r}_f in the direction of the focus:

$$E \propto \frac{e^{i(-r_f k - \omega t)}}{r_f} , \quad \left(\frac{\partial E}{\partial n} \right)_{\text{A}} = (1-F) E \left(ik - \frac{1}{r_f} \right) \cos \angle(\vec{n}, \vec{r}_f) . \quad (4.4)$$

The diagrams reveal the convolution of the scattering distribution, represented by the diffraction peaks and the noisy bottom level, with the diffraction pattern of the illumination spot. This effect becomes in particular disturbing with decreasing detector distance ($r_f < 1000$ mm, a), but is significantly reducible if the illumination beam is focused on the detector (b). Nonetheless, higher diffraction orders reveal defocusing effects if the detector distance is reduced (inset, Fig. 4.10 b). These "aberrations of the diffracted wave field" [216] are only slightly increased if the detecting elements are distributed over an oblique plane (scattering sensor) and not on a sphere with a radius of 52 mm.

Although the diffraction of the illumination beam and the aberrations should influence the scattering from the random roughness as well, these effects are not evident in the corresponding parts of the ARS. They are obscured by the random phase effects that

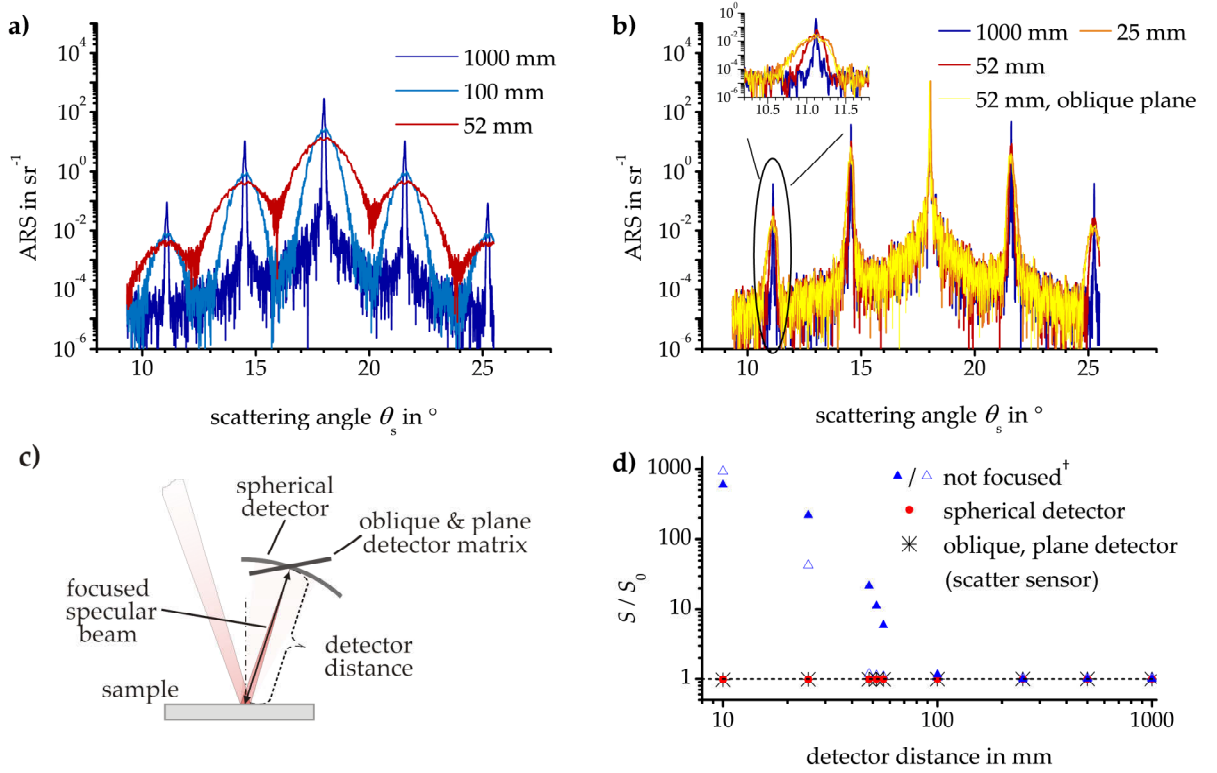


Fig. 4.10.: Far-field properties analyzed for a superposition of a smooth sinusoidal grating (amplitude=20 nm, $f=0.09 \mu\text{m}^{-1}$) and a random rough surface ($K=5000$, $n_K=1.3$). The spot diameter on the sample is 2.3 mm ($2\omega_0$). a) ARS as a function of detector radius without focusing element. b) ARS as a function of detector radius with focusing element. In addition a curve for the oblique, plane (matrix) detector is illustrated. c) Scheme to emphasize the different detector geometries. d) Influence of the focusing element and the detector form on the measured S values, which are proportional to σ^2 , for a purely random rough surface ($K=5000$, $n_K=1.3$). S_0 is the value obtained with a spherical detector (sweep radius: 1000 mm) and with a focusing element. [†]) lower integration limits of $\theta_s=1.5^\circ$ or 3° for filled or open triangles, respectively.

cause the speckle pattern. This is even better emphasized by diagram a); though no focusing element is applied, the ARS bottom level for the 100 mm sweep radius is identical to 1000 mm sweep radius. Only the convolution of the peaks obscures the scattering from random roughness. Consequently, light scattering based roughness measurements of pure random rough surfaces, which have no edges in the PSD, are almost unaffected by far-field concerns, as long as the diffraction pattern of the specularly reflected beam is excluded from the evaluation or a focusing element is applied.

This also holds for the integrated scattering of a rough surface - pure roughness without sinusoidal grating - as summarized in diagram d). The determined S values, which represent the roughness (Eq. 3.3), remain constant for the different detector configurations. The deviations for the set-up without a focusing element are only induced if the increasing width of the specular peak contributes to the integration of S . This is demonstrated by a comparison of S for two different low angle integration limits (1.5° and 3° , Fig. 4.10 d).

Roughness measurement on smooth (and medium rough) surfaces

There are several statements on the validity of the first order VPT for increasing roughness levels within the literature. In the following paragraphs, these statements are summarized, reviewed in the context of the scattering sensor, and compared to modeling results obtained with the BKT. This review is necessary, since it is not always clear whether bandwidth limited or intrinsic (possible for the ABC-model) roughness values are given.

Furthermore, the modeling enables the application range of the VPT in the context of the scattering sensor to be quantified with the correct bandwidth. In particular, the non-approximated exponential version of Eq. 3.3 is not valid if the spatial frequency range of σ does not cover the entire scattering relevant frequency range [222].

The most simple and general statement is the requirement for any single roughness component within the roughness spectrum to be much smaller than the wavelength of light [223]. The limit for the term "much smaller" and the question for the relevant spatial frequency range are left open. Church, Elson, and others state in a number of papers that $0.01 = (\mathbf{a}^2\pi/\lambda)^2 \ll 1$ [44,74,82,85]²¹, with \mathbf{a} the amplitude of a sinusoidal grating. Thus, the limiting amplitude would be about 11 nm ($\sigma=7.8$ nm [62]) for the scattering sensor ($\lambda=660$ nm). In [76] a slightly different relation named as Rayleigh-Strehl parameter is given for the case of a smooth surface version of the BKT: $((4\pi/\lambda) \sigma \cos \theta_i)^2 \ll 1$. With this relation the detectable roughness would be only 5.5 nm.

Within some Russian light scattering papers, the limits are discussed for the application of the VPT on X-ray scattering measurements at grazing angles of incidence [72,96]. The resulting roughness limits as functions of the incidence angle and the polar scattering angle are $k\sigma \cos \theta_i < 0.3$ and $k\sigma \cos \theta_s < 0.3$, respectively. For the scattering sensor, with θ_i and θ_s close together, this corresponds to approximately $\sigma \lesssim 30...36$ nm. Independently from scattering or incidence angles, $\sigma \lesssim \lambda/20 \approx 32.5$ nm should hold [96]. An interesting consequence of the previous relations is the possibility to increase the maximal detectable roughness value to more than 100 nm by increasing the angle of incidence to $\theta_i \approx 80^\circ$ and by the evaluation of scattering angles close to the specular reflex²².

In [224] two different relations are stated: $\sigma \lesssim \lambda/20 \approx 30$ nm for angle resolved scattering analysis; $\sigma \lesssim 0.3\lambda \approx 200$ nm for TS-based roughness determination [224]. The latter is, however, an result of the increased validity range of the exponential part of Eq. 3.3 compared to the VPT. On the other hand, in [28,192] PSDs from topography and scattering data of a surface with $\sigma=100$ nm reveal an acceptable correlation, although slight discrepancies become evident.

For the stated roughness limits, it is not always clear whether the given roughnesses are bandwidth limited or related to the scattering in the complete hemisphere. Moreover, the results are not related to other stochastic properties such as the form of the corre-

²¹ "«»" is interpreted in the following as 0.01; The sensor wavelength 660 nm is used as λ .

²² The required θ_i or θ_s are not accessible with a compact sensor set-up; the typical geometry of commercial CMOS matrices with the sensitive area surrounded by a circuit board prevents it.

sponding PSD functions. To increase the information on these limitations, in particular, for the scattering sensor specifics, modeling results of the BKT and the VPT of ideally reflecting surfaces ($F=-1$, $Q=1$) were compared. The required random surfaces with varying roughnesses and different PSD slopes were generated by utilizing the procedure introduced in Sec. 3.2.1 (p. 14) for fractal PSD model functions (Eq. 3.10 in Sec. 3.2.1).

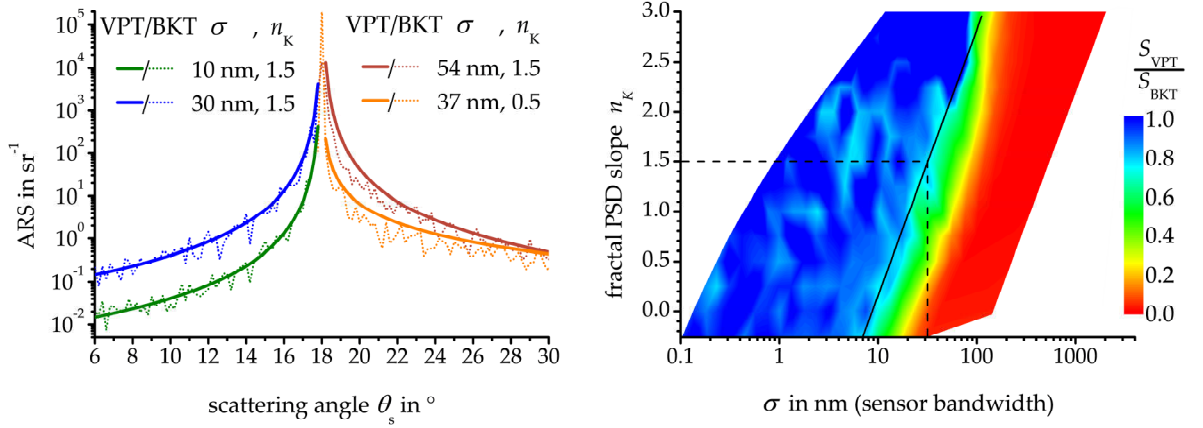


Fig. 4.11.: The increasing roughness results in deviations of the VPT and the BKT. Left: ARS curves illustrate the deviations as a function of scattering angles. Right: Deviations of the integrated scattering S , as a function of the surface roughness and the PSD slope, demonstrate the limits of the VPT for roughness measurements with the scattering sensor. Black line: threshold of $S_{\text{VPT}}/S_{\text{BKT}} > 0.8$, corresponds to 10% deviation of the rms roughness.

The modeling results, summarized in the left part of Fig. 4.11, reveal a good correlation between the VPT and the BKT for low roughnesses (blue/green curves). For higher roughness values, power is redistributed from the close to specular region presumably to higher diffraction orders, as demonstrated by the red and orange curves. To quantify these deviations, the right part of the figure illustrates the ratio of partially integrated scattering determined from the BKT and the VPT modeling results as a function of the roughness (sensor relevant frequency range) and the PSD slope n_K .

The results demonstrate, that the detectable roughness threshold is not determinable as single number, since it changes considerably with the PSD slope. The capability to measure high roughness values is increasing with n_K up to $\sigma \approx 70$ nm sensor relevant roughness for $n_K=2.5$, which corresponds to 71 nm relevant roughness at 660 nm. For this n_K the contributions (or amplitudes) of higher spatial frequencies to the roughness are almost negligible. However, personal experiences revealed that the highest values for n_K do seldom exceed $n_K \approx 1.5$. Therefore, the highest accessible roughness values are in the order of $\sigma=30$ nm (32 nm relevant at 660 nm). For low n_K values, a dramatic decrease of the accessible roughness, down to only $\sigma=8$ nm (18 nm relevant at 660 nm) is observed. This is caused by the increasing amplitude of higher spatial frequency components which cause scattering into higher diffraction orders, compared to those at lower frequencies.

4.3.5. Summary

A number of semiconductor matrix detector based light scattering measurement concepts were developed for several applications to overcome the time-consuming scanning procedures of goniometer based systems. However, a lack of highly sensitive and compact sensor systems which are applicable to 3D near angular scattering measurements of optical components was recognized, that led to the development of the novel light scattering sensor.

Although the basic concept of this sensor comprises a commercial CMOS sensor matrix, an elaborated beam preparation system as well as comprehensive measurement and calibration routines enable the measurement of calibrated 3D-*h*ARS distributions with a dynamic range of 7.6 decades down to ARS levels below $5 \times 10^{-5} \text{ sr}^{-1}$.

The PSD functions obtained from such measurements extend over a spatial frequency range of one and a half decades and have a signature equivalent roughness level of as low as $\sigma=0.26 \text{ nm}$. Combined uncertainties ($k=2$) of only 5% for rms roughness values and about 13% for *h*ARS values were determined using Monte-Carlo modeling based uncertainty analysis. This latter uncertainty is in the order of those of conventional goniometer systems [5,11,149,212].

In addition to the evaluation of the uncertainty budget, the validity conditions of the VPT and the far-field properties, required for the application of the VPT, were analyzed for the specific scattering sensor geometry. The corresponding BKT modeling results revealed an upper roughness limit of about 30 nm, which, however, can be influenced by the PSD slope. On the other hand, the modeling revealed negligible influences of the compact sensor arrangement on the scattering and roughness measurement results, since the far field requirements are ensured by the final imaging element in the beam preparation system.

5. Techniques applied for direct roughness and defect assessment

The techniques summarized in this chapter were applied for the verification of the results obtained with the light scattering sensor by direct, light scattering independent techniques and for the development of new analysis approaches. Thorough modeling of light scattering requires topography data obtained with techniques that cover the light scattering relevant spatial frequency range and are sensitive for roughness levels in the sub-nanometer regime. In particular, the first requirement is achieved by the combination of results from white light interferometry and atomic force microscopy. In addition, typical assessment approaches for surface defects are discussed for which an alternative application scenario of the scattering sensor is developed in Sec. 6.4.

5.1. Topography measurement techniques

White light interferometry

White light interferometry (WLI), which combines interferometry and optical microscopy, exploits the short coherence length of broadband (visible) light. The corresponding interference patterns result from the superposition of magnified images of the surface and a reference plane. Therefore, reference planes as well as beam splitting elements are included in the microscope objectives. By scanning along the macroscopic surface normal, varying interference patterns are obtained, which are analyzed for intensity and phase to calculate the surface topographies [225].

The WLI measurements in this thesis were performed with a ZYGO New View 7300 WLI applying a 10× Mirau and a 50× Mirau objective. The corresponding measurement parameters, including the spatial frequency resolution provided by the supplier, are summarized in Tab. 5.1. However, the lateral as well as the vertical resolution are influenced by the profile of the sample as discussed in [226] and by the author of this thesis in [227]. In addition, objectives can exhibit a low pass function which flattens the amplitudes of high spatial frequency roughness components. The uncertainty of the determined rms roughness values excluding these effects is in the order of 10 % [228].

Atomic force microscopy





Atomic force microscopy (AFM) exploits the changing forces if a nanometer-sized probe tip on a cantilever is scanned over a surface. By analyzing the changing oscillation fre-

5. Techniques applied for direct roughness and defect assessment

quency of the cantilever as a function of the tip position, a surface profile is extracted [229,230].

Tab. 5.1.: Scan areas applied for topography measurements and corresponding nominal resolutions.

[†] the minimal roughness is limited to $\sigma \approx 0.04$ nm by instrument noise.

	objective	area in μm^2	Δz in nm	Δx in μm	spatial frequency f in μm^{-1}
WLI	10×	698×523	<0.1	1.09	
	50×	140×105		0.22	
AFM		50×50	<0.02 [†]	0.10	
		10×10		0.02	

The measurements presented in this thesis have been obtained using a Dimension 3100 Atomic Force Microscope (Bruker, Tapping ModeTM) with single crystalline silicon probes of $r=10$ nm nominal tip radius. From the tip radius the lower lateral resolution limit is determined by: $f_{\max}=1/2\pi\sqrt{ar}$ [75,135], with a the amplitude of a sinus profile. However, even with an amplitude of 100 nm, f_{\max} is in the order $5\mu\text{m}^{-1}$ and, therefore, beyond the light scattering relevant frequency range for visible light.

Inaccuracies at low spatial frequencies can be induced by deviations of the piezo system which moves the probe tip. The resulting effect, known as "scanner bow" [63], is in particular relevant for large scan areas.

The vertical resolution is limited by instrument noise to rms roughness values as low as $\sigma \approx 0.04$ nm; uncertainties for the corresponding PSD functions are below 15 % [135]. A detailed uncertainty analysis can be found in [231].

5.2. Surface defect classification

The identification and classification of surface defects such as scratches, digs, pits and humps is, besides surface roughness, form, and spectral properties, one of the most critical issues for the quality assessment in the fabrication of optical surfaces. The current standards for defect assessment are defined in the ANSI/OEOSC OP01.002 [114], which is based on the scratch/dig specification in the MIL-PRF-13830B [113], or in the ISO 14997 [8] with defect classes defined in the ISO 10110-7 [112].

Following the ISO 10110-7, the class of a flaw, regardless whether it is a scratch or dig, is categorized in classes based on the square root of the defect area in millimeters. Regarding the OP01.002, the classification of digs is very similar, besides that the defect class is given by the dig diameter or by the average of the maximal and minor defect axes in $1/100$ mm. On the other hand, scratches are classified by comparing their visual impressions to the impressions of scratches on reference charts.

This kind of empirical light scattering evaluation is the most common way for a first defect assessment in the daily routine of optical fabrication [8]. Trained persons compare

the visual impressions of flaws to artificial flaws of known classes on reference charts under defined illumination and observation conditions [113]. For scratches this is even the preferred MIL/OP conform procedure [7], since the scratch standard and its secondary standards are only determined by the visual appearance of the reference scratches, but not by geometrical properties [2]. Regarding ISO, the reference chart should consist of deposited chromium areas on glass substrates, whereas the original MIL standard requires flaws that reveal the same impressions as the primary reference standard and look like etched or ground [Drawing C7641866 in 113].

The subjective portions of the conventional classification procedures were recognized and criticized years ago [2,6,10]. Consequently, alternative objective characterization methods were proposed, that were partially included into the current versions of the standards. For example with the image comparator microscope [10], which is one quantitative method described in the ISO 14997 [8], the power removed by defect light scattering from the specular direction is measured to identify the defect classes. By this method, which should be applied to scratches and digs whose dimensions are below $10\text{ }\mu\text{m}$ [8], the defects are characterized by visibility. With the development of digital cameras and industrial vision techniques in recent years, several approaches were described that (automatically) evaluate surface images recorded under dark field conditions [6,9,232–236]. However, these systems are still not yet common in daily practice.

Most microscope based approaches can be exploited to obtain the defect area as well. In particular Nomarski and Darkfield microscopy should be mentioned [61,156]. By white light interferometry, even the entire defect geometry is determinable; therefore, it was utilized for the basic investigation within this thesis. However, the application of microscopes is described in ISO 14997 as not suitable; due to the small field of view, the system can only assist the defect classification in quality assessment.

Within the semiconductor industry there is a similar task as the defect assessment; the detection of nano-flaws, in particular nano-particles and pits in silicon wafer surfaces is of great interest [237,238]. For this purpose several highly sensitive light scattering based systems exist that exploit the characteristic scattering distributions of (nano-)particles on smooth surfaces [19,237–239]. Within a sub class of these non-compact, complex systems (several) single or integrating detectors record the scattering of the surface that is scanned by a highly focused (laser) beam [39,40,237]. In particular, these applications give promising hints for possible application scenarios of the light scattering sensor.

6. Light scattering properties of optical surfaces and thin films

The light scattering sensor developed opens up novel analysis scenarios for the quality assessment of optical surfaces. This chapter demonstrates both: the variety of characterization tasks, whose accomplishment is enabled through the sensor, as well as the requirement for a comprehensive understanding of the corresponding physical relations needed to interpret the measurement results and to derive tailored analysis procedures. Therefore, the investigation of the following properties of optical surfaces will be discussed:

- Nanostructure analysis and modeling of anisotropic surfaces fabricated by single-point diamond turning and magnetorheological finishing (Sec. 6.1),
- roughness and anisotropy analysis of titanium thin films (Sec. 6.2),
- light scattering and roughness evolution analysis of a notch-filter system (Sec. 6.3), as well as
- assessment of defects on optical surfaces (Sec. 6.4).

6.1. Anisotropic light scattering distributions and surface structures

A number of optical surfaces exhibit corrugated nano-structures [17,21,34,81,193,240,241] that imply anisotropic roughness properties. In the spatial frequency domain, this corresponds to non-rotationally symmetric 3D-PSD functions and, hence, also to non-rotationally symmetric 3D-ARS distributions. In particular the characterization of anisotropic surfaces demonstrates that measurements along single directions, as in stylus profilometry or in-plane ARS measurements, can cause misleading roughness information [11].

Surface anisotropy is either an intrinsic material property [242], which may be exposed in the fabrication process, or is a desired but primarily undesired result of the fabrication process. Therefore, combined roughness and isotropy analyses can provide information on the fabrication process which can be exploited for the evaluation and improvement of the process. This will be demonstrated for MagnetoRheological Finishing (MRF) and Single-Point Diamond Turning (SPDT). Both technologies are common processes in state of the art optical surface fabrication which induce highly anisotropic surface structures. On the other hand, even commercially available - presumably conventionally polished - surfaces are prone to have anisotropic surface structures, as was observed in the context of the light scattering sensor development for RG1000 and float glass surfaces, cylindrical lenses, or coated metallic mirrors.

For a comprehensive performance modeling of optical systems, for example of light scattering sensitive high contrast optics, the complete 3D-light scattering information, including the anisotropy properties, should be considered [175]. Therefore, quantitative measurement and analysis techniques are required that are applicable in the quality assessment.

The light scattering and roughness evaluation of SPDT aluminum surfaces is presented to demonstrate approaches for the characterization and quantification of isotropy properties. Later on, the procedures derived are applied for the comparison of the diamond turned surfaces and an anisotropically polished glass surface as well as for the optimization of MRF processes.

6.1.1. Approaches to measure and quantify structure properties of anisotropic surfaces

Figure 6.1 (next page) summarizes surface topography images of WLI and AFM measurements, the h ARS, as well as the corresponding 3D-PSD functions of an aluminum surface fabricated by SPDT. Additional sketches in Fig. 6.1 reveal the relations of the respective measurement areas.

In the turning process, a diamond-tipped tool bit of radius $R_T=450\text{ }\mu\text{m}$ was moved in a spiral with a feed period $\vartheta=10\text{ }\mu\text{m}$ over a preshaped surface¹ and removed material to achieve the final surface form (and finish). Therefore, the dominating surface structure corresponds to a smooth, cusp shaped grating of period ϑ for which the WLI revealed peak heights of 5 nm to 15 nm (Fig. 6.1). This amplitude was generated by the shape and the overlapping of the tool bit from period to period. Within and parallel to the turning marks, the periodic repetition of edges in the tool footprint caused an additional corrugated structure, which is in particular visible in the AFM topography data (Fig. 6.1).

Further roughness components were induced by vibrations of the tool bit that generated chatter marks in the grooves and disturbances of the periodic structure [149,243]. Finally, intrinsic material properties such as the grain structure [61,81,244] and corrosion patches [63], represented by the red spots in the WLI topography data, cause an isotropic background roughness component.

Advantages of scattering sensor based roughness and isotropy analysis

The h ARS as well as the 3D-PSD functions in Fig. 6.1 enable the roughness components within specific spatial frequency bands to be analyzed in more detail. In particular within the spatial frequency range covered by the h ARS and the corresponding PSD the three roughness components are very well distinguishable:

- The vertical diffraction structure represents the feed marks, their periodicity, the structure within the feed marks, as well as deviations of the periodicity and the

¹ The SPDT samples presented in this section were provided by Ralf Steinkopf, Fraunhofer IOF.

6. Light scattering properties of optical surfaces and thin films

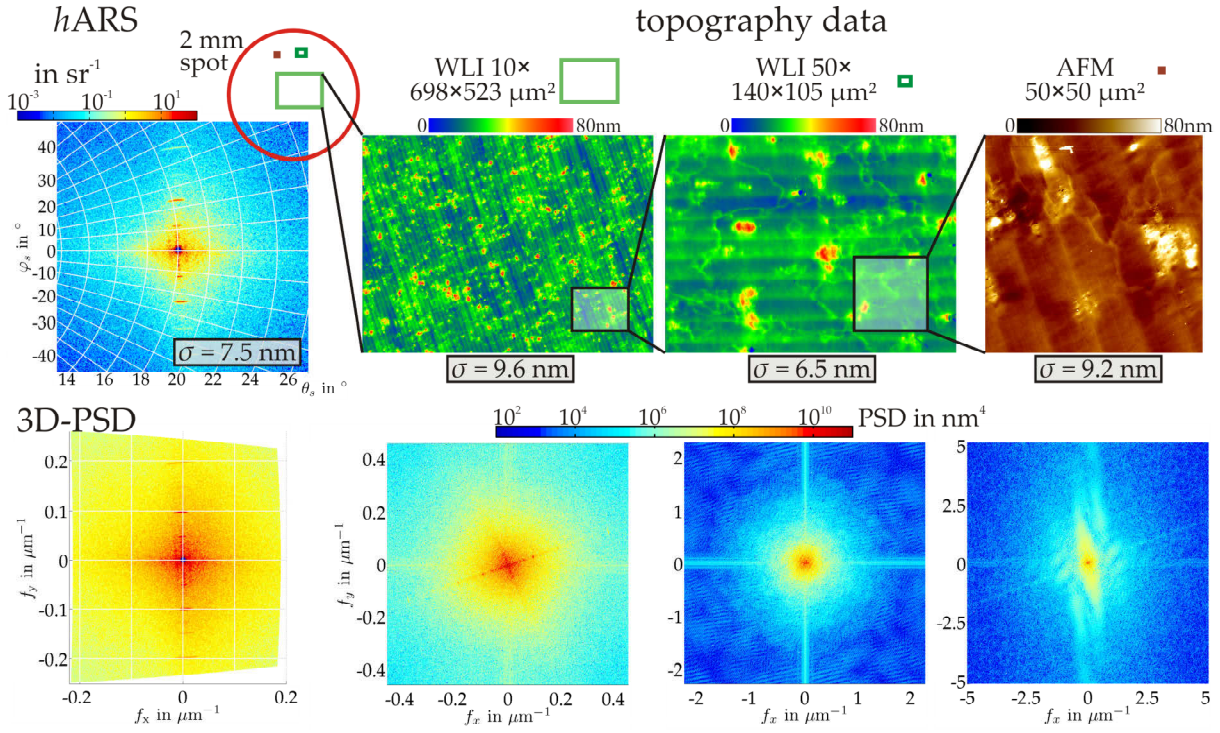


Fig. 6.1.: Upper row, from left to right: Comparison of roughness information obtained from *hARS*, WLI (10×, 50× objective), and AFM (50×50 μm^2 scan); the measurement areas are additionally compared in the uppermost row. The lower row illustrates the derived 3D-PSD functions.

amplitude as discussed in detail in [149] and [62, Ch.4.3]. In a distance of about 2° from the specularly reflected beam, diffraction peaks are visible, which correspond to the feed mark frequency of $f=0.1 \mu\text{m}^{-1}$ (Eq. 3.2). It should be mentioned, that the observable number of diffraction peaks are no higher diffraction orders. The peaks correspond to higher or additional Fourier orders/components of the non-sinusoidal grating structure and are, therefore, visible in the PSD functions from topography data as well (WLI 10×objective, 3D-PSD and PSD_{2D} in Figs. 6.1 and 6.2).

- The increased scattering, almost perpendicular to the direction of the diffraction peaks, is caused by the corrugated structure of the jitter within the feed marks. The angle between this distinct direction is about 94° and corresponds to the angle between the turning edge and the feed direction. This angle is only slightly visible in the jitter marks within the topography data of the AFM scan. In contrast to the plane of diffraction, no distinct frequency is visible within the jitter.
- The average roughness and the remaining areas of the 3D-PSD functions are dominated by the isotropic background roughness and the granular structure. Hence, these roughness component are responsible for the average level and the average shape of the $\text{PSD}_{2D,\text{iso}}$ functions (Fig 6.2).

Within this evaluation, the suitability of light scattering measurements is notable. Induced by the averaging over the illumination spot, PSD functions from *hARS* distributions are less influenced by local inhomogeneities. For example the grain visible in the AFM topography data is the reason for the anomalous wobbling like structure in the

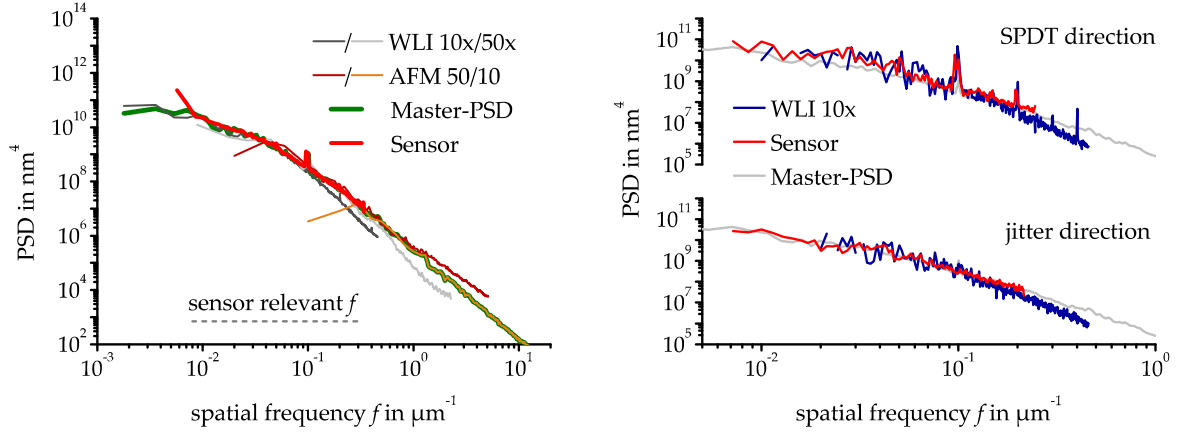


Fig. 6.2.: $\text{PSD}_{2\text{D},\text{iso}}$ and directional $\text{PSD}_{2\text{D}}$ functions (left/right) obtained from the PSD data in Fig. 6.1.

corresponding AFM 3D-PSD. Moreover, the resulting PSD functions are not prone to trending/detrending and edge discontinuity artifacts [245], that are possible sources of the differently pronounced crosses² within the topography based PSD functions. Further artifacts of topography based PSD functions are for instance aliasing or the low-pass filter induced by the transfer function of the WLI objective, for which impressive examples are given in Sec. 6.2

In Fig. 6.1 the determined roughness values are additionally given. Striking are deviations of the σ values that primarily result from the different spatial frequency ranges covered. Nevertheless, in the overlapping regions of the corresponding $\text{PSD}_{2\text{D},\text{iso}}$ functions (Fig. 6.2) an excellent correlation is identifiable. Possible reason for remaining deviations are local stochastic surface deviations, measurement noise, and especially the artifacts mentioned. It is therefore mandatory to identify these artifacts and to exclude them in the calculation of Master-PSD functions [63,228].

The $\text{PSD}_{2\text{D},\text{iso}}$ function obtained from the $h\text{ARS}$ fits the transition between the different topographically determined PSDs very well. In addition, the $h\text{ARS}$ based PSD functions are less affected by stochastic noise or local stochastic surface deviations and have a higher data density. This is achieved by dividing the f -range of the sensor into intervals with bandwidths of $\Delta f \approx 6 \times 10^{-4} \mu\text{m}^{-1}$. Although these intervals meet the average frequency interval of adjacent CMOS elements, each class contains about 500 PSD values.

Methodology for directional roughness analysis

The example of the SPDT surface demonstrates that rms roughness values as well as $\text{PSD}_{2\text{D},\text{iso}}$ functions only provide reduced information, which is insufficient for a comprehensive surface characterization of anisotropic surfaces. It is, in particular, not possible to distinguish the different roughness components relevant for different directions on the surface. Therefore, the development of a methodology for anisotropy characterization is described in the following paragraphs.

² The crosses occur although the topography data was corrected for tilts with the WLI/AFM software.

Direct, topography based anisotropy analyses would be viable by two approaches: Measurement of 2D surface profiles in specific directions or, more generally, the calculation of directional roughness values or PSD functions by evaluating cuts or projected averages of 3D surface profiles. Both methods are not discussed in detail, since recording single surface profiles is not practicable for a fast assessment and the evaluation of cuts and projected averages requires special care for numerical artifacts³.

The most natural way to derive easy to handle anisotropy information should be the direct evaluation of 3D-PSD functions. In the same way as a measured $\text{PSD}_{2\text{D},\text{iso}}$ function is bandwidth limited with respect to f , the 3D-PSD in an azimuthal spatial frequency interval $\Delta\varphi_f$ represents the roughness components of a specific direction.

On the other hand, the topographically determined PSD functions exhibit the mentioned stochastic noise, artifacts, and have a reduced data density, which in particular limits the reliability in narrow frequency intervals or at low spatial frequencies⁴. At this point the advantages of (*h*)ARS based roughness measurements become evident:

- The spatial frequency range covered is defined by the grating equations and can be adjusted through the wavelength and the scattering geometry;
- the spatial frequency resolution is directly given by the discretization of the scattering angles, which corresponds to the high density of the CMOS matrix elements;
- the sampled surface area, relevant for the scattering inherent averaging, is determined by the illumination-spot diameter, which exceeds those of WLI or AFM (Fig. 6.2)

Hence, in contrast to topographically determined PSDs, the spatial frequency resolution is decoupled from the surface area averaging so that the stochastic reliability can be easily increased.

For example in [247], anisotropy analysis on the base of a direct evaluation of the ARS at normal incidence was presented. For $\theta_i=0$ the azimuthal scattering angle φ_s corresponds directly to the polar spatial frequency φ_f , since the grating equations are no longer coupled ($\theta_s \leftrightarrow f, \varphi_s \leftrightarrow \varphi_f$). However, unpolarized illumination [247] and detection is additionally necessary to avoid an artificial optical anisotropy in the ARS that is induced by the optical factor Q . The ARS based anisotropy analysis presented in [248] is performed at normal incidence as well, but the sample was rotated along its normal, whereas the azimuthal scattering angle was fixed. In this configuration (within the VPT) any influence of the polarization is avoided. However, both approaches were presented for time consuming goniometer based ARS measurements.

For measurements with the scattering sensor, the non-polarized detection is fulfilled; the anti-reflective coating reduces the sensitivity differences for polarization to only about

³ Projected averages of a 3D surface profile (Fourier slice theorem [246]) sampled on a rectangular grid can result in artificial roughness components at high spatial frequencies. On the other hand, a numerical Abel transform is required to calculate a $\text{PSD}_{2\text{D}}$ of a non-averaged cut [62,82,125].

⁴ Increasing the scanning area could avoid this limitation. However, since the number of data points is often kept constant, the lateral resolution is reduced and high spatial frequencies are lost.

1%⁵. Hence, the singularity in the optical factor ($Q=0$) at specific scattering angles for polarization sensitive detection vanishes. The PSD functions obtained from the h ARS are corrected for the remaining influences of polarization by applying the correct Q for s-polarized illumination. Consequently, elaborated anisotropy analyses based on 3D-PSD functions become possible and directional roughness values σ_i can be determined employing the following universal relations of roughness and PSD:

$$\sigma = \sqrt{\int_{\varphi_f} \int_f \text{PSD} f df d\varphi_f} = \sqrt{\sum_i \int_{\Delta\varphi_{f,i}} \int_f \text{PSD} f df d\varphi_f} = \sqrt{\sum_i \sigma_i^2} \quad (6.1)$$

These equations lead to conclusions for normalization, which provide a basis to analyze or compare anisotropic properties and to derive tailored anisotropy parameters:

- $\sigma \neq \sum_i \sigma_i$ - The σ_i represent the bandwidth limited ($\Delta f, \Delta\varphi_f$) contributions along specific directions to the isotropic rms roughness σ , but do not add up directly to σ .
- $\hat{\sigma}_i = \sqrt{(\sigma_i^2 / \Delta\varphi_f) 2\pi}$ - represents a normalized directional roughness value, comparable to the rms roughness of an isotropic surface with the same σ . These $\hat{\sigma}_i$, bandwidth limited in f and φ_f , can be compared independently of the applied azimuthal spatial frequency bandwidth $\Delta\varphi_f$.
- $\frac{1}{\Delta\varphi_f} \int_{\Delta\varphi_f} \text{PSD} d\varphi_f$ - gives an averaged PSD_{2D} that corresponds to the $\text{PSD}_{2D,iso}$ of an isotropic surface with that PSD. Normalization to $1/2\pi$ instead of $1/\Delta\varphi_f$ would result in the contributions to the $\text{PSD}_{2D,iso}$ in the $\Delta\varphi_f$ interval.

The suitability of the light scattering sensor for this evaluation is demonstrated by exemplary directional PSD_{2D} functions of the SPDT surface, obtained from topography and h ARS data along the turning and the jitter directions (Fig. 6.2, right). Because of the higher averaging (about factor 4 more sampling points in $\Delta\varphi_f$) and the higher resolution, the resulting PSD_{2D} functions, obtained for identical Δf and $\Delta\varphi_f$ intervals, reveal less noise and no missing data points. In addition the mathematical effort is reduced, since the PSD_{2D} is directly sampled from the h ARS and a Fourier transform can be omitted.

Application to single-point diamond turned surfaces

The h ARS of three diamond turned aluminum surfaces together with the applied fabrication parameters are illustrated in Fig. 6.3 (sample III is the same as in Fig. 6.1). The corresponding directional roughness distributions of $\hat{\sigma}_i$ (Fig. 6.4, left) were determined with a $\Delta\varphi_f$ of 4° and a sampling of 0.5° in φ_f . These curves reveal a significant reduction of the SPDT roughness component with decreasing feed period, but almost identical levels for the contributions from jitter and other isotropic components.

Following [250] and [62, p.27], the roughness of a 2D profile consisting of grooves, whose profiles are circle sections, is $\sigma_{\text{SPDT}} = 0.3z_0$, with z_0 the cusp height of adjacent

⁵ The reflectance spectrum of the AR-coated CMOS matrix, provided by the supplier, was transferred to the applied incidence angle and analyzed by utilizing the thin film software IMD [249].

6. Light scattering properties of optical surfaces and thin films

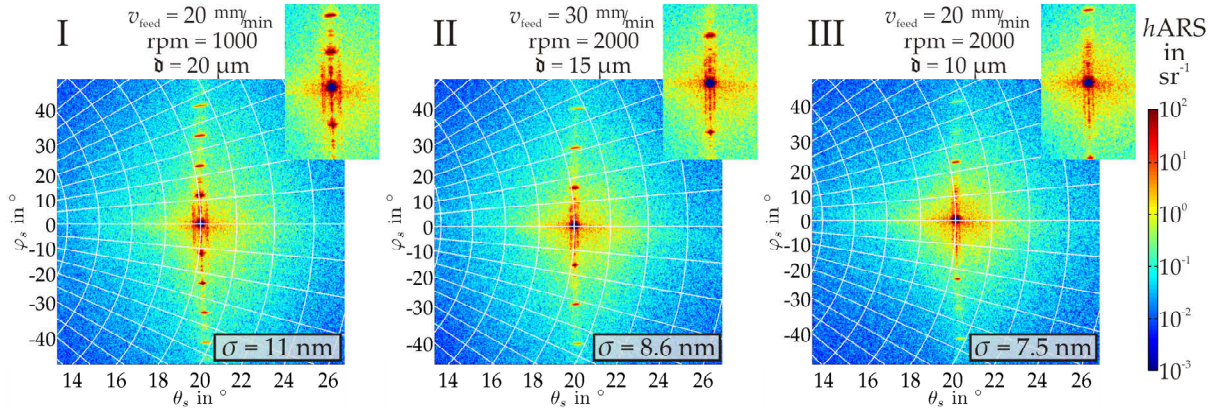


Fig. 6.3.: $hARS$ of three diamond turned surfaces fabricated with different feed periods. The insets show a magnification of the central $hARS$ parts. v_{feed} : feed velocity; rpm: number of rotation per minute; d : feed period. $R_T=450\text{ }\mu\text{m}$ for all samples.

circle sections. By calculating z_0 as a function of the diamond tool radius R_T and the feed period d , the roughness of the SPDT structure component is given as

$$\sigma_{SPDT} = 0.3z_0 = 0.3 \left(R_T - \sqrt{R_T^2 - (d/2)^2} \right). \quad (6.2)$$

In the limit of $R_T \gg d$ this relation corresponds to a quadratic behavior of the intrinsic roughness as a function of feed period. Numerically identical results were derived for an elliptical tool or with a different approximation in [251] and [252, p106], respectively.

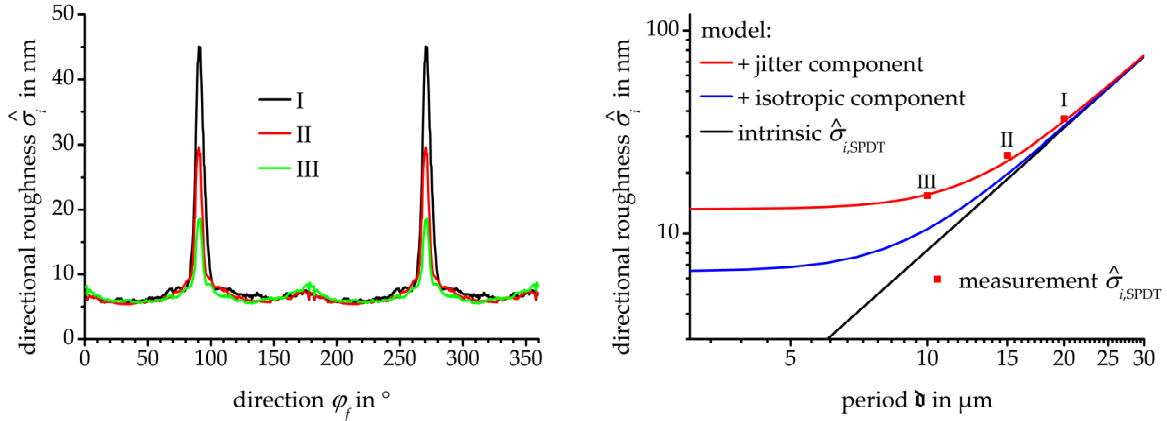


Fig. 6.4.: Left: Directional roughness values $\hat{\sigma}_i$ of the three SPDT surfaces. Right: Evolution of the SPDT roughness component as a function of the feed period.

Comparison of the theoretical curve for $R_T=450\text{ }\mu\text{m}$, represented by the black line in the right part of Fig. 6.4, with the measured SPDT roughness components shows considerable deviations in particular for the lowest feed period. However, Eq. 6.2 does not include further roughness components which are also present in the direction of the feed marks. If the isotropic component is added⁶, the deviations are reduced, but there is still a gap remaining. A closer look on the $hARS$ at scattering angles between the diffraction peaks and the specular reflex (insets, Fig. 6.3) reveals additional roughness components, which, if integrated excluding the peaks and subtracting the isotropic background, give a

⁶ Addition of these unidirectional roughness components: $\sigma = \sqrt{\sigma_{SPDT}^2 + \sigma_{iso}^2}$, see Eq. 6.1 or [62, Ch.4.3].

roughness contribution of about 10.5 nm in the same direction as the turning marks. By adding these components (excluding the peaks), the theoretical curve fits almost exactly the measured roughness values. The sources of these components are additional Fourier orders and the jitter of the height and of the feed of the turning tool from revolution to revolution, as discussed in [149] and [62, Ch.4.3].

The achievable roughness for the material/tool combination presented is the isotropic roughness component of about $\hat{\sigma}_i=6.5$ nm. This low roughness is only achievable without any jitter of the turning tool, if the feed period is below 5 μm . However, the absence of jitter would reduce the roughness components outside the turning direction as well. Hence, the best possible roughness for a perfect turning process could be even lower.

(An-)Isotropy parameters In the following analysis, the SPDT surfaces and a polished cylindrical lens⁷ are compared by different anisotropy parameters. The anisotropic lens structure can be identified in the $h\text{ARS}$ (Fig. 6.5, left) as three lines of increased scattering, that cross in the specular reflex. This structure is represented in the topography by three directed, but in contrast to the SPDT surfaces, non periodical roughness components. However, in particular the third component is only visible to the trained eye.

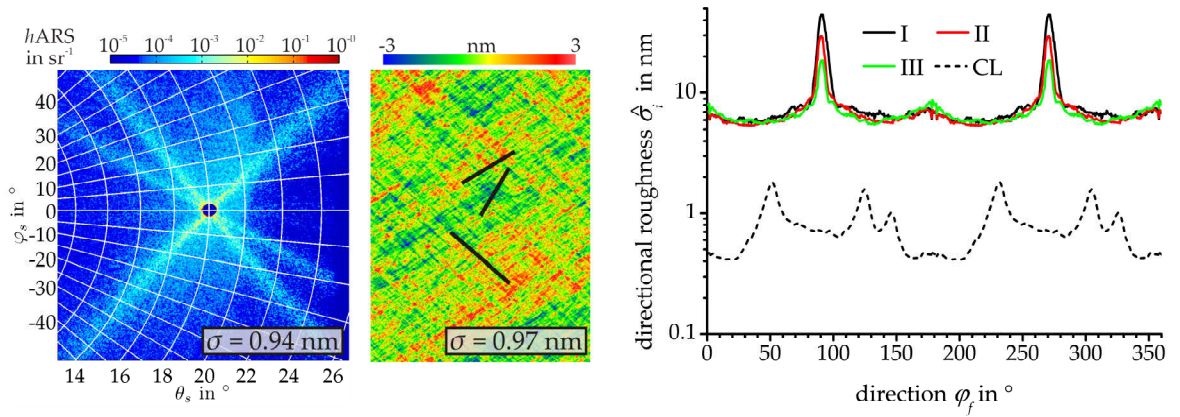


Fig. 6.5.: Left: $h\text{ARS}$ and WLI topography data ($10\times$ objective, $698\times 523\mu\text{m}^2$) of a polished, cylindrical fused silica lens (CL). The black lines indicate the directional roughness structures, which cause the anisotropic scattering. Right: Directional roughness values $\hat{\sigma}_i$ of the lens and the diamond turned surfaces. From these distributions the isotropy parameters are derived.

Three possible anisotropy parameters based on Eq. 6.1 are now defined and discussed. They enable the quantification and comparison of optically relevant anisotropy properties and provide an analysis tool to identify the scattering from scratches (see Sec. 6.4).

- $\hat{\sigma}_{\text{std}}$ is defined as the standard deviation of the directional roughness values $\hat{\sigma}_i$.
- $\text{PV}_{\text{ACF},\hat{\sigma}}$ is inspired by the ARS based procedure presented in [247]: The peak to valley difference of an autocorrelation function of the ARS at fixed θ_s along the azimuthal scattering angle φ_s is evaluated. This approach was transferred by replacing ARS with $\hat{\sigma}_i$ and φ_s with φ_f . For a perfect isotropic surface $\text{PV}_{\text{ACF},\hat{\sigma}}$ is 1.

⁷ The (pre-)polished fused silica lens was provided by Hellma Optics, Jena.

6. Light scattering properties of optical surfaces and thin films

- $\mathbb{D}_{|\text{mean-med}|}$ is defined as the modulus difference of the arithmetic mean and the median of the $\hat{\sigma}_i$. Therefore, the parameter is especially sensitive if single outliers exist.

To compare the isotropy of differently rough surfaces, the $\hat{\sigma}_i$ values are normalized to the rms roughness. In addition, the parameters should be determined for the same spatial frequency ranges, Δf and $\Delta\varphi_f$, and with identical discretization in φ_f . The anisotropy parameters are a function of the discretization in φ_f , since a finite $\Delta\varphi_f$ is unavoidable for 3D-PSD functions with discrete data. Thus, as for the rms roughness, the isotropy parameters are bandwidth limited. Otherwise, the $\Delta\varphi_f$ interval should be high enough to average out the influences of the speckle pattern. Therefore, the parameters in Tab. 6.1 were determined for $\Delta\varphi_f=4^\circ$ and with a sampling period of 0.5° .

Tab. 6.1.: Isotropy parameters determined from *hARS* for the SPDT surfaces and the cylindrical fused silica lens. Moreover, the corresponding parameters for ideally isotropic surfaces are given.

	SPDT			cylindrical lens	isotropic surface
	I	I	III		
$\hat{\sigma}_{\text{std}}$	0.61	0.46	0.28	0.40	0
$\text{PV}_{\text{ACF},\hat{\sigma}}$	0.58	0.75	0.90	0.79	1
$\mathbb{D}_{ \text{mean-med} }$	0.21	0.13	0.08	0.06	0

As expectable from the decreasing SPDT roughness components of the surfaces I to III the isotropy is improving with reduction of the feed period. Nevertheless, the rating of the cylindrical lens in the context of the diamond turned surfaces is interesting as it is classified close to sample II by the parameters $\hat{\sigma}_{\text{std}}$ and $\text{PV}_{\text{ACF},\hat{\sigma}}$. Parameter $\mathbb{D}_{|\text{mean-med}|}$, in contrast, states an isotropy that is slightly better than that of sample III. This would also be the intuitive assessment if the corresponding surface profiles are directly compared and empirically judged (Figs. 6.1 and 6.5).

However, the anisotropy rating is somehow subjective and the parameters derived have to be adapted in the context of the application of the optical surface. For the anisotropy assessment of optical surfaces, the classification of the third parameter $\mathbb{D}_{|\text{mean-med}|}$ should be preferable. The scattering of a single exposed directional roughness structure is more critical than several directions of comparable increased roughness levels with a 3D-ARS closer to a homogeneous background scattering. The arithmetic mean is sensitive for these roughness outliers, whereas the median is not. Hence, their difference is well suited as a corresponding measure.

6.1.2. Anisotropic roughness of magnetorheologically finished surfaces

To obtain the results presented in this section, the scattering sensor and the anisotropy methodology were employed for a fast, close to process - almost in-situ - evaluation of surfaces polished with MagnetoRheological Finishing (MRF). Therefore, the scattering sensor was mounted within the processing environment beside the MRF machine for several experiments. In addition, the applicability of both, the MRF process for the

finishing of SPDT electroless nickel surfaces and of the sensor for the structure assessment should be evaluated.

MRF is a sub-aperture polishing process, whose key feature is a fluid ribbon that is formed on a rotating wheel if a magnetic field is applied (Fig. 6.6). The material removal induced by the ribbon is used to determine the surface figure, to locally correct for figure errors, and to smooth the surface roughness [242]. In particular the fact that the ribbon is primarily a fluid suspension of magnetic and abrasive particles in water, whose viscosity is adjustable by the magnetic field, has several advantages. The removal process is determined by shearing forces so that the normal load on a surface is negligible [253]. Therefore, the removal rate can be very precisely defined by the dwell time, whereas deviations of the penetration depth into the ribbon have negligible influence on the accuracy of the figure correction [242,254]. In addition, the process is supposed to induce only very low levels of sub surface damage, since its formation is attributed to normal stress [241,255,256].

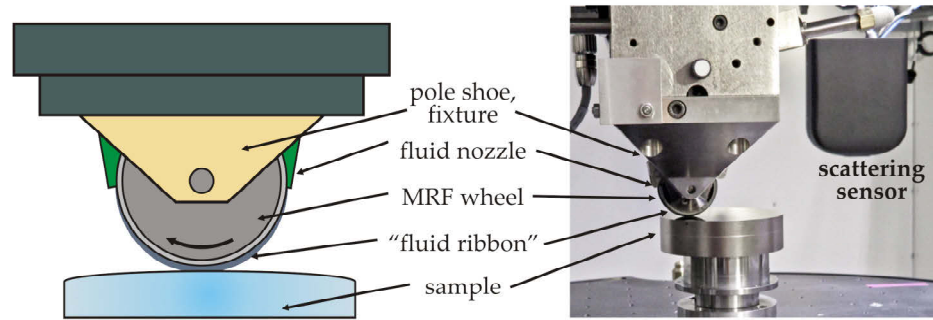


Fig. 6.6.: Left: Scheme of an MRF machine. Right: Light scattering sensor mounted in the MRF set-up.

At the Fraunhofer IOF the MRF machine⁸ has been applied so far to fused silica for which roughness values below 0.7 nm have been achieved [257]. However, the same finishing fluid can behave dramatically differently if applied to other materials and can even result in roughening [242]. In particular for soft or polycrystalline materials, achieving low roughness levels even below 1.5 nm seems to be challenging [242,254,256,258].

In the experiments⁹ whose results are presented here the MRF process was applied for the finishing of optical electroless nickel surfaces prepared by diamond turning. One of the main purposes was the removal of the feed mark roughness, as demonstrated for silicon or calcium fluoride in [253]. As mentioned above, achieving low roughness levels is additionally challenging as roughness values of 1.8 nm and 5 nm demonstrate for diamond turned nickel plated aluminum or diamond turned electroless nickel, respectively [256,258].

By mounting the scattering sensor within the MRF environment (Fig. 6.6, right), it became possible to provide a direct and very fast feedback about the influences of different process parameters on the surface quality. In particular, a 3D roughness characterization was mandatory, since the initial SPDT surfaces were anisotropic and the directional

⁸ MRF machine: QED Q22-950F polishing center; standard MR fluid with diamond abrasives.

⁹ Sample preparation by Matthias Beier, Roman Loose, and Marcus Trost (Fraunhofer IOF).

MRF process induces anisotropic surface features as well. Further preparations for the experiments were only the determination of the displacement of the finishing and the measurement area, the wiping of the sample surface to remove residue of the polishing fluid, as well as the reduction of the ambient light.

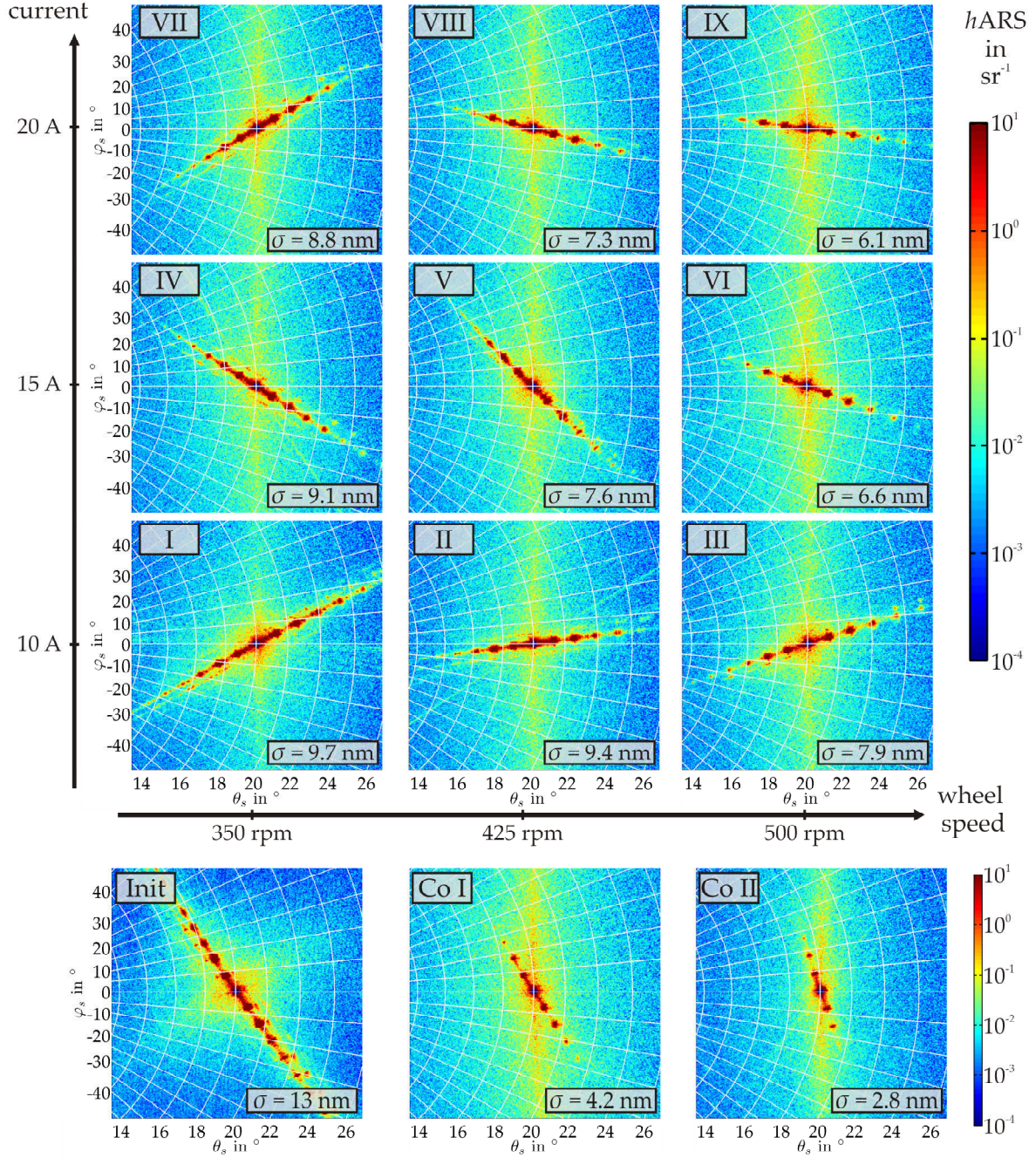


Fig. 6.7.: $hARS$ distributions of MRF processed positions on a diamond turned electroless nickel surface set up the base to analyze the roughness component evolution. The $hARS$ in the lower left (Init) is taken from the initial surface, whereas I to IX correspond to different parameter combinations of the wheel speed and the magnetic field driving current. Co I and Co II were obtained after combined sequences of processing steps with the parameter sets I and IX.

Figure 6.7 presents $hARS$ results obtained from MRF spots on a diamond turned electroless nickel surface which were fabricated with different process parameters. In addition, the lower row of the figure shows the $hARS$ of the initial surface, which exhibits signifi-

cant diffraction from the turning marks, and of two surface spots that were obtained by a two-step process after evaluation of the parameter matrix. For the different spots the revolutions per minute of the finishing wheel and the magnetic field generating current were varied. In a rough interpretation, these parameters correspond to the number of abrasive events per time and the viscosity or stiffness of the fluid, respectively. Besides the direct fluid properties, such as the chemical composition or the humidity, these parameters are varied to determine the removal rate [254] and, thus, should also influence the resulting roughness properties. The processing time of a single spot was only three seconds; the penetration depth into the fluid ribbon, which changes its form with the magnetic field, was kept constant at about 0.33 mm.

The $hARS$ distributions reveal two main roughness components that correspond to the diffraction at the diamond turning marks and the intrinsic MRF structure. The latter is represented by the increased scattering which is vertically orientated. Fig. 6.8 quantifies the corresponding $\hat{\sigma}_i$ values and illustrates them as functions of the processing parameters and of the MRF material removal depths obtained from topography data (WLI, $1\times$ objective).

The diffraction from the SPDT structure in the $hARS$ and, hence, the SPDT roughness component is reduced in the different steps compared to the initial surface. However, this effect is primarily influenced by the speed of the MRF wheel, whereas in particular for the step from 15 A to 20 A the magnetic field has only little effect (Fig. 6.8, left). This is similar to the behavior reported for experiments with the MRF set-ups in [255] or in [259] in which the material removal rate remains constant for magnetic fields emerging from currents higher than 5 A or 12.5 A, respectively.

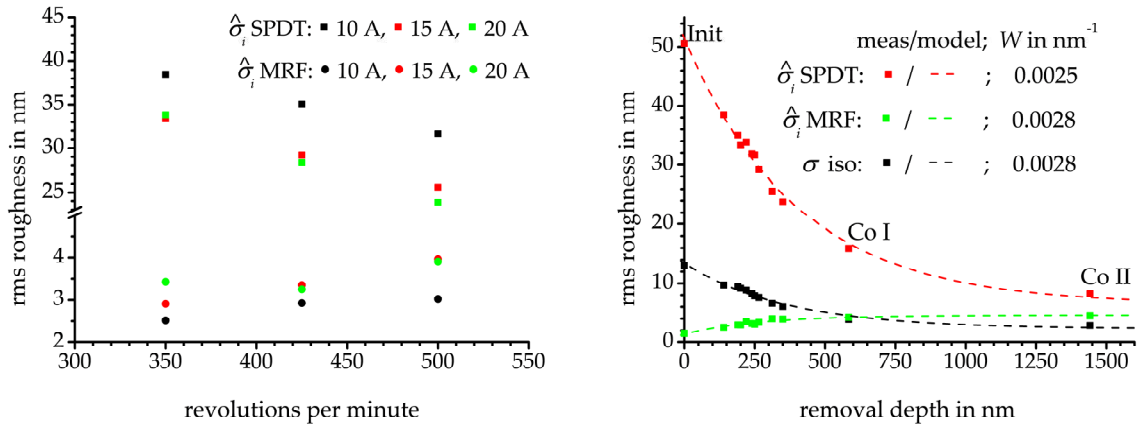


Fig. 6.8.: Evolution of $\hat{\sigma}_i$ for the MRF and SPDT structure components as functions of the current and the rotations per minute (left) of of the removal depth (right).

The intrinsic MRF roughness components, represented by the quite diffuse, vertically orientated $hARS$ structure, increases from the lower left to the upper right parameter set (Fig. 6.8). However, the relations of the MRF components to the process parameters are similar to that of the SPDT component, but inverted and less pronounced (Fig. 6.8, left). The properties of the MRF roughness components are slightly different from those of the

cylindrical lens (Sec. 6.1.1, p 55), since they do not cause a star-like *hARS* pattern with tapering lines close to the specular reflex. The MRF structure is wider and more diffuse. In surface topography modelling this corresponds to shorter groove lengths of the MRF structure compared to that in the lens structure.

Analysis of the topography data of the initial surface revealed cusp heights of the feed marks of 60 nm. In contrast, the removal depths range from 100 nm (set I) up to 325 nm (set IX) per spot. However, even this highest removal (IX) could not flatten the feed marks completely, for which a remaining amplitude of 15 nm was determined. Therefore, two combined two-step processes were tested to exploit the parameter sets IX and I with the highest removal of feed marks and the lowest intrinsic MRF roughness, respectively. Moreover, the dwell times of the combined processes, which were Co I: $(2 \times \text{IX} + 2 \times \text{I})$ and Co II: $(4 \times \text{IX} + 6 \times \text{I})$, were increased by multiple steps to improve the turning mark removal.

As indicated by the *hARS* of Co I and Co II (Fig. 6.7, lower row), the diffraction from the feed marks could be dramatically reduced by the increased removal. However, an feed mark amplitude of about 10 nm is still remaining, even for the removal of 1440 nm by Co II. Although indicated by the Co II *hARS* shown, the MRF roughness component was not significantly reduced either. Three processed spots with identical MRF parameters revealed a limiting value for the MRF component of about 4.1 nm.

However, the additional processing spots extend the right hand side diagram in Fig. 6.8, which now reveals an exponential decay of the SPDT roughness component with the removal depth; the isotropic component shows a similar progress; that of the MRF component is inverted. These trends can be approximated as a function of the material removal depth (MRD) with an initial value σ_{init} and a limit roughness σ_{∞} :

$$\sigma = (\sigma_{\text{init}} - \sigma_{\infty}) e^{-W \times \text{MRD}} + \sigma_{\infty} . \quad (6.3)$$

Equation 6.3 was originally derived based on wear mechanisms for vibratory finishing [260], but was also observed for MR finishing of soda lime glass surfaces by analyzing R_a , the 1D arithmetic mean surface roughness, parallel to the finishing direction [261,262].

One mentionable fact is that the parameter W for the fitted curves in Fig. 6.8 is almost identical for both roughness components as well as the isotropic roughness. Nevertheless, the effect of the SPDT removal on the isotropic roughness is much higher than the roughening; therefore, overall a roughness reduction is achieved. By further increasing the dwell time, the turning marks should be completely removed; thus, following Eq. 6.3, an isotropic roughness limit of about 2.3 nm can be achieved. This value is in the order of the average roughness level of the better polished regions of the sample which is analyzed in the following (Fig. 6.9, p. 61).

So far, only the small sections of the MRF processed surfaces were investigated; the question, if the removal of the diamond turning structure is a function of the orientation of feed marks and MRF wheel direction, is left open. Using the directional roughness

methodology the answer can be found by analyzing the spatial distributions of isotropy and roughness. Since the adjustment requirements of the sensor are considerably lower than for AFM and WLI, it is well suited for the fast, full-surface characterization including *h*ARS, roughness, and isotropy analyses.

To map the nanostructure properties, the sensor was combined with an automated *x-y*-stage and raster scans with 0.5 mm step width were performed. From the *h*ARS the directional roughness values, the isotropy parameter $\mathbb{D}_{|\text{mean-med}|}$, and the direction of the highest $\hat{\sigma}_i$ -component were determined. Besides the anisotropy properties, the maps reveal the homogeneity of the surface and the distribution of defects or contaminations. The latter are in particular apparent in the upper right part of the sample map.

To reduce the initial SPDT roughness, the feed period of this surface was only 2 μm which corresponds to a spatial frequency $f=0.5 \mu\text{m}^{-1}$. In addition, the MRF processing time was even longer than that of the combined processes to achieve an improved reduction of the feed marks. The average roughness level of the defect-free areas in which the MRF and the SPDT processing directions were not parallel revealed the limiting roughness level of about 2.3 nm predicted from Eq. 6.3.

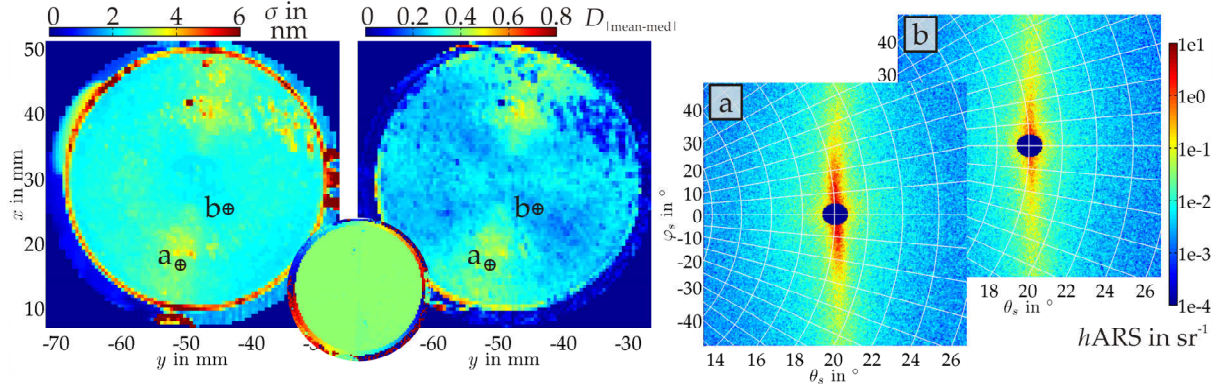


Fig. 6.9.: Mapping of the roughness (left) and the degree of isotropy (center) of a diamond turned surface after MR finishing. The small circular inset shows the constant direction of the dominant roughness component over the surface. Moreover, the *h*ARS distributions of significant positions are given in the right part of the figure.

Since the initial surface was fabricated in a spiral pattern and the direction of the dominating MRF component is constant over the surface (small map inset in Fig. 6.9), the MR finished surface comprises all combinations of MRF and turning mark directions.

The map of the anisotropy parameter (Fig. 6.9, center) reveals suspicious areas in which the isotropy is locally, but symmetrically to the sample center, changed. In addition, the rms roughness map reveals increased roughness levels at the same surface sections at which the MRF direction was parallel to the directions of the turning marks.

In the right part of Fig. 6.9, *h*ARS distributions of two representative positions on the MRF surface are compared. Although the *h*ARS of all positions on the MRF sample reveal neither diffraction marks nor a direction of increased scattering, besides the intrinsic MRF component, the scattering in the MRF direction is markedly higher at positions at

which the MRF direction and turning marks were parallel. However, even at the highest *h*ARS levels the *h*ARS and additional 3D-PSD function from WLI topography data did not reveal discrete peaks. Hence, the most significant part of the turning marks and in particular the periodicity was removed. Nonetheless, the influence of the orientation is demonstrated; the mechanism responsible for the turning mark removal - the shearing forces - are less effective for a parallel orientation if virtually no surface gradients are seen by the abrasive particles.

So far, these first tests revealed very promising results for the application of the scattering sensor in combination with the anisotropy methodology to improve the MRF process. However, with the standard polishing fluid, MRF is not applicable to the final finish of metallic optical surfaces for the visible spectral range. The starting point for further improvements of the roughness level will be the polishing fluid [242], whose influence was not investigated in this thesis.

6.1.3. **Concluding remarks**

The thorough characterization of surfaces fabricated by diamond turning and by different polishing processes demonstrates the suitability of the light scattering sensor for roughness measurements and elaborated anisotropy analyses. In this context, a novel methodology for the evaluation of directional roughness properties and for the derivation of isotropy parameters was developed and analyzed.

The methodology enabled the analysis and modeling of roughness components of SPDT surfaces, fabricated with different feed parameters; the comparison of the anisotropy properties of SPDT surfaces and an anisotropically polished fused silica lens; and the optimization of magnetorheological finishing. In particular for the final point, the close-to-process, almost in-process, measurements provided by the scattering sensor could be exploited to find optimal MRF operation parameters for the removal of diamond turning marks and low intrinsic MRF structures. In addition, the sensitivity of the resulting surface structures to the relative orientation between the MRF processing direction and the turning mark direction was demonstrated in the full surface roughness and isotropy analysis with the scattering sensor.

6.2. Roughness evolution of titanium thin film coatings

Thin metallic films are used in a wide area of applications ranging from optical elements - broad band mirrors or metallic reflecting attenuators - to other functional surfaces, as in hard disk drives or for thermal insulating vessels. In optics, in particular roughness growth as a function of thin film thickness is critical: On the one hand, a minimal thickness is required for a high reflectance; on the other hand, the roughness, which is increasing with the thin film thickness, is a source of scattering losses.

In the next section, means to extend the spatial frequency range of the scattering sensor to cover the thin film roughness relevant spatial frequency range will be presented. Thereafter, a detailed analysis of the roughness evolution of titanium films on anisotropic substrates is presented and a corresponding evaluation procedure is developed. It is demonstrated that the frequency range covered by the sensor includes the transition between the substrate and the thin film roughness. In combination with the 3D capability of the sensor, this can be exploited to study the anisotropy evolution.

Titanium was selected as test film material to generate representative surfaces of different roughness levels for the sensor and the analysis technique development. In addition, the opaque titanium films are supposed to have an extended stability to corrosion [263,264], compared to aluminum films [265]. Hence, changes in the surface structure between the different characterization steps should be avoided.

6.2.1. Adaption of the light scattering sensor

First PSD results of a 600 nm titanium film on a glass substrate, obtained from topography and *h*ARS data, are compared in Fig. 6.10 to motivate the sensor modifications required for thin film characterization. The PSD functions reveal three (relevant) facts: (I) the PSD determined from a scattering sensor measurement, fits the Master-PSD very well; (II) the higher spatial frequencies, in which intrinsic thin film roughness components are dominant, are not included in a sensor measurement; (III) the Master-PSD can be described by the PSD models presented in Sec. 3.2.2.

The second fact is, on the one hand, a consequence of the specific substrate/thin-film combination; on the other hand, the literature reveals similar relevant spatial frequency ranges for several optical thin films [5,164,266].

Since the PSD model fits the specific roughness characteristics, it can be exploited to extrapolate the roughness information beyond the covered spatial frequency range. However, it would be favorable to extend the frequency range of a measurement to provide the opportunity for interpolation. Therefore, the implementation of a second illumination channel is analyzed. This extension aims in particular on the plateau section of the Master-PSD at $f \approx 1 \mu\text{m}^{-1}$, there the intrinsic thin film roughness is dominating.

With regard to the grating equations (Eq. 3.2), there are three quantities that can be exploited to increase the spatial frequencies: the illumination wavelength, the scattering

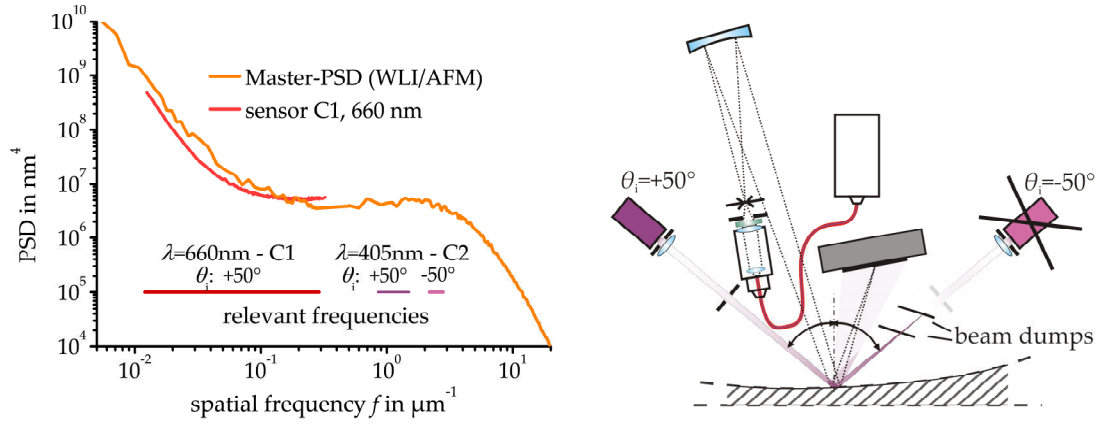


Fig. 6.10.: Left: The comparison of a Master-PSD of a 600 nm titanium film to a $\text{PSD}_{2\text{D},\text{iso}}$ determined from $h\text{ARS}$ demonstrates the lack of significant spatial frequencies in a measurement with the primary illumination channel ($\lambda=660$ nm, C1). In addition, the spatial frequency ranges of both illumination channels are depicted. Right: Scheme of possible configurations for the second illumination channel ($\lambda=405$ nm, C2).

angles, and the incidence angle. To use the existing sensor geometry with a single detector matrix and to perform the measurements without sample or detector movement, which would contradict the sensor concept, the parameter set is reduced to λ and θ_i . As a consequence, a second illumination channel with a reduced wavelength of $\lambda=405$ nm and an increased incidence angle of $\theta_i=50^\circ$ was implemented.

The chosen wavelength, for which compact, cost-effective laser diode modules are available, is at the lower band edge with significant quantum efficiency of the CMOS matrix. $\theta_i=50^\circ$ is a compromise of the accessibility of high spatial frequencies and of an implementation within the sensor housing. In the following, the 660 nm (primary) and the 405 nm (secondary) illumination channels are referred to as C1 and C2, respectively.

The frequency range opened up by C2 extends from $f=0.85\mu\text{m}^{-1}$ to $1.5\mu\text{m}^{-1}$. Higher frequencies would be achieved for a highly negative incidence angle (e.g. -50°), for which, however, the beam would interfere with the beam dumping arrangement. It is interesting to note that the bandwidth for both channels is about $\Delta f=0.6\mu\text{m}^{-1}$ ($-0.3\mu\text{m}^{-1} \dots 0.3\mu\text{m}^{-1}$ for C1). However, in a log-log scale the bandwidth of C1 is more than one and a quarter decade, whereas for C2 it is only about a quarter decade.

Unfortunately, the specularly reflected beam is not included in the scattering angles covered by the CMOS matrix if $\theta_i < 10^\circ$ or $\theta_i > 25.5^\circ$ and, hence, the isotropy information is not included in measurements with C2 as well. Otherwise, it was observed previously [247] and in the context of this thesis that the intrinsic thin film roughness shows an isotropic structure. This structure can even obscure anisotropic surface features of the underlying substrate at the C2 relevant frequencies, as will be shown. Hence, anisotropy is for measurements of thin film roughness with C2 of reduced interest.

6.2.2. Roughness and anisotropy evolution of titanium thin films

Titanium thin films with thicknesses d of 200 nm, 600 nm, and 1000 nm were deposited in a magnetron sputtering process¹⁰ with increased argon pressure on two types of differently polished glass substrates. The analysis results for a conventionally polished Schott RG1000 glass are discussed in this section to work out the characteristics of anisotropy and thin film roughness evolution.

Roughness evolution - measurement and modeling

Figure 6.11 summarizes the $hARS$ distributions obtained with both illumination channels together with the corresponding partially integrated scattering values S . The data reveals an increasing scattering with the film thickness for both channels. However, in particular the scattering levels determined using C2 show considerably higher S -ratios than those determined using C1. These differences are consequences of the different spatial frequency ranges in which the roughness properties are dominated either by the influence of the substrate (C1) or the thin film (C2). An additional observation in the C1- $hARS$ is the improving isotropy with the increasing film thickness, which indicates the isotropic surface structure of the growing film in contrast to the anisotropic substrate.

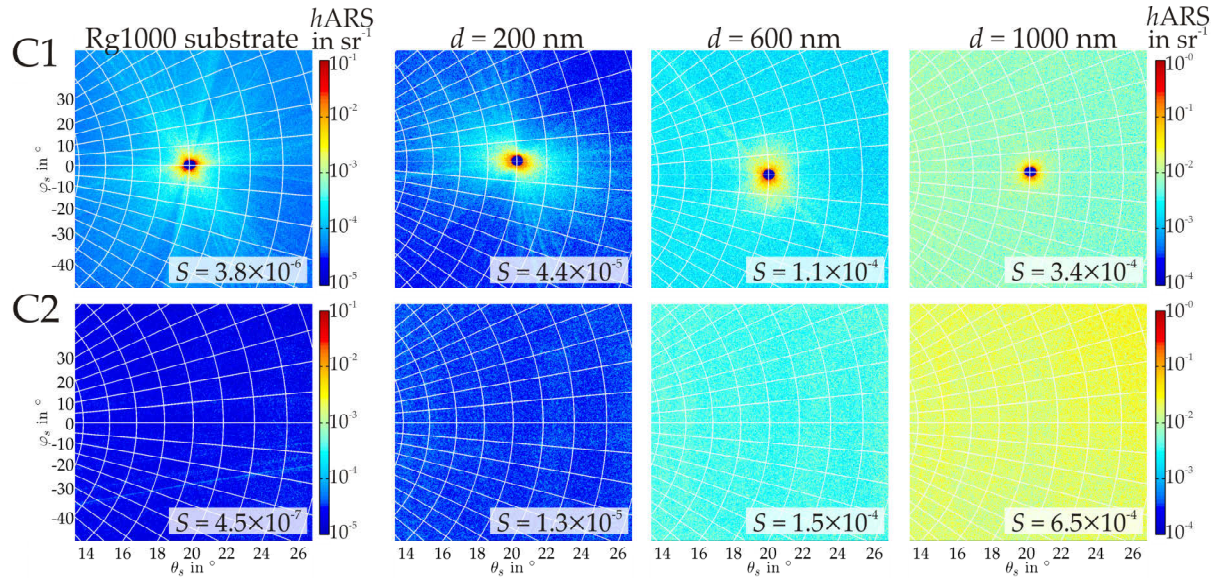


Fig. 6.11.: $hARS$ distributions of the substrate and the Ti thin films for both illumination channels (different scale for the substrate). In addition, the integrated scattering values S are given.

The PSD sections determined from the $hARS$ (Fig. 6.12, left) represent the same roughening trend, which is in particular emphasized by the sections obtained from the C2 $hARS$. On the other hand, almost identical PSD functions are observed at $f \lesssim 0.03 \mu\text{m}^{-1}$ for all samples; in particular, the PSD data of the substrate and the 200 nm film are virtually identical¹¹. This indicates that the roughness relevant for C1 is primarily determined by

¹⁰ Thin film deposition by Thomas Müller, Fraunhofer IOF.

¹¹ The contradiction between the identical C1 PSD sections and the difference in S (factor 10) for the substrate and the 200 nm film is attributed to the optical factor, which increases with the reflectivity.

the replicated substrate roughness. (At higher spatial frequencies, the C1 PSD of the substrate seems to be influenced by instrument noise; the low reflectivity of the pure RG1000 causes an $hARS$ level which is close to the sensitivity limit of the sensor (Sec. 4.3.2, p. 32).)

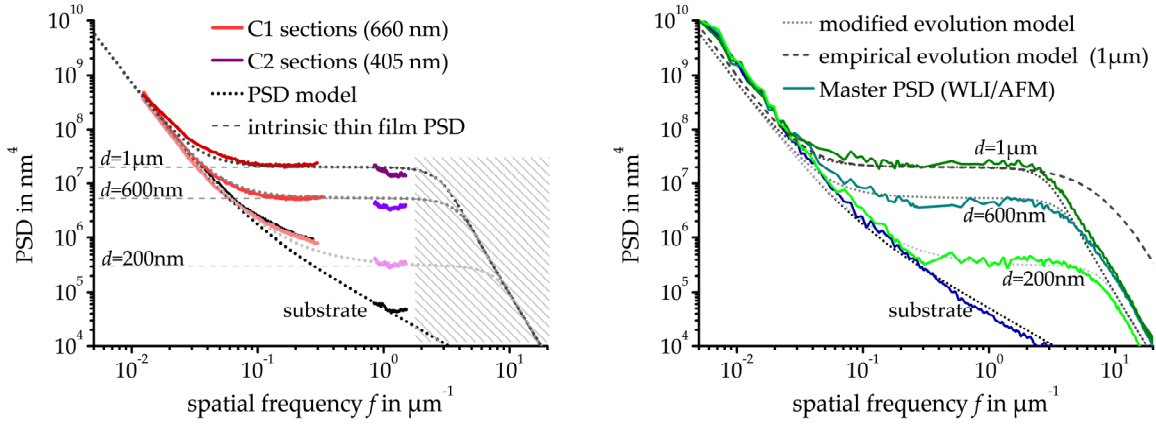


Fig. 6.12.: Left: Determination of the interpolated PSD model functions from the PSD sections obtained with C1 and C2. Parameters: $\Omega=0.32 \text{ nm}^3$, $\beta=1.3$, $\nu=0.11 \text{ nm}^3$, $\eta=4$, $K_1=552$, $n_{K,1}=2.05$, $K_2=50000$, $n_{K,2}=0.35$. Right: Comparison of the interpolated PSD functions to Master-PSD functions determined from the topography data. The dashed curve (right) demonstrates the deviations of the PSD cut-off if the empirical evolution model would be used.

To bridge the gaps in the PSD sections and to verify the scattering based evolution modeling, combined Master-PSD functions from WLI and AFM topography data (Fig. 6.13) were determined, which are illustrated in the right part of Fig. 6.12. In the AFM scan areas in the lower row of Fig. 6.13, the granular structure of increasing size verifies the isotropic character of the intrinsic thin film roughness at least for $f \gtrsim 0.3 \mu\text{m}^{-1}$. On the other hand, the red-green contrast in the WLI images shows identical long range structures, which are superimposed by the granular film structure for increasing film thickness.

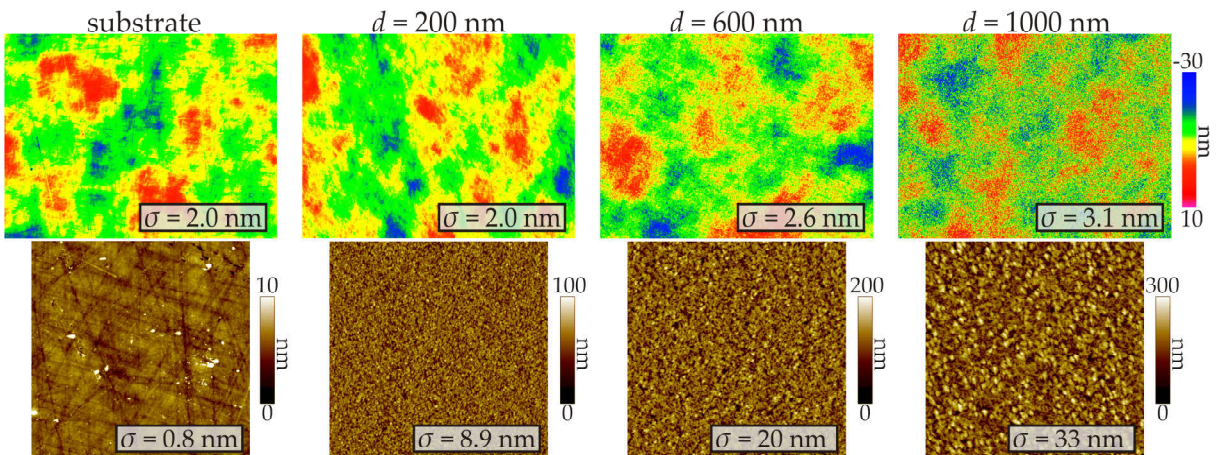


Fig. 6.13.: Topography images of the Ti thin films on the RG1000 substrates obtained by WLI ($10\times$ objective, $698\times 523 \mu\text{m}^2$; top) and AFM ($10\times 10 \mu\text{m}^2$; bottom) measurements.

The progresses of the Master-PSD functions correspond almost perfectly to those of the modified roughness evolution model. As a consequence, the PSD sections determined

from the h ARS of both illumination channels are connectable by this PSD model, as demonstrated in the left hand side diagram of Fig. 6.12.

The fitting procedure would start from the PSD sections obtained with C2, since this part of the PSD can be assumed to be independent from the substrate parameters (K, n_K) and thin film PSD cut-off parameters (ν, n_Ω). For the samples presented, the C2 PSD sections are almost horizontally and, therefore, the cut-off of the thin film PSD is not included in the C2 measurement. Hence, Ω and, if results for different thicknesses are available, β can be adapted. (ν and n_Ω were determined using the topography based PSD functions to complete the model.)

With Ω and β adjusted, the high spatial frequency sections of the C1 PSDs are partially determined, too. Subsequently, the parameters K and η_K can be determined by fitting the PSD functions at the substrate dominated low spatial frequencies and the not yet determined remaining parts of transition between substrate and intrinsic thin film roughness. Figure 6.12 shows the good correlation between the interpolated PSD functions and the topography based Master-PSD functions. In addition, the constituting model PSDs are given, which show that for a description of the substrate the sum of two fractal PSD functions was applied.

Exploiting the modeling procedure and the PSD sections derived from both illumination channels, it becomes possible to determine interpolated roughness values (Tab. 6.2) that extend over a spatial frequency bandwidth of about two decades ($f=0.015\mu\text{m}^{-1}$ to $1.5\mu\text{m}^{-1}$) with scattering sensor measurements. This is almost the same bandwidth (in log-scale) as that of a single AFM or WLI scan and, moreover, comparable to a PSD from a goniometer based ARS measurement at a single wavelength. However, to obtain the same information from topography data, a combination of at least two different scan areas would be necessary to exclude typical artifacts.

Tab. 6.2.: Comparison of the roughness evolution, the degree of anisotropy, and the transition frequency of the titanium coatings on the RG1000 substrate. († same bandwidth; $\hat{\sigma}_{\text{std}}$, f_{trans} and the 200 nm film on a superpolished substrate (sps) are discussed in the following)

	substrate	200 nm	600 nm	1000 nm	200 nm on sps
σ^\dagger from h ARS, interpolated	1.0	1.8	6.3	12.1	1.5
σ^\dagger from Master-PSD	1.1	1.9	5.8	12.9	1.4
anisotropy parameter $\hat{\sigma}_{\text{std}}$	0.20	0.16	0.08	0.02	0.02
f_{trans}	-	0.89	0.10	0.07	0.08

Figure 6.14 illustrates the advantages of PSD functions obtained with the scattering sensor compared to PSD functions determined in different topography scan areas. The latter can show large deviations that are, for example, caused by the low-pass function of the WLI objective or aliasing effects in the AFM data [231,267]. It is almost impossible to derive a Master-PSD at $f \approx 0.2\mu\text{m}^{-1}$ for the shown topography PSD sections of a 200 nm Ti film on a superpolished fused silica substrate. The model PSD functions obtained with the scattering sensor benefit from the fact that the light scattering measurements are not

prone to these artifacts.

Aliasing is, in particular, relevant for the thin film roughness components in the horizontal PSD sections, there the PSD functions of the two AFM sampling areas differ by more than a half decade. An identical behavior is achieved if the PSD is calculated from a surface scan whose sampling distance was numerically reduced (Fig. 6.14, right).

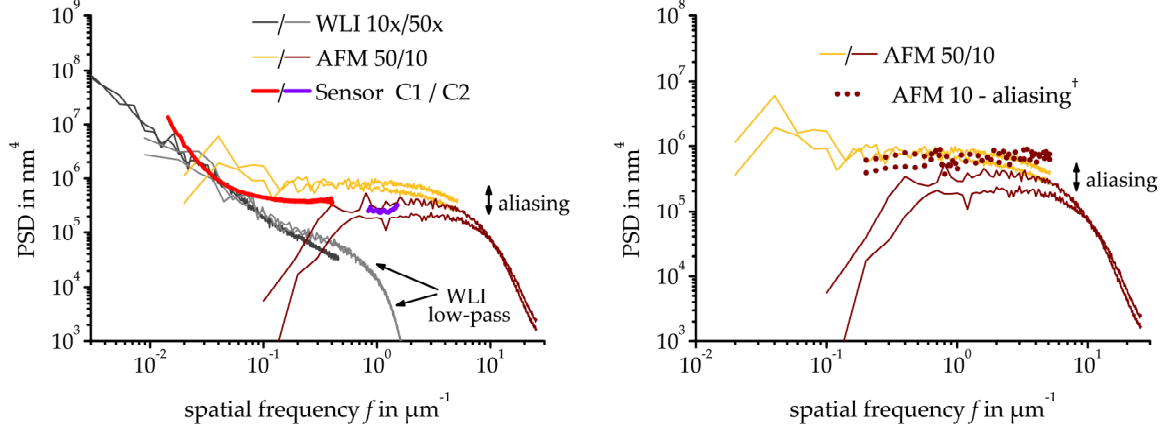


Fig. 6.14.: Artifacts caused by aliasing (AFM) or the optical transfer functions of the WLI objective complicate the determination of Master-PSD functions from topography data and demonstrate the advantages of the PSD functions obtained from *h*ARS distributions. (200 nm Ti film on superpolished fused silica, $\sigma_{\text{WLI/AFM}}=1.4$ nm) Right: [†] the lateral resolution of the $10 \times 10 \mu\text{m}^2$ AFM scans were numerically reduced to that of $50 \times 50 \mu\text{m}^2$ AFM scans to imitate aliasing.

Additional information on the roughness evolution can be obtained from the analysis of the roughness evolution parameters (Fig. 6.12) as well as the analysis of the isotropy properties (Tab. 6.2). For example Ω in the classical model corresponds to the average size of the thin film constituting elements; $\Omega=0.03 \text{ nm}^3$ or $\Omega=0.02 \text{ nm}^3$ were reported for amorphous silicon thin films, which is close to the atomic volume of silicon [86,102]. From the modified model, $\Omega=0.32 \text{ nm}^3$ for titanium was determined, which is factor 20 higher than the corresponding atomic volume of 0.018 nm^3 . This can correspond to the polycrystalline behavior of metals, such as tungsten or molybdenum, for which increased Ω were reported as well [86,102,268].

The value of 1.3 for β reveals a strong roughening, beyond the stochastic regime ($\beta=0.5$), which is for instance an indicator for columnar growth mechanisms [138] comprising a highly crystalline structure. On the other hand, within the empirically modified model the correlation of Ω to the thin film element size is maybe lost, since the parameter itself is indirectly altered by β or may change with the film thickness for non-linear growth mechanisms. Whether Ω can still be a measure for the size of the film constituting elements, has to be theoretically or experimentally verified in ongoing studies.

Analysis of isotropy evolution

The C1 *h*ARS distributions (Fig. 6.11) and the WLI topography data (Fig. 6.13) reveal a significant isotropy evolution with the thin film thickness, which is quantified by the

directional roughness values and the $\hat{\sigma}_{\text{std}}$ anisotropy parameters¹² in Fig. 6.15 (left). The anisotropy properties of the pure substrate and the 200 nm film are very similar, as for example the constriction in the directional roughness at $\varphi_f \approx 150^\circ$ or the $h\text{ARS}$ distributions demonstrate. This indicates the almost perfect replication of the substrate nanostructure. In contrast, the $h\text{ARS}$ and the directional roughnesses of the 1000 nm film are almost perfectly isotropic and the 600 nm film shows an anisotropic scattering primarily close to the specular reflex.

The evolution of the anisotropy parameter as a function of the radial spatial frequency for small intervals $\Delta f = 25 \times 10^{-4} \mu\text{m}^{-1}$ gives an even more thorough analysis. The slopes and levels of the resulting curves in Fig. 6.15 (right) are virtually identical for the substrate and the 200 nm film; hence, the anisotropy is not altered by the thin film in this spatial frequency range.

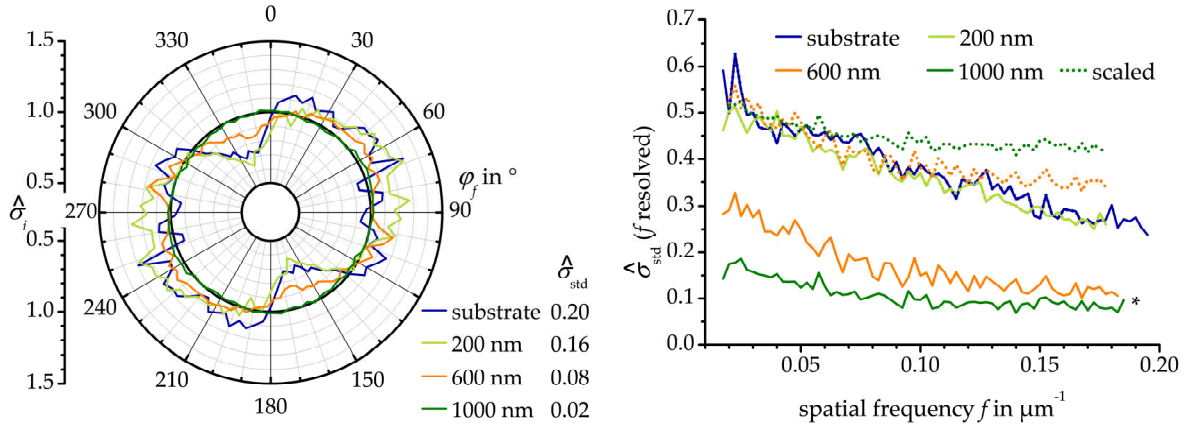


Fig. 6.15.: Comparison of the normalized directional roughness values (left) and the spatial frequency resolved anisotropy parameter (right) demonstrate the reduction of the anisotropy with increasing thin film thickness. From the right hand side diagram the transition frequencies between dominating substrate and thin film roughness were determined. The curves are scaled (overlapping at $f < 0.05 \mu\text{m}^{-1}$) to emphasize the anisotropy evolution. *) The stochastic fluctuations (speckle) in the small frequency intervals prevent a parameter $\hat{\sigma}_{\text{std}}$ of 0.

In contrast, the curves of the 600 nm and the 1000 nm films do not only reveal the reduced level of anisotropy at the entire covered spatial frequency range, but also exhibit different trends. Whereas the slopes of all (scaled) curves are identical at low frequencies, the curves for 600 nm and 1000 nm flatten out at transition frequencies f_t for which the anisotropy substrate structure vanishes and the intrinsic thin film roughness is dominant. At these spatial frequencies, the intrinsic thin film PSD model is about 5 times ($1/2$ orders of magnitude) higher than the substrate PSD model.

In the PSD model, the transition frequency is given analytically by the following relation¹³:

$$f_t = \sqrt[n_K+1]{\frac{5K}{\Omega} d^{-2\beta}} \propto \sqrt[n_K+1]{d^{-2\beta}} \quad \text{with} \quad 5 \times \text{PSD}_{\text{Sub}}(f_t) = \text{PSD}_{\text{int}}(f_t) \approx \Omega d^{2\beta}. \quad (6.4)$$

¹² For these surfaces $\hat{\sigma}_{\text{std}}$ was applied, since the anisotropic surface features are equivalently distributed scratch like structures and no dominating directional structures are visible (Fig. 6.13).

¹³ If PSD_{Sub} is given as the sum of two fractal models, f_t can only be derived numerically.

The corresponding values of f_t determined from the roughness evolution parameters are summarized in Tab. 6.2 on p. 67. It is obvious, that for a better or super-polished substrate with low K the thin film roughness would become critical at a lower transition frequency than for the RG1000 substrate. This is induced by the ratio of K and Ω - the parameters which define the levels of the constituting model PSD functions.

The value of the transition frequency provides a mean to define a critical film thickness (in combination with a deposition parameters) for a specific substrate at which the intrinsic thin film roughness is negligible. Hence, it becomes possible to state the maximal tolerable thin film thickness for a given substrate at which the scattering is purely dominated by substrate roughness. A high transition frequency, achieved by low thin film roughness for a (very) thin film, would be preferable. Nevertheless, a specific thickness is necessary to obtain the functional properties of the surface. Determining the transition frequency can define the level at which the roughness of a substrate is just good enough to be below the unavoidable thin film roughness.

6.2.3. Concluding remarks

The roughness and isotropy evolution of titanium coatings on anisotropic RG1000 substrates were analyzed in this section. In this context, the advantages of light scattering based nanostructure analyses applying the scattering sensor were emphasized, which were the fast 3D-capability and the reduced susceptibility for artifacts compared to topography based techniques. However, the implementation of a second illumination channel and the application of a combined PSD model, modified for arbitrary roughness evolution powers, were necessary to extend the spatial frequency range covered in a sensor measurement. These procedures enabled PSD functions in a spatial frequency range of 2 decades ($f=0.015\mu\text{m}^{-1}$ to $1.5\mu\text{m}^{-1}$) to be determined. This range is comparable to those of single AFM, WLI, or ARS-goniometer measurements.

The spatial frequency range covered in a measurement includes the intrinsic thin film roughness components and the transition from dominating film roughness to dominating substrate roughness. Therefore, a transition frequency at which the thin film roughness would become critical for the optical losses could be determined. To identify and derive this frequency, at which the top PSD of the thin film is no longer influenced by the substrate structure, the isotropy analysis methodology developed in Sec. 6.1 was applied.

The application of the sensor and the discussed analysis concept are in general not restricted to ex-situ characterization. Only little technical effort would be required to toughen the sensor for vacuum conditions, which enables in-situ studies of the roughness evolution within the deposition process. This effort should be considerably lower than that for the in-situ studies based on synchrotron x-ray scattering presented in [269].

6.3. Roughness induced scattering of complex multilayer systems

Multilayer coatings are the method of choice to achieve highly reflective or transmissive optical elements that provide tailored spectral properties. One of the most challenging filter types in interference coating fabrication are notch filters [270] which have narrow reflecting bands with steep edges and wide transmission ranges.

In this section, approaches for the light scattering based characterization of an exemplary notch filter¹⁴ that exhibits a high reflectance/blocking capability at a central wavelength of 642 nm and a bandwidth of only 34 nm is presented. In order to achieve the spectral notch, the filter consists of a quarter wave stack whose design is detuned following an equivalent layer approach [270,271]. The resulting stack with a thickness of 23 μm consists of 178 layers of Ta_2O_5 and SiO_2 as high index and low index materials, respectively, that were deposited in an ion beam assisted evaporation process¹⁵. In particular the accurate deposition of the single films with a wide range of thicknesses from 400 nm down to only 5 nm is challenging.

The notch design aims at the application in laser based fluorescence or in multi-photon microscopy to isolate the excited light, by reflection of the exciting light. Therefore, low scattering levels for the excitation wavelength are mandatory, since the power differences of the stimulating and stimulated light can exceed 10 decades¹⁶ [272,273]. High scattering levels of rerunning excitation light could reduce the blocking capability of the notch filter so that the light to be measured is outshined and occurring cross-talk effects limit resolution and sensitivity.

In the following, the development of a corresponding light scattering model is discussed. It is derived from 2D-ARS measurements recorded at 633 nm, a wavelength within the blocking band; at 532 nm, within the transmission band; as well as at 395 nm. For illustration purposes, the analysis is restricted to 2D curves, since no anisotropic surface structures were observed in topography measurements. After the identification of influencing factors, advantageous measurement conditions are identified, corresponding scattering sensor application scenarios are proposed, and first test results are discussed.

A detailed light scattering analysis of such a complex multilayer system is presented for the first time. Only in [274,275] basic measurement results of multi-cavity filters, which show an inverted spectral behavior than the notch filter, were discussed.

6.3.1. Development of the light scattering and interface correlation model

The left part of Fig. 6.16 shows in-plane ARS measurements in the reflection hemisphere of the notch filter for the wavelengths $\lambda=633\text{ nm}$, 532 nm , and 395 nm . If compared to

¹⁴ The sample was provided by Stefan Jacobs, Optics Balzers Jena GmbH.

¹⁵ By now a plasma assisted reactive magnetron sputtering (PARMS) process is utilized to achieve lower thin film roughnesses and to improve the thin film thickness accuracies.

¹⁶ A detailed estimation is presented in App. A.1.

532 nm, in particular the measurements at 395 nm and 633 nm exhibit considerably enhanced scattering levels at angles up to $\theta_s \approx 30^\circ$, which corresponds to increased scattering losses given (TS in Fig. 6.16). The "wings" of enhanced scattering in the ARS are caused by semi-resonant scattering mechanism as will be pointed out in the following. In addition, the comparison of a measured and modeled reflectance spectrum ($\theta_i = 6^\circ$) in Fig. 6.16 reveals a minor shift of the relevant reflectance band to longer wavelengths.

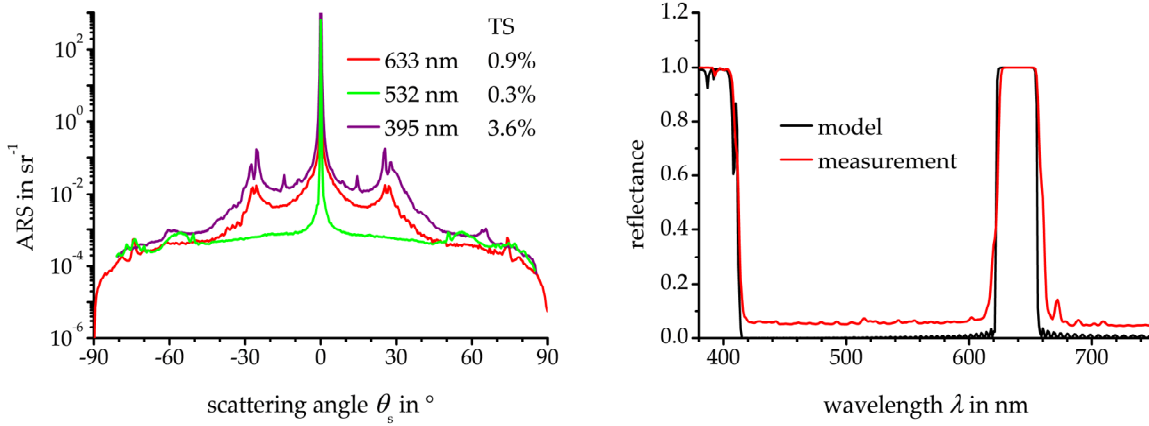


Fig. 6.16.: Left: Measured in-plane ARS distributions in the backward hemisphere for $\theta_i = 0^\circ$ at different wavelengths. Right: Reflectance spectra for $\theta_i = 6^\circ$.

For the later application, the scattering into the transmission hemisphere is of special interest, since light scattering of the excitation wavelength in the forward direction, which has to be blocked, would reduce the blocking capabilities of the filter. Therefore, the scattering at 633 nm (the available wavelength closest to 642 nm) was recorded in the transmission hemisphere, too. In addition, ARS results for illumination from the substrate side as well as from the thin film side together with the corresponding scattering losses are compared in Fig. 6.17.

The data reveal that an illumination from the substrate side is advantageous for the application, since the scattering loss in both hemispheres and in particular in the transmission hemisphere is more than one order of magnitude lower. On the other hand, the blocking capability is not altered. It is remarkable that in the transmission hemisphere the ARS level of the resonant scattering is only 1.5 decades below the intensity of the transmitted beam; hence, the scattered power is very close to the relevant specular power that defines the blocking capability.

Preliminary modeling results for the ARS at 633 nm in both directions, additionally given in the figure, reveal a good correlation in general, but also apparent deviations. The modeling parameters and assumptions applied are linear increasing PSD functions ($\beta = 0.5$) with partially correlated roughness and the ideal multilayer design. To improve the modeling results, physically meaningful parameters such as β or an average optical thickness deviation δ from the ideal multilayer [5,135] can be employed in the evaluation of Eq. 3.7. The influences of these two parameters, which were tested so far only for conventional quarter wave designs, on the ARS of the notch filter is summarized in the

next two subsections. To further improve the scattering model, two additional influencing mechanisms are discussed in the subsections thereafter.

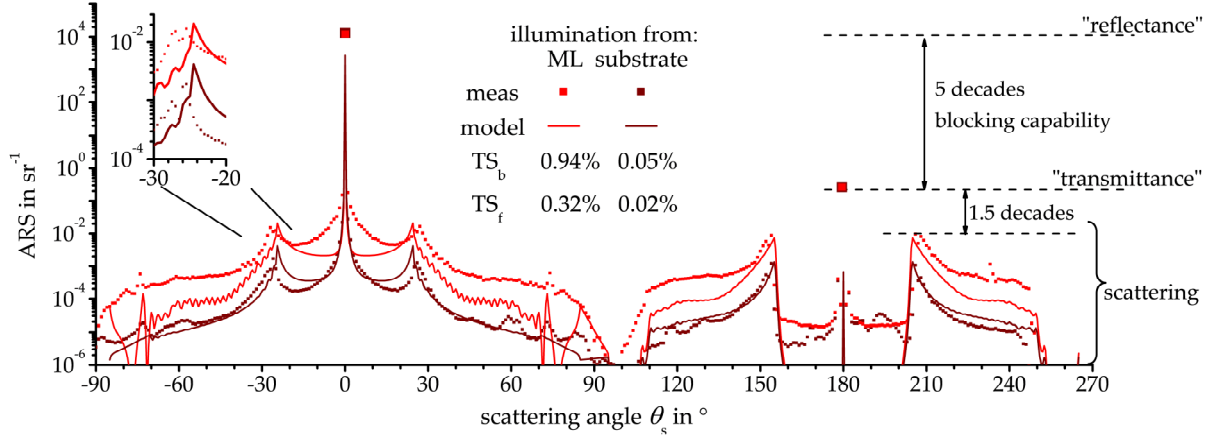


Fig. 6.17.: Modeled and measured ARS distributions for the reflection and transmission hemisphere with illumination from the multilayer or the substrate side ($\lambda=633$ nm, normal incidence).

Influence of spectral properties

A minor eye-catching deviation between the ARS model and the measurement are the slightly different positions of the enhanced scattering (Fig. 6.17). Since these "wings" are directly correlated to the spectral properties of the multilayer, they are sensitive for global deviations δ of the optical film thickness ($T_{\text{opt}}^* = (1+\delta) T_{\text{opt}}$). Such global deviations were discussed in several publications [135,140,141] and were impressively applied in [5,135].

The influences of different values of δ on the notch filter ARS as well as on the reflectance spectrum are summarized in Fig. 6.18. The curves reveal an improved correlation between measured and modeled data at the angles of resonant scattering for $\delta=0.005$. For this coefficient, the reflectance spectrum shows an improved correlation between the modeled and measured reflectance band as well. On the other hand, in particular the step from $\delta=0.005$ to $\delta=0.01$ increases the scattering loss TS_b by a factor of 2 from 0.7 % to 1.3 %

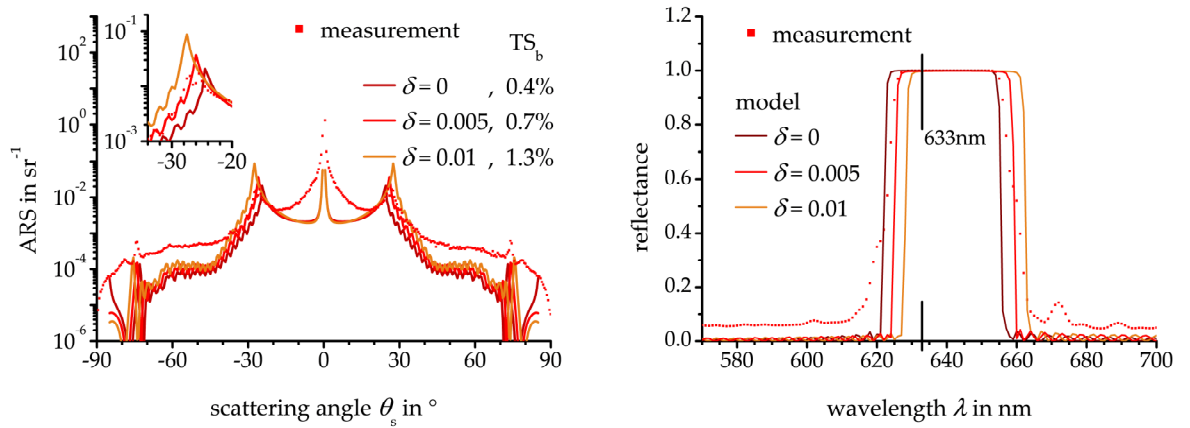


Fig. 6.18.: Influence of the optical thickness deviation δ on the ARS and TS_b (left, $\lambda=633$ nm, $\theta_i=0^\circ$, reflection hemisphere) and the reflectance spectrum (right, $\theta_i=6^\circ$). The best correlation between measured and modeled curves is achieved for $\delta=0.005$.

and demonstrates the connection between spectral properties and scattering losses.

The parameter δ affects in Eq. 3.7 only the optical factors \mathfrak{C}_i , which describe the transition of the incident field (θ_i) at the i -th interface to the scattered field (θ_s, φ_s) emerging from the i -th interface including interference and propagation conditions for both components through the multilayer system. Hence, the \mathfrak{C}_i correspond to merged field distributions for the angle of incidence as functions of the scattering angles and are closely related to the reflectance spectrum as a function of the incidence angle.

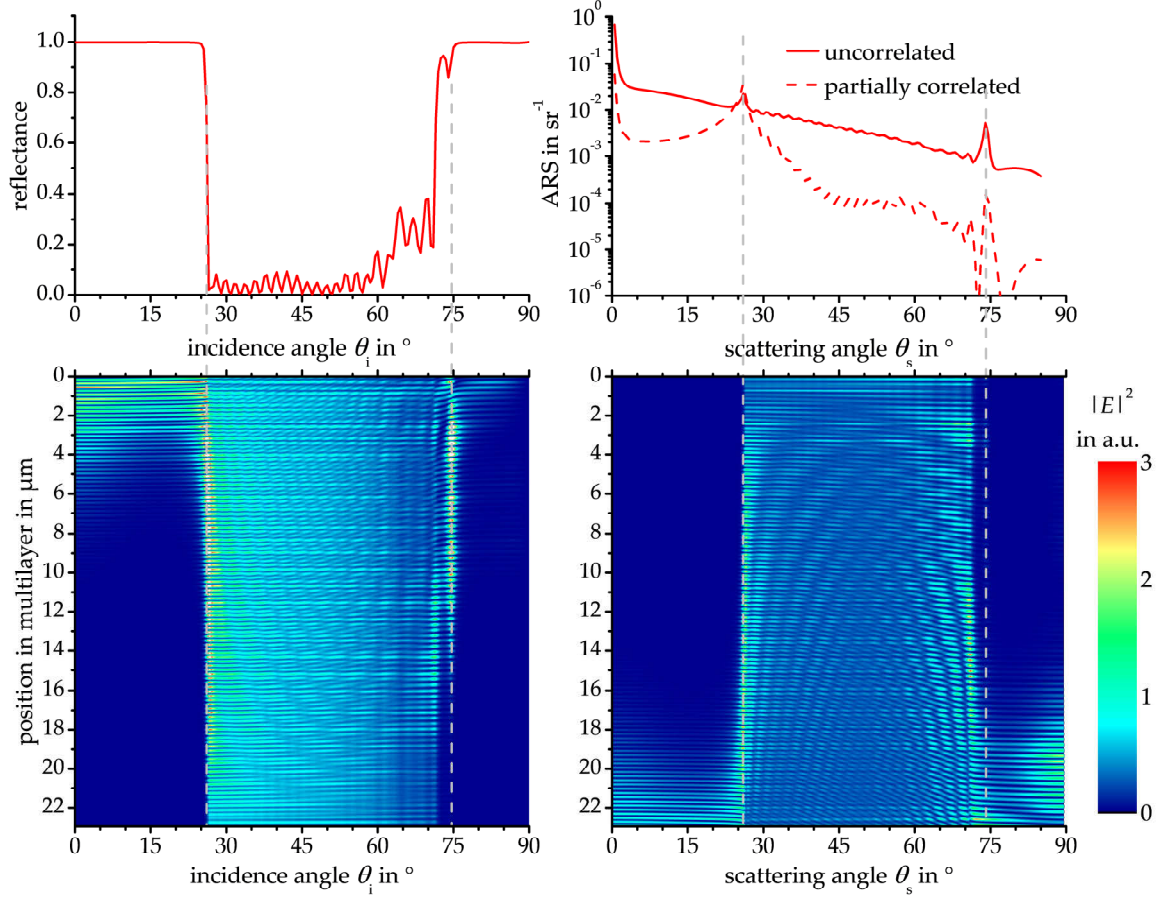


Fig. 6.19.: Standing wave field distributions in the multilayer stack as a function of θ_i for the incident (bottom left) and of θ_s for the scattered (bottom right) fields ($\lambda=633$ nm, s-pol). For comparison of peculiar angles, a modeled angular reflectance curve (top left) and a modeled ARS curve (top right) are given as well.

These relations are summarized in the diagrams in Fig. 6.19, that illustrate the standing wave field distributions within the notch filter for the illumination component ("ingoing field") and the scattered component ("outgoing field", toward the reflectance hemisphere) as functions of θ_i or θ_s , respectively. In addition, the angular reflectance spectrum as well as the ARS are depicted to demonstrate the correlation to the field distributions for selected angles. The figure reveals the following facts:

- The penetration depth into the multilayer at which the incident field for $\theta_i=0^\circ$ drops to $1/e^2$ is $4.6\text{ }\mu\text{m}$, which corresponds to 20% of the entire multilayer stack. Therefore, only the uppermost layers provide significant scattering contributions. This is a

consequence of the high reflectance for this illumination condition.

- Induced by the opposite "direction" of the outgoing scattered field in comparison to the incident field, the average penetration depths into the multilayer system can be assumed as inverted. This inverted behavior corresponds to the ability of the scattered field, generated at a specific interface, to escape from the multilayer system into the reflection hemisphere for a specific scattering angle.
- At angles that correspond to edges in the angular reflectance spectrum the field distributions of incident and scattered field reveal high penetration depths as well as high average field intensities.
- The improved abilities of the scattered light to leave the multilayer at these angles are responsible for the resonant scattering. (These effects can be enhanced or reduced by interface roughness correlation effects, as discussed in a following section.)

The intensity of the penetrating field at the single interfaces determines the contribution of an interface to the scattering distribution, whereas the field distribution of the scattered field determines if the scattered power can escape from the multilayer system. Consequently, the \mathfrak{C}_i can be assumed as the ability of the scattered light generated at the i -th interface to leave the multilayer, weighted by the incident field at the i -th interface for the current angle of incidence.

The weighting by the incident field is very impressive for conventional, highly reflective quarter wave stacks (Fig.6.20) for which primarily the roughness at interfaces from the high to the low index material (direction from air) contribute to scattering [132]. For the notch filter, there is no obvious correlation visible. However, for normal incidence at 633 nm, several interfaces correspond to field minima so that reduced scattering contributions can be expected [11]. Only at some of the uppermost interfaces maxima are located; therefore, considerable contributions to the scattering can be assumed. On the other hand, maxima are located in the thin film volumes. This implies that bulk scattering can be a significant scattering source, which is discussed in one of the following sections.

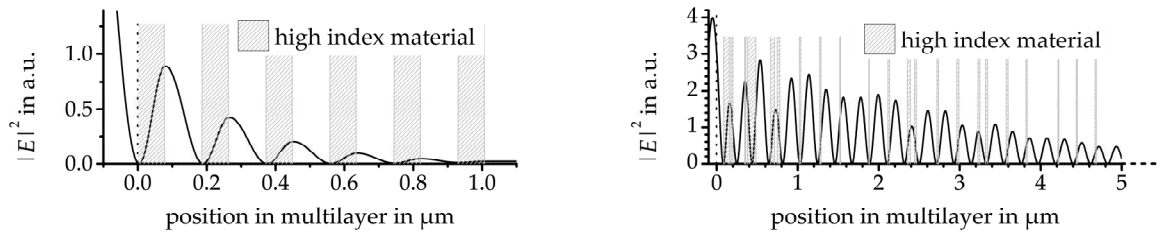


Fig. 6.20.: Comparison of the incident standing wave field distributions ($\theta_i=0^\circ$, $\lambda=633\text{ nm}$, s-pol) and the index steps for a highly reflective quarter wave system (left) and the notch filter (right). Abscissa origins correspond to the interfaces to air.

The angular reflectance spectrum is correlated to the spectral reflectance. A simple but rather coarse relation between pairs of illumination angles and illumination wavelengths can be derived from the Bragg equation (Eq.6.5, left) or from its generalized form for

multilayer systems (right part) [276,277] of period Λ and average refractive index n :

$$2\Lambda = \frac{\lambda_1}{\cos \theta_{i/s,1}} = \frac{\lambda_2}{\cos \theta_{i/s,2}} \quad , \quad \lambda = 2\Lambda \cos \theta_{i/s} \sqrt{1 - \frac{2(1 - \langle n \rangle)}{\cos^2 \theta_{i/s}}} \quad (6.5)$$

Although the equations give only the condition for constructive high reflectance for conventional periodical multilayer systems, they can be exploited to analyze the general correlation between pairs of λ and $\theta_{i/s}$. Both edges in the angular reflectance spectrum (26° and 74° , 633 nm) correspond for $\theta_i=0$ to edges in the wavelength spectrum at longer wavelengths. The resonant scattering as well as the edge in $R(\theta_i)$ at 26° belong to the edge of the reflectance band at 660 nm; the wing at 74° is related to a spectral section of high reflectance that starts at about 820 nm. With this knowledge, the positions of the resonant scattering wings can be evaluated to monitor the position of band edges.

For a narrow band notch filter, both band edges can be monitored, if the illumination wavelength is chosen short enough. For normal incidence at 532 nm, Eq. 6.5 predicts the resonant scattering at $\theta_s \approx 63^\circ$ and 73° , which correspond to the 623 nm and 660 nm band edges for normal incidence, respectively. As illustrated in Fig. 6.21 these results are only coarse estimations, but reveal qualitatively the correct behavior.

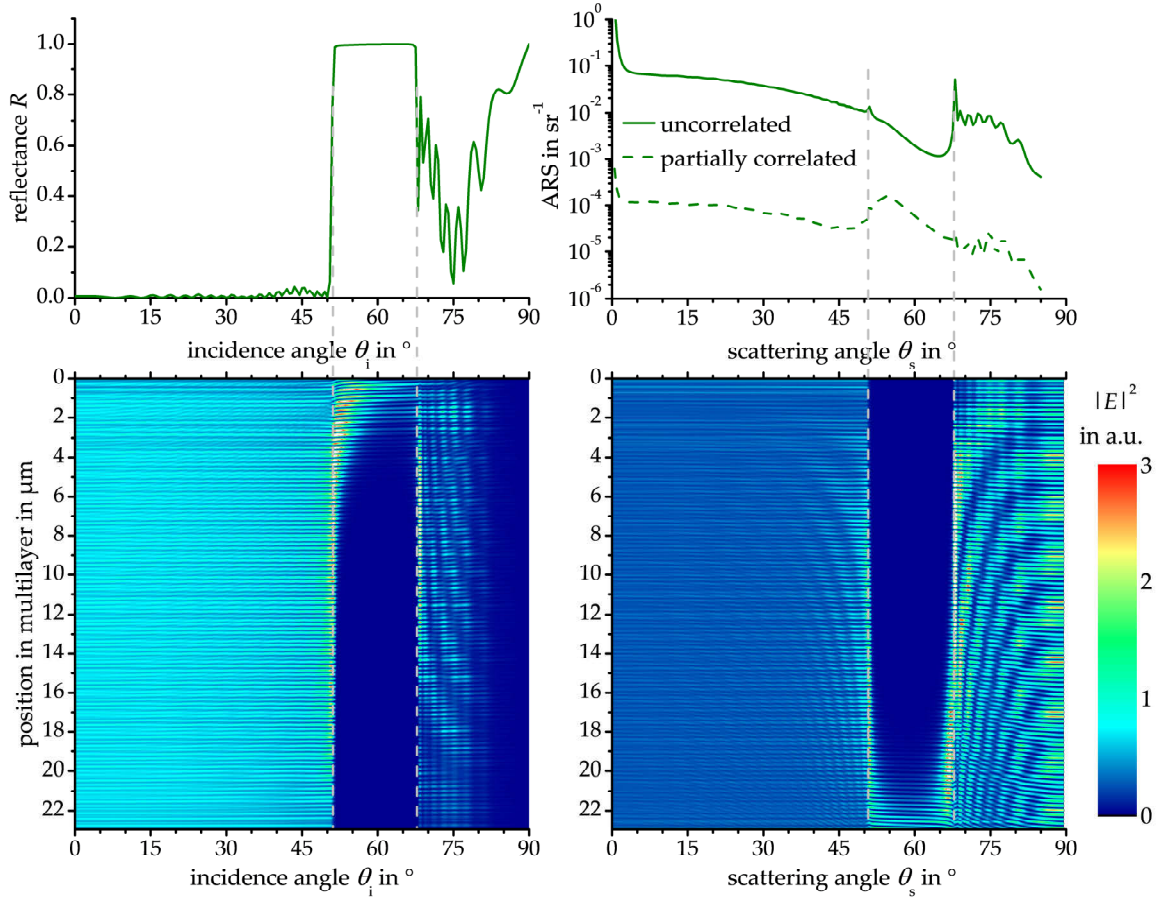


Fig. 6.21.: Standing wave field distributions in the multilayer stack as a function of θ_i for the incident (bottom left) and of θ_s for the scattered (bottom right) fields ($\lambda=532$ nm, s-pol). For comparison of peculiar angles, a modeled angular reflectance curve (top left) and a modeled ARS curve (top right) are given as well.

As a consequence of the transparency of the filter at 532 nm and the field distribution of the illumination component (Fig. 6.21), the penetration into the multilayer system is much higher than at 633 nm. Hence, the number of interfaces that can contribute to the scattering is increased. Otherwise, at scattering angles that correspond to the reflecting part of the spectrum, scattered light that emerges from deeper buried interfaces is not able to escape the multilayer into the backward hemisphere. Therefore, the light scattering at these angles for uncorrelated roughness is lower and is furthermore dominated by the uppermost interfaces. However, as also depicted, interference effects related to interface roughness correlation can dramatically reduce the average scattering level through destructive interference; hence, the scattering in the edge regions becomes a maximum.

These facts of the field distributions can be exploited for the further improvement of the roughness evolution and correlation models as will be pointed out.

Influence of roughness evolution

Although the evaluation of the spectral coefficient δ could improve the correlation between model and measurement for the resonant scattering wings, the general correlation, in particular for the illumination from the multilayer side, is still improvable. Therefore, the roughness evolution in the multilayer, which enters Eq. 3.7 by the PSD_{ii} (and PSD_{ij}) functions, is analyzed in the following paragraph.

Combined Master-PSD functions of the top surface and the substrate (rear side) were determined from WLI and AFM data (Fig. 6.22) to obtain an initial point for the roughness evolution modeling. These PSD functions revealed the progress typical for thin films on substrates (Secs. 3.2.2 and 6.2); hence, the combined evolution model could be applied to model the PSD functions of intermediate interfaces. The relevant roughness¹⁷ of the top surface and the substrate, determined from the Master-PSD functions, are $\sigma=2.9$ nm and $\sigma=0.34$ nm, respectively¹⁸.

Within the topography evaluation, particles on the substrate rear side were recognized that complicated the light scattering modeling process. However, the corresponding PSD functions, including the nano-particles, were also applicable for the scattering modeling (shot model, Sec. 3.1.3). The Master-PSD for the non-coated substrate was determined at particle free positions (small scan areas) and from PSD sections of the top surface that are not influenced by the intrinsic thin film roughness.

Roughness and PSD evolution models were successfully applied to describe the interface evolution of multilayers for light scattering modeling in several publications. For instance in [48,102,135,278] the kinetic continuum model was applied for highly reflective coatings for $\lambda=13.5$ nm; in [5,135] and [227] the empirical model was applied for highly reflective coatings for $\lambda=193$ nm and $\lambda=532$ nm, respectively¹⁹. However, to enable PSD models

¹⁷ Normal incidence at $\lambda=633$ nm ($f=0.014 \mu\text{m}^{-1} \dots 1.56 \mu\text{m}^{-1}$)

¹⁸ To achieve lower roughnesses, plasma assisted reactive magnetron sputtering is utilized by now.

¹⁹ [5], [48] and [227] are co-authored by the author of this thesis.

6. Light scattering properties of optical surfaces and thin films

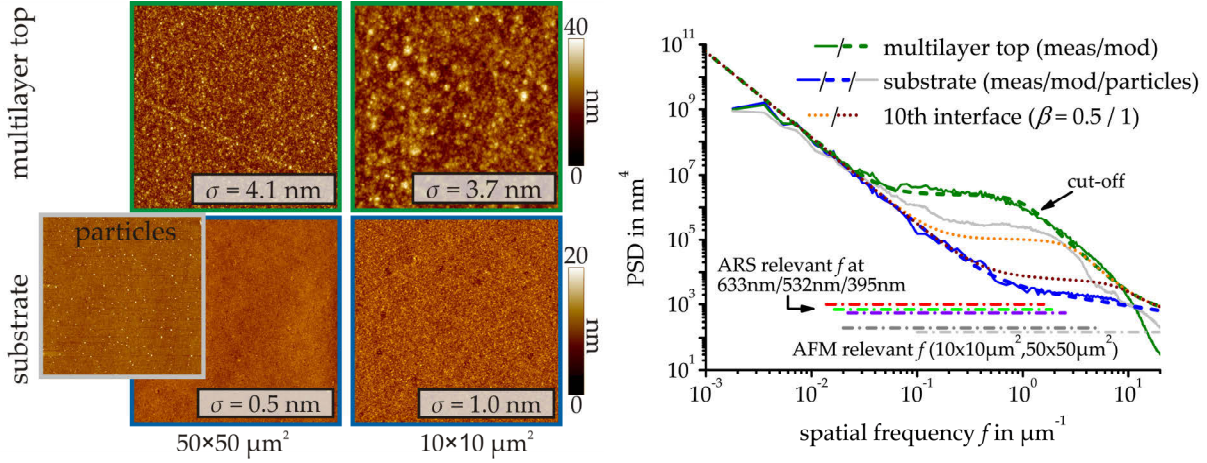


Fig. 6.22.: Master-PSD functions (right) obtained from WLI and AFM topography data (left). The model parameters are: $\Omega=0.72 \text{ nm}^3$, $\nu=0.7 \text{ nm}^2$, $\eta=3$, $\beta=0.75$, $K_1=676 \text{ nm}^{4-n_{K,1}}$, $n_{K,1}=1.65$, $K_2=2880 \text{ nm}^{4-n_{K,2}}$, $n_{K,2}=-0.5$.

that include a roughness evolution and a cut-off behavior according to arbitrary power laws, the combined model, introduced by the author in Sec. 3.2.2 and in [110], was applied for the notch filter. This was necessary, since the top surface PSD has the cut-off at spatial frequencies of $f \gtrsim 1.0 \mu\text{m}^{-1}$ that are relevant for the ARS at 633 nm and 395 nm at least at scattering angles $\theta_s \gtrsim 40^\circ$. Corresponding PSD functions of the 10th interface for $\beta=0.5$ and $\beta=1$ obtained with this model are exemplary illustrated in Fig. 6.22. In order to represent the correct substrate PSD, two fractal models were added: $\text{PSD}_{\text{sub}} = K_1/f^{n_{K,1}+1} + K_2/f^{n_{K,2}+1}$.

The roughness evolution power β could only be determined directly if surfaces from interrupted coatings processes would be analyzed or if destructive sample preparation for cross sectional measurements is applied [278]. To avoid this, β was determined indirectly in a fit procedure of measured and modeled ARS curves with the PSD functions of the top surface and the substrate as fixed input parameters. Fig. 6.23 shows results for different β and the corresponding measurement for the notch filter, if illuminated from the thin film or the substrate side.

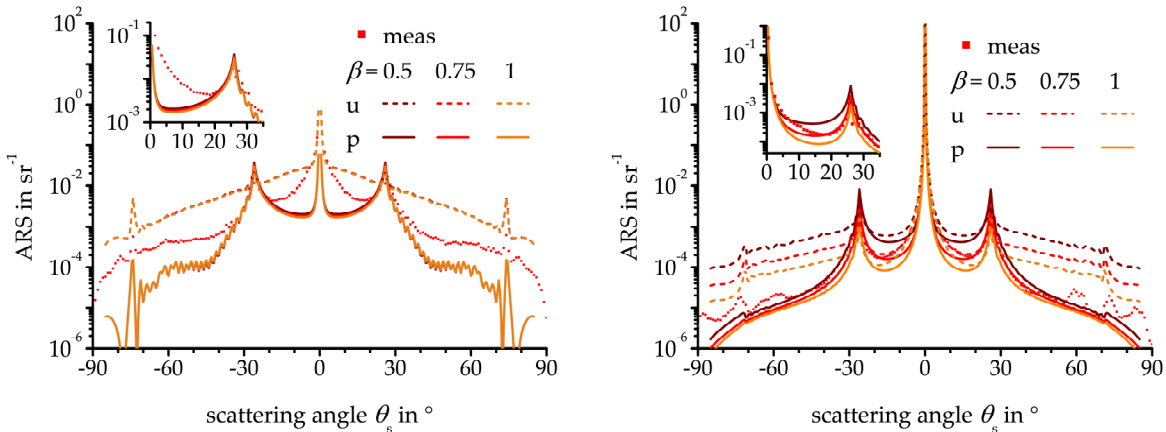


Fig. 6.23.: Influence of the roughness evolution parameter β on the ARS ($\lambda=633 \text{ nm}$, backward hemisphere) for illumination from the thin film (left) and from the substrate side (right).

The most concise relative alterations of the intrinsic PSD functions have to be expected

at the lowest interfaces in the stack, since the PSD model is additive. For example for $\beta=0.75$, the ratio of the first and second intrinsic film PSD is about 4.4; whereas it is only 1.005 for the uppermost interfaces. Consequently, as depicted in Fig. 6.23, the ARS with illumination from the substrate side reveals a higher sensitivity on the parameter β . This is additionally enhanced by the low penetration depth of the field. In the right hand side diagram in Fig. 6.23, the best correlation was obtained for partial correlation and for $\beta=0.75$, which corresponds to $\sigma \propto d^{0.75}$ for intrinsic film roughness evolution. Therefore, the roughness evolution (at least in the lower interfaces) is beyond the stochastic roughening regime.

Nonetheless, there was still a lack of correlation for illumination from the thin film side or for 532 nm, although the correlation of measurement and model for illumination from the substrate could be improved.

Influence of bulk imperfections

To explain remaining deviations between model and measurement, a model based on bulk scattering within the thin films [104], which had been applied by the author of this thesis to model the scattering of rugate coatings [110], was additionally tested. The motivation for this step were the high field intensities within the rather thick layers (Fig. 6.19, p. 74).

So far, the bulk imperfection PSDs are scaled versions of the surface PSD functions. However, the resulting curves for partially correlated and uncorrelated bulk inhomogeneities (Fig. 6.24) did neither improve the modeling results for 633 nm nor for 532 nm. The modeling results reveal considerable differences in the general shape of the ARS.

As described in [104], an intrinsic z -dependence of the bulk imperfections within the layer was additionally tested; Only with a high decay of the inhomogeneities along the z -axis, the results revealed a good correlation to the measurement. However, with this decay, the bulk scattering model reduces to partially or uncorrelated interface scattering. Hence, it is reasonable to negate significant influences of bulk imperfections on the ARS.

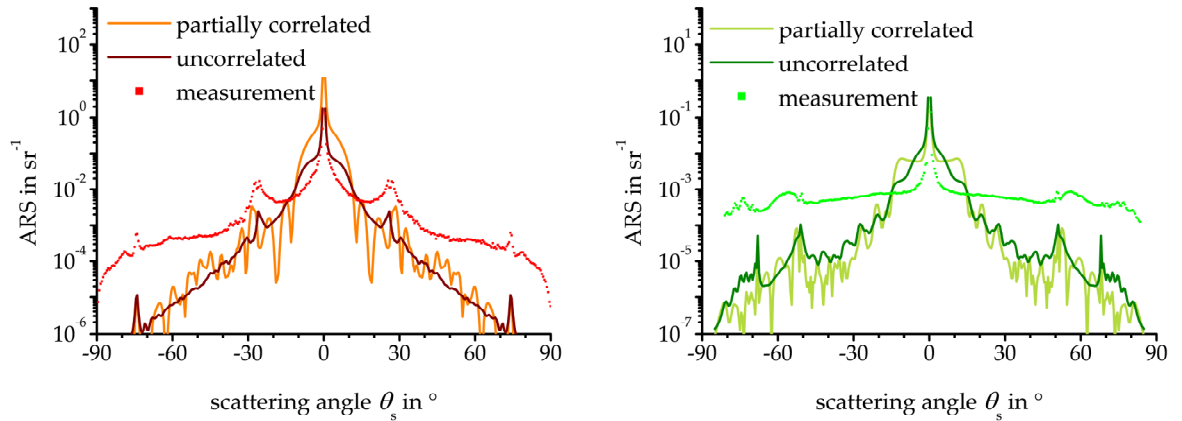


Fig. 6.24.: Attempts to improve the modeling based on correlated/uncorrelated thin film bulk scattering for $\lambda=633$ nm (left) and $\lambda=532$ nm (right).

Influence of interface roughness cross-correlation

By the modeling approaches presented up to now, only the ARS at 633 nm with illumination from the substrate shows a reasonable agreement; however, the interface cross-correlation properties were not discussed in detail so far. In the diagram on the left hand side in Fig. 6.23 the measured ARS curves are in between the partially and uncorrelated models. Therefore, the simplest approach - a weighted averaging - was tested and gives good results for 633 nm, normal incidence, and illumination from the thin film. This model implies the existence of partially correlated and uncorrelated interfaces within the illumination spot. In the context of Eq. 3.7, the averaging is the same as a factor $0 < \kappa < 1$ in front of the PSD_{ij} : $\text{PSD}_{ij} = \kappa \min(\text{PSD}_i, \text{PSD}_j)$, $i \neq j$.

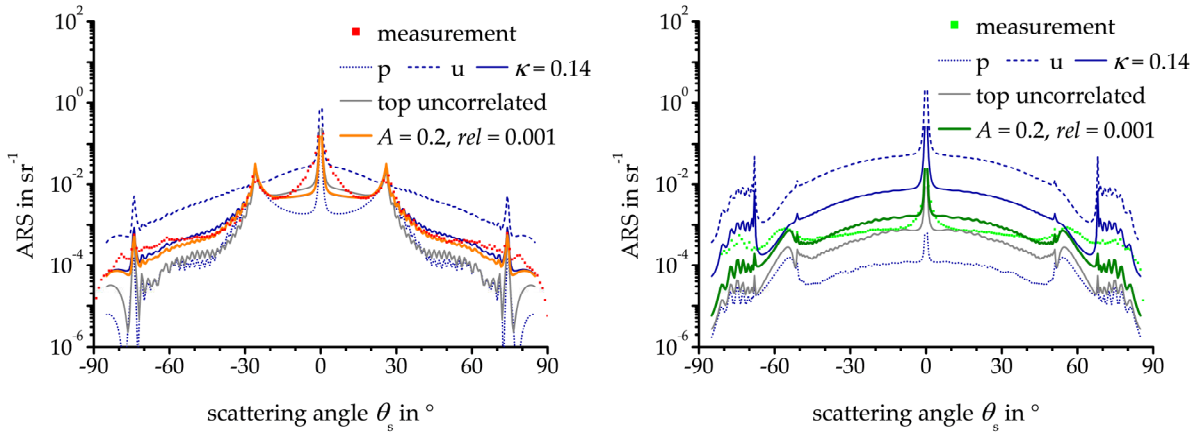


Fig. 6.25.: Comparison of measured and modeled ARS curves at 633 nm (left) and 532 nm (right) for different correlation models.

This proposed correlation model worked for normal incidence at 633 nm and 395 nm (not shown), but failed if the penetration depth into the multilayer is increasing for 532 nm or for higher incidence angles at 633 nm. Hence, the model was refuted. Otherwise, the good results of the partially correlated model for the illumination from the substrate side at 633 nm implied that the relevant effect were not apparent for deeper buried interfaces, but primarily in the uppermost interfaces.

If only the uppermost surface was assumed as uncorrelated with respect to the other partially correlated interfaces, a significant enhancement of the modeling quality for all wavelengths was achieved (Fig. 6.25). At 633 nm, in particular, the correlation close to the specular reflex is improved with these assumptions. This model can be interpreted as the influence of an external effect, not depending on the deposition or evolution process, which resulted in deviating cross-correlation properties of the uppermost interfaces.

To further improve this model an exponential weighting ansatz for the PSD_{ij} functions with a minimal degree of correlation at the top surface ($1-G$) and correlation relaxation τ_{vert} was investigated:

$$\text{PSD}_{ij} = \left(-G e^{-\tau_{\text{vert}} \times t} + 1 \right) \min(\text{PSD}_i, \text{PSD}_j) ; \quad (6.6)$$

here, t is the distance of the upper interface (i or j) to the uppermost (air-)interface.

With the parameter set ($G=0.02$, $\tau_{\text{vert}}=0.001 \text{ nm}^{-1}$) the best correlation was achieved for all investigated illumination conditions (Fig. 6.25). This implies a reduction of the partial correlation to a level of $(1-G/e)$ up to 1000 nm (4 %) into the thin film stack.

However, there are still unsolved remaining deviations. As long as the modeling assumptions have not been verified by independent analysis techniques, in particular the correlation model is only of theoretical nature. Nevertheless, recently presented methods for experimental cross-correlation measurements [136,137], which are either destructive or require an experimental effort that is beyond the scope of this work, could be applied to test the assumptions made.

6.3.2. Application scenarios for the light scattering sensor

The analyses presented and the light scattering model developed demonstrate the complex light scattering mechanisms in notch filter systems. In particular the necessity to perform several measurements at different illumination conditions to set up the scattering model seem to contradict the application of non-complex light scattering sensors. Nevertheless, once a comprehensive model is derived, sensor measurements can provide valuable information for the monitoring of interference filters.

The most relevant information is obtained if the analysis wavelength is close to the application wavelength and the sensor configuration emulates the application configuration. Therefore, a recently developed version of the scattering sensor concept for measurements in the transmission hemisphere [279] is modified and employed for test measurements. In addition, the application of the original sensor concept with little adaptations is tested.

The application scenarios, which are exemplarily demonstrated in the following, can cover different tasks in the notch filter quality assessment:

- monitoring the long wavelength band edge by evaluation of the angular position of the resonant scattering wing,
- monitoring of defects and contamination,
- assessment of the level of roughness evolution in the thin film stack,
- assessment of the ratio between blocking capability and scattering level, and
- monitoring the homogeneity of the mentioned properties over the entire surface.

Prior to the application tests, the application scenarios and the corresponding sensor configurations were analyzed employing the scattering model developed. Figure 6.26 shows modeled 3D-ARS distributions of the reflection hemisphere at $\lambda=633 \text{ nm}$ for $\theta_i=0^\circ$ and $\theta_i=18^\circ$, the illumination angle of the sensor, as well as in-plane ARS curves at $\theta_i=18^\circ$ for different (available) wavelengths close to 642 nm .

The left part of the figure reveals that the polar scattering angle of the resonant scattering ring is not a function of the incidence angle. This is in correspondence to the field

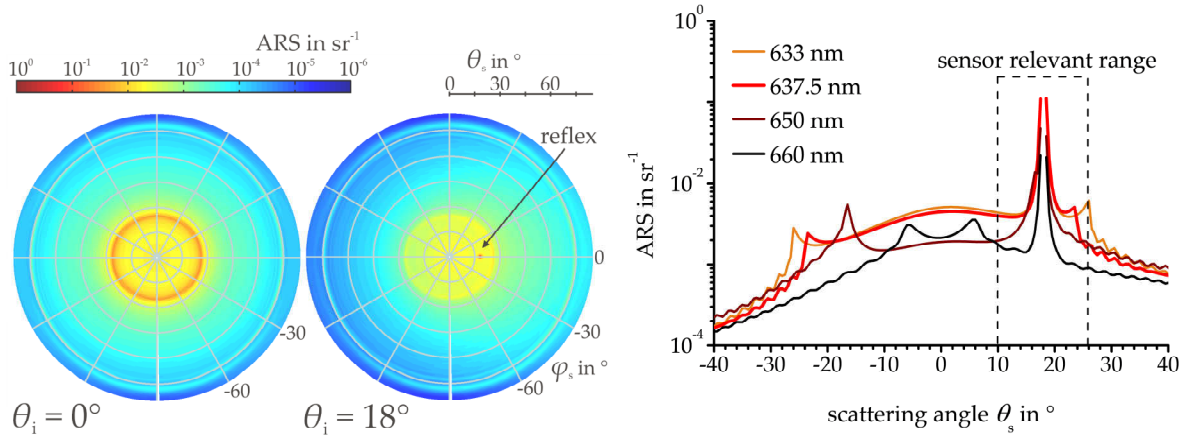


Fig. 6.26.: ARS modeling results to choose the illumination wavelength and the configuration of the light scattering sensor. The 3D-ARS of the reflection hemisphere for $\theta_i=0^\circ$ and $\theta_i=18^\circ$ (left) reveal constant angular positions of the ring of resonant scattering. In-plane ARS distributions demonstrate the optimal illumination wavelength (right).

distributions in Fig. 6.19 (p. 74), since the resonant scattering is caused by the interference effects in the scattered field component; therefore, the rings do not shift with the incidence angle. However, the corresponding ARS level is slightly changed as a result of the changing wave field distribution of the illumination field component and the shift of the scattering relevant spatial frequencies.

The right hand side diagram in Fig. 6.26 reveals that the resonant scattering angles are not within the covered scattering angles of the sensor in its standard configuration ($\lambda=660\text{ nm}$, $\theta_i=18^\circ$). Moreover, this illumination condition is not within the reflectance band of the notch filter. For 650 nm the resonant scattering shifts so that the specular reflex is almost collocated with the resonant scattering, since the illumination condition corresponds to the long wavelength spectral band edge. To separate the specular reflex and the resonant scattering within the angular range of the sensor, a laser diode emitting at 637.5 nm was implemented, for which the resonant scattering is located at $\theta_s=23.5^\circ$.

A comparison of a measured and a modeled h ARS obtained with this sensor configuration is illustrated in the left part of Fig. 6.27. Already these measurements enable the filters long wavelength band edge, its scattering loss in the reflectance hemisphere, for a configuration similar to the application conditions, as well as the homogeneity of the filter to be monitored.

For example, the inset on the left hand side of Fig. 6.27, indicates an increased scattering loss from $S=2.6 \times 10^{-4}$ to $S=6.0 \times 10^{-4}$, which is caused by a scratch and contamination on the filter surface. These types of peculiar scattering phenomena can be simply identified in 3D- h ARS distributions by anisotropy, fluctuations, or differences in the speckle structure, whereas it is hardly possible to discover them in in-plane ARS measurements.

The increased scattering is only visible for illumination from the thin-film side; therefore, the corresponding scattering sources are located in the uppermost layers. In addition, such defects are possible explanations for the remaining deviations close to the specular reflex (Fig 6.25, left) between ARS model and measurement and also for the necessity to

utilize modified roughness correlation model.

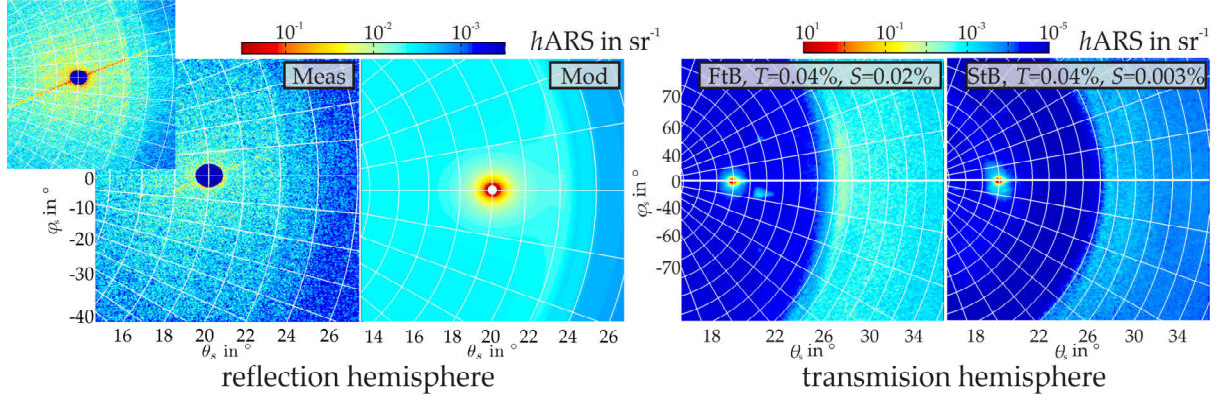


Fig. 6.27.: Left: Comparison of measured and a modeled $hARS$ distributions of the notch filter for the scattering sensor ($\lambda=637.5\text{ nm}$, $\theta_i=18^\circ$). The inset shows an $hARS$ disturbed by interface imperfections not typical for roughness. Right: $hARS$ distributions recorded in transmission with the thin film or the substrate towards the illuminating beam (FtB or StB) illustrate the advantageously reduced scattering for the StB orientation.

The high angular resolution of the sensor would enable the resonant scattering angle and, hence, the band edge to be determined with a high accuracy. For an uncertainty $\Delta\theta_s \approx 0.4^\circ$ for the angle of resonant scattering, the corresponding $\Delta\delta$ determined from ARS modeling is 0.001. This results in a sensitivity to shifts of the long wavelength band edge of as low as $\Delta\lambda \approx 0.7\text{ nm}$. This accuracy is only limited by the width of the resonant "ring" and the speckle structure, as visible in Fig. 6.27.

Another promising application scenario, demonstrated in the right part of Fig. 6.27, is a sensor which monitors the scattering as well as the blocking capability in the transmission hemisphere. The wavelength and the incidence angle are chosen to 637.5 nm and 10° , respectively, so that the angular distance between transmitted beam and resonant scattering is about 14° ; the sensor detector matrix is located in the transmission direction²⁰.

For this concept, the spectral properties, in particular the low transmittance, of the notch filter and the configuration in the transmittance direction have two advantageous effects on the measurement capabilities: on the one hand, integration of the specular part of the $hARS$ enables the transmitted power T to be measured; on the other hand, the beam dumping efforts for the sensor are reduced. The latter, in combination with the position of the CMOS-matrix in the transmittance hemisphere, enables a working distance of only 30 mm to be achieved. Hence, the solid angle covered by the sensor matrix is significantly increased to 0.28 sr (factor 3 compared to the standard configuration, p. 33), which corresponds to 4.4 % of $2\pi\text{ sr}$ of the hemisphere.

The evaluation of the scattering distributions obtained (Fig. 6.27, right) enables the analysis of both: the level of roughness evolution in the multilayer and the comparison of the ratio between the transmitted and the scattered power for illumination from the thin film or the substrate side. Although in this configuration the transmission is slightly higher

²⁰ A recently developed implementation of the light scattering sensor concept for ARS measurements in the transmission hemisphere described in [279] was modified for these experiments.

than for 642 nm and normal incidence, the ratios of $S/T \approx 0.50$ or $S/T \approx 0.07$ demonstrate impressively the reduced scattering loss for illumination from the substrate side, while the measured transmission levels (Fig. 6.27) remain constant.

From the light scattering model for pure partial correlation, the ratios of S for the two illumination conditions can be derived for different β (Fig 6.23). The results can then be compared to the measured ratios. High ratios indicate high differences between the roughness of interfaces close to the substrate and the roughness of the uppermost interfaces. Low differences indicate the absence of roughening, which is either achieved by negligible intrinsic thin film roughness or by replication of a dominating substrate roughness, for which the PSD functions in the multilayer stack are almost identical.

The evaluation of properties for arbitrary multilayer systems initially requires knowledge of the scattering model including roughness evolution and spectral properties. Thereafter, specific application scenarios can be analyzed. However, universal application scenarios of the scattering sensor for multilayer systems comprise at least homogeneity monitoring and defect assessment.

6.3.3. Concluding remarks

A comprehensive scattering model of a complex notch-filter multilayer system was derived by comparison of modeled ARS distributions to goniometer based ARS measurements at different illumination conditions. To adapt the light scattering model, a method which was developed previously [5,135] was taken, analyzed for the notch filter, and expanded.

The analysis of both, the roughness evolution and the field distributions within the multilayer stack, helped to explain the by more than one order of magnitude reduced scattering loss if the filter is illuminated from the substrate side. However, to bridge the remaining gaps between ARS measurement and modeling results, modeling approaches based on bulk scattering within the multilayer system and novel modified thin-film roughness correlation models were tested. In particular, a modified correlation model that indicates a loss of roughness correlation in the uppermost interfaces, could improve the correlation between modeled and measured ARS distributions.

The thorough light scattering model provided the basis for the development of tailored application scenarios of the light scattering sensor concept for the quality assessment of notch filters. Following modifications, indicated by the modeling, of illumination wavelength and incidence angle, the monitoring of the spectral properties in combination with the attenuation level, roughness evolution, and homogeneity were enabled.

6.4. Light scattering analysis and classification of surface defects

The conventional defect classification method presented in Sec. 5.2 is a visual "light scattering" inspection by trained persons. This is for commercial (fast, cost-effective classification) as well as historical reasons. For instance the scratch-dig standard, defined in the MIL-PRF-13830B [113] and based on a work from 1945 [280], is partially only a cosmetic standard [2,9] that defines the visibility of a defect. In particular for scratches, the reference charts aims on the visual impression of the scratches and, hence, the scratch classes are not necessarily correlated to the width/depth of the scratch [2,111,113,280].

ISO 10110-7 / ISO 14997 [8,112] as well as OP1.002 [114] attempt to avoid this problem by defining the defect classes through the flaw affected surface area. However, the primary part of defect assessment is still a "scattering" evaluation in which the visual impressions of the defects are compared to spots of defined areas on reference charts.

On the other hand, the scattering from defects and not the defect dimensions would result in performance limitations of optical elements. Hence, measurement and analysis of the ARS can provide additional quantitative means for defect assessment. This was already recognized by Young in the 80s [2,47]. He used scattering measurements and modeling to achieve the correct visual impressions (light scattering) for novel, improved reference defects that were congruent to the primary standards of the MIL standard.

In the following sections, approaches for an *h*ARS based defect assessment are presented. Besides the light scattering properties, the extraction of geometrical parameters for a conventional classification of defects, relevant in optical fabrication, is a main topic. This measurement task is well suited for the application of the light scattering sensor, since the scattering of defects reveals complex 3D-ARS distributions. It will be demonstrated that in particular the scattering close to the specular beam has to be analyzed and highly resolved measurements are necessary. Finally, a light scattering based approach for the defect classification according to ISO-10110-7 / OP1.002 is proposed and discussed.

6.4.1. Light scattering sensor qualification and applicability evaluation

The compact size enables the scattering sensor to be installed with other measurement systems in combined set-ups. For defect investigations, the sensor²¹ was combined with the WLI and a sample positioning stage to measure and compare defect topographies and *h*ARS distributions of the same surface positions (Fig. 6.28). After determination of the displacement, the real-time scattering or microscope images were observed while moving the sample to find defect affected surface positions.

In addition, the diameter of the sensor illumination spot was reduced to about 1 mm to expose the light scattering of single defects from the roughness induced scattering. A large illumination spot would result in an *h*ARS that is dominated by surface roughness,

²¹ Some defect results were obtained with a prototype sensor comprising a lens based beam preparation, $\lambda=650\text{ nm}$, $\theta_i=20^\circ$, and a Photonfocus MV1-D1024 CMOS matrix with 1024×1024 elements.

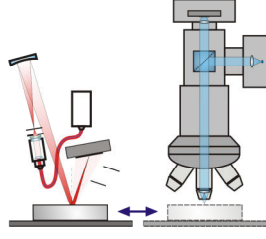


Fig. 6.28.: Combined set-up consisting of the scattering sensor (left), a white light interferometer (right), and an x/y -stage. The displacement was determined to observe the same sample positions.

since the ARS can be regarded as the average of rough surface and defect scattering, weighted by the corresponding illuminated areas. Thus, the scattering of small defects could vanish in the ARS distribution if the contributing defect (its scattering) is small compared to the illuminated surface area with pure roughness.

On the other hand, a rather small spot ($\lesssim 100 \mu\text{m}$) would increase the characteristic size of the speckle in the $h\text{ARS}$, which can interfere the scattering of the defect and would complicate the application of the evaluation procedures that will be discussed. Therefore, the spot size has to be a trade-off of the smallest defect size, that has to be identified, and the surface roughness. Moreover, the spot size determines the size of sampling steps and, hence, the measurement time for the mapping of an entire surface for defects.

To further illustrate these effects, the scattering of a small and shallow pit on differently rough metallic surfaces (fractal PSD, $n_K=1.3$, varying K) was modeled for different waists of the illumination spot ($2\omega_0$) with the BKT²². As a measure for the detection capability, the ratio \mathbb{R} of the integrated scattering for the defect on the rough surface and the pure rough surface was defined $\mathbb{R}=S_{\text{def}+\sigma}/S_\sigma$ and analyzed (Fig. 6.29). This definition is similar to a "signal-to-noise ratio" for defect detection with the scattering sensor.

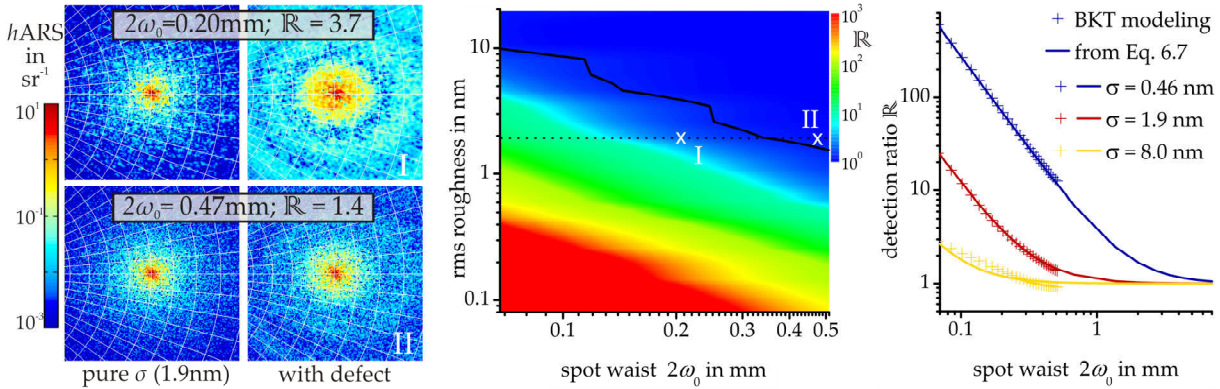


Fig. 6.29.: Sensitivity \mathbb{R} to detect a surface defect ($D=10 \mu\text{m}$, $t_0=0.8 \mu\text{m}$, elliptical depth profile) as a function of the illumination spot waists and the surrounding surface roughness. The black line (center) indicates the limit of $\mathbb{R}>2$. Left: Exemplary modeled ARS distributions to emphasize the varying speckle structure and the limit chosen.

In Fig. 6.29, the black solid line ($\mathbb{R}=2$) displays the threshold for which the pit is detectable in a measurement by analyzing S . In addition, exemplary $h\text{ARS}$ distributions close to the detection limit are given to illustrate $\mathbb{R}>2$.

²² Further BKT modeling results and a discussion concerning the applicability are presented in Sec. 6.4.3.

In the modeled ARS distributions (Fig.6.29, left), the scaling of the defect related scattering could be observed, whereas the roughness related scattering remained constant. A more detailed analysis of the modeled curves confirmed the following scaling relation for the detectability of a defect²³ in the sensor geometry:

$$\mathbb{R} = \frac{S_{\text{def}+\sigma}}{S_{\sigma}} \approx \frac{\frac{\mathbb{A}_{\text{def}}}{\mathbb{A}_{\text{spot}}} S_{\text{def}} + \frac{\mathbb{A}_{\text{spot}} - \mathbb{A}_{\text{def}}}{\mathbb{A}_{\text{spot}}} S_{\sigma}}{S_{\sigma}} \approx \frac{D_{\text{def}}^2}{S_{\sigma} 4 \omega_0^2} \left(\int \text{DSC} \, d\Omega + \left(\frac{4 \omega_0^2}{D_{\text{def}}^2} - 1 \right) S_{\sigma} \right) \stackrel{!}{>} 2 ; \quad (6.7)$$

\mathbb{A} are the respective surface areas; DSC is the differential scattering cross section which is applied in a few publications to describe and compare the scattering from singular sources such as defects or particles. DSC and ARS are related by a normalization with the spot area or better with the illumination beam profile [55,62,115,281]. However, the quantity is inappropriate for measurement purposes for several reasons: Following the definition in [55,115] the determination of DSC requires an excellent knowledge about the illumination spot. Nevertheless, DSC would be still affected by the surrounding roughness²⁴. Thus, the DSC is almost not accessible in a light scattering measurement and is, therefore, not applied in this thesis. Otherwise, the same arguments reveal that in a strict interpretation "the ARS of a defect" does not exist, since the entire illuminated area, even if it is perfectly smooth, has to be taken into account.

Modeled and extrapolated curves obtained from Eq. 6.7 are additionally given in the right hand side diagram of Fig.6.29. These curves enable the chance to detect defects for a given spot diameter to be determined from an estimated DSC and an estimated S_{σ} . Using the equivalent beam energy for a top hat profile with a spot diameter $D_{\text{spot}}=1$ mm, the sensor in the chosen set-up should be applicable to detect defects with the given dimension up to a relevant roughness levels of about 1 nm.

6.4.2. Angle resolved scattering and topographies of surface defects

With the combined set-up of the WLI and the scattering sensor, the h ARS distributions and topographies of peculiar positions on a titanium thin film, a silicon surface, and a RG1000 glass substrate were analyzed. Fig.6.30 compares the topographies and the h ARS results of selected defects: a scratch in and a particle on the RG1000 substrate, an elliptical dig in the silicon surface, as well as a stretched dig in the titanium thin film.

The scratch topography (Fig. 6.30, A), which is a result of a manual sample preparation with a scratch tool (tip radius: 250 μm , force: 0.5 N), reveals a depth of only 25 nm and a width of 18.5 μm . The corresponding h ARS shows an increased scattering ($\mathbb{R}=5.4$) with a pronounced level perpendicular to the scratch direction caused by diffraction at the

²³ The first approximation is not straightforward and only valid in an ergodic sense, since cross-correlation properties of the defect and the roughness have to be considered. In the context of the VPT, these cross-correlation properties correspond to mix terms in the PSD calculation of roughness and defect topography sections. However, the influence of these terms is reduced if $\mathbb{A}_{\text{def}}/\mathbb{A}_{\text{spot}} \ll 1$.

²⁴ In general the determination of a DSC unaffected by the surrounding surface roughness would require the illumination spot to be adjusted to the defect size. A reasonable approximation can only be achieved if the defect scattering is considerably dominating.

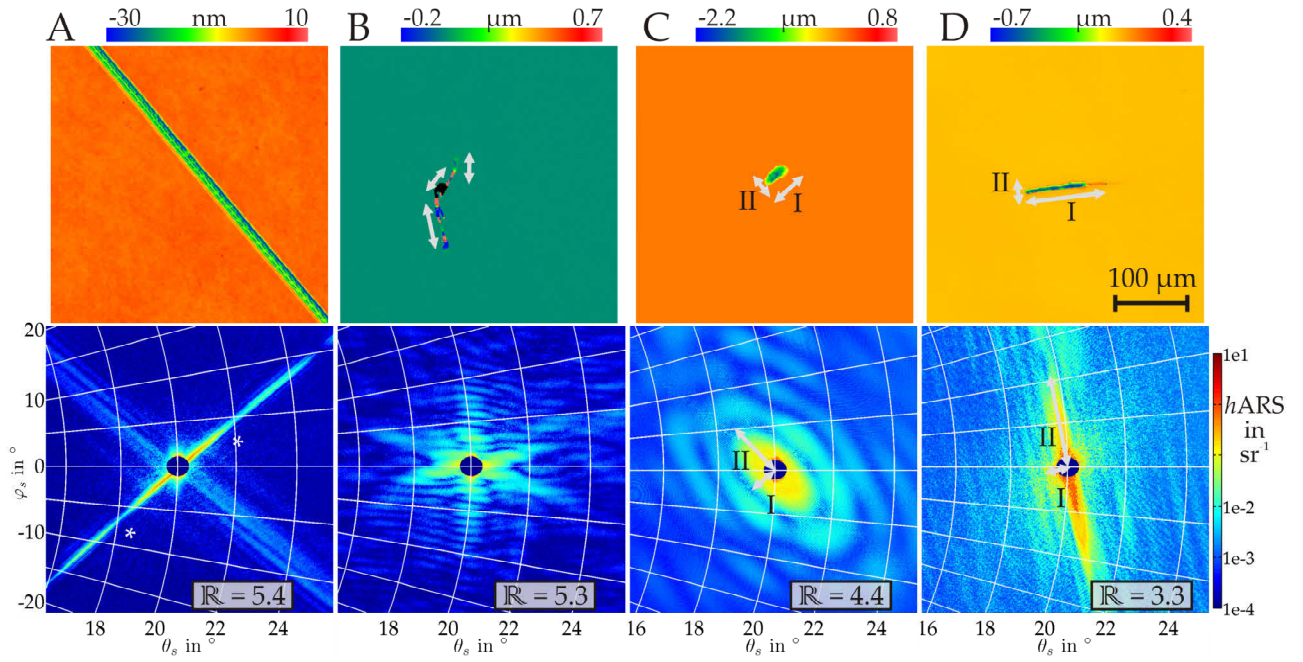


Fig. 6.30.: Comparison of $hARS$ measurements to the corresponding topography data (WLI, $10\times$ objective, $370\times 370\mu m^2$) and \mathbb{R} values. Left to right: scratch in RG1000 surface, particle on RG1000 surface, pit in silicon surface, and pit in 200 nm thick titanium film. (Orientations of the $hARS$ and topography data are congruent.)

scratch edges. In addition, there is a second increased scattering level almost parallel to the scratch, which is caused by a non-periodic corrugated structure within the scratch. This structure corresponds to chatter marks of the scratch tool, similar to those on the SPDT surfaces in Sec. 6.1.1 and similar to that mentioned for scratches in [237].

The pronounced anisotropic scattering distribution of scratches - for this scratch is $\mathbb{D}_{|\text{mean-med}|}=0.28$ ²⁵ - can be exploited to distinguish scratches and other defects in an automated surface mapping, if the anisotropy properties of the scratch are significantly different from that of the roughness. In addition, the scratch width (Tab. 6.3) is determinable with Eq. 3.8 by evaluating θ_1^{\min} of the constrictions in the increased scattering (label *).

The surface feature in Fig. 6.30, B is presumably a particle contamination. Although the corresponding topography profile exhibits invalid data points, dimension of about $130\times 35\mu m^2$ are readable for this object, which shows similarity to a textile fiber fragment. The corresponding $hARS$ reveals a very complex distribution with several minima and maxima. Nevertheless, the three primarily visible directions of the particle, labeled in the surface topography, can be identified in the $hARS$ distribution. Moreover, the $hARS$ reveals an increased scattering of $\mathbb{R}=5.3$ compared to a defect free position.

The elliptical form of the pit (Fig. 6.30, C) with a depth of about $1.6\mu m$ causes an $hARS$ distribution similar to an Airy pattern. According to Eq. 3.8 and congruent to basic diffraction theory, the dimensions of the ellipse (the first minima in the $hARS$) are inverted with respect to the major and minor axes visible in the topography data (I and

²⁵ $\hat{\sigma}_{\text{std}}=0.64$, $PV_{\text{ACF},\hat{\sigma}}=0.56$; anisotropy parameter definitions on page 55.

II). This inverted behavior is even more impressive for the defect in Fig. 6.30, D.

Besides the increased scattering, the characteristic fine structures of the defect ARS distributions are impressive. Employing Eq. 3.8, the dimensions of the axes of both pits and the scratch were estimated from the h ARS and compared to those determined at the defect top and at the defect FWHM (Tab. 6.3). In addition, the h ARS as well as the topography (Fig. 6.31) of two artificial chromium humps on a defect reference chart²⁶ are evaluated to test the evaluation procedure for flaws which are no indentations.

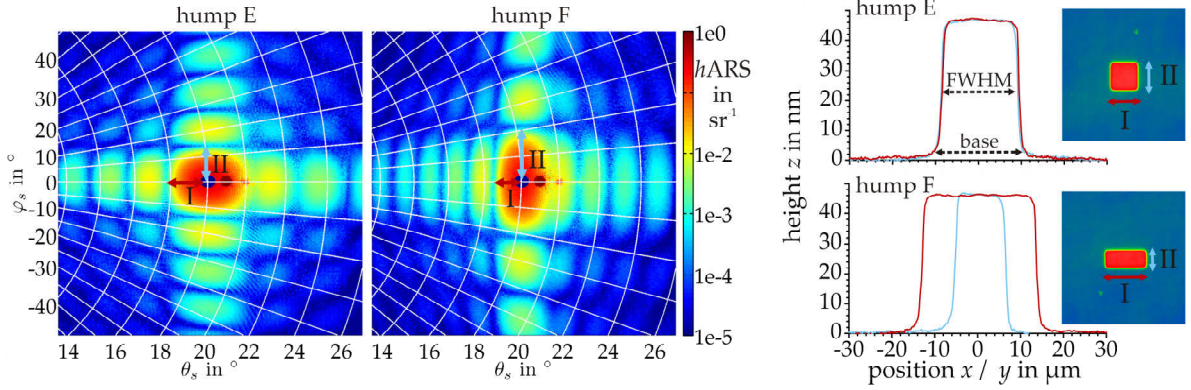


Fig. 6.31.: Measured h ARS distributions (left) and corresponding topography data (right) of two chromium spots of the ISO 10110-7 defect class 0.016 on a defect reference chart.

Tab. 6.3.: Defect dimensions (major and minor axes) obtained from h ARS and from topography data at the defect base and at the FWHM.

	scratch A	pit C		pit D		hump E		hump F	
		maj I	min II	maj I	min II	AI	AII	maj I	min II
θ_1^{\min} in $^\circ$	2.75	1.05	2.3	0.4	4.1	2.3	2.3	1.5	3.5
D_{hARS} in μm	16.5	43.3	19.8	113.6	11.1	19.8	19.8	30.3	13.2
D_{WLI} , base, in μm	18.5	40.9	20.6	88.4	12.5	20.0	20.0	28.6	14.0
D_{WLI} , FWHM, in μm	12.0	29.6	13.6	79.0	6.0	17.8	18.0	26.6	11.9

In Tab. 6.3, the better correlation of the dimensions obtained from the h ARS to the dimensions at the top/base of the flaw compared to those at the FWHM is mentionable. Hence, in correspondence to the requirements of the defect classification standards, the results from the h ARS distributions represent the affected area. Although there is a good correlation of the axes dimension determined from h ARS, the reliability of this procedure in the case of general pits and humps has to be cross-checked. Therefore, additional modeling results and the evaluation of an increased experimental database are presented in the next section.

By applying Eq. 3.8 it is straightforward to estimate the minimal and maximal analyzable defect sizes for the current sensor configuration, which correspond to axes dimensions from $154 \mu\text{m}$ ($\theta_1^{\min}=0.3^\circ$) down to less than $5.8 \mu\text{m}$ ($\theta_1^{\min}=8^\circ$).

²⁶ The reference chart was provided by Hellma Optik, Jena.

6.4.3. Light scattering modeling to classify defects

So far, the exemplary results revealed the potential for a thorough defect assessment using the light scattering sensor. In this section the general applicability of Eq. 3.8 for the sensor based classification of pits and scratches of arbitrary forms and depths regarding ISO 14997 and OP1.002 is further addressed. Therefore, the scattering of different defects is modeled for the sensor set-up with the BKT (Sec. 3.1.1).

First of all the applicability of the BKT for this task has to be tested. For example, the radii of local surface curvatures, which should be much larger than λ for the validity of the tangent plane approximation (Eq. 3.5), are at least higher than $10\text{ }\mu\text{m}$ ²⁷ for both pits in Fig. 6.30. However, the tangent plane requirement could be fulfilled better, in particular with regard to the local surface normals at the defect edges (cosine term in Eq. 3.5), and since the analyzed surfaces are not perfectly conducting. Therefore, measured and modeled $h\text{ARS}$ distributions are compared to verify the applicability of the BKT (Fig. 6.32). This comparison was enabled by the combined WLI-sensor set-up that provided the required pairs of $h\text{ARS}$ and topography data as input for the modeling.

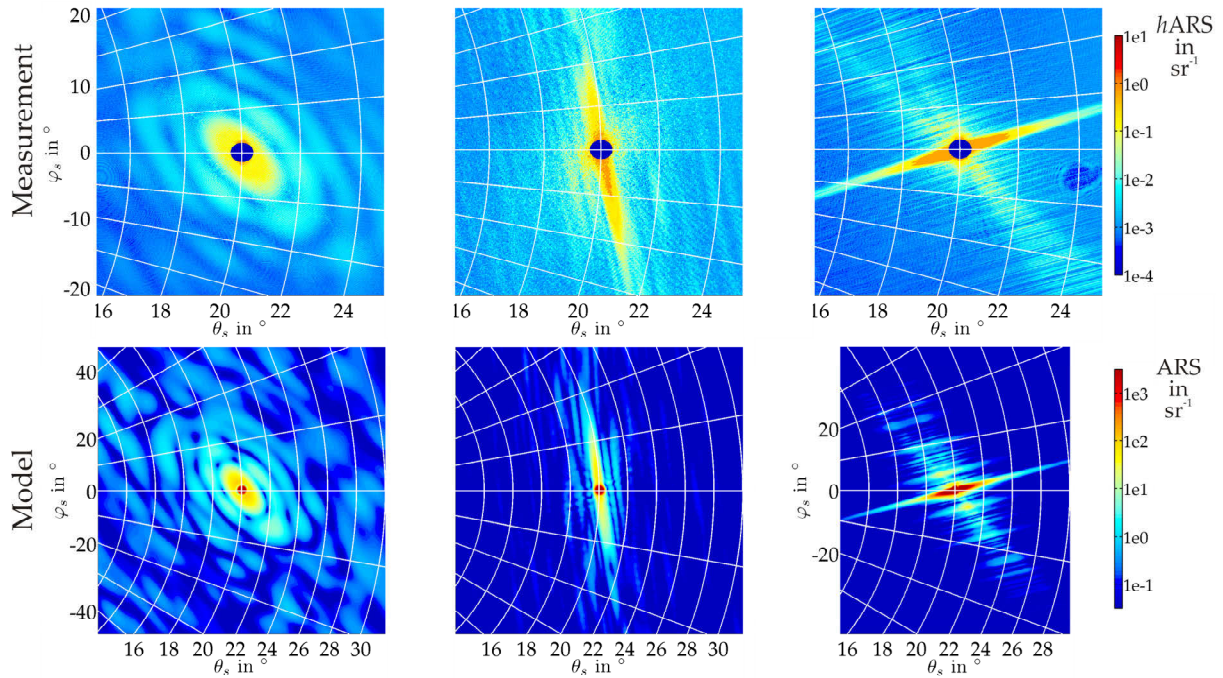


Fig. 6.32.: Comparison of measured and modeled $h\text{ARS}$ distributions of the pits C and D (left, center) from Fig. 6.30 and a further scratch in a silicon surface (right). The modeling results were obtained with the BKT using the corresponding topography data as input.

The modeling results in Fig. 6.32 show a very good correlation to the measurements, although the defects were assumed as ideal reflectors ($F=-1$, s-polarized illumination). Deviations in the global level are attributed to the differences in the spot sizes and beam profiles between modeling and measurement (see Sec. 6.4.1 and Eq. 6.7): the dimensions of the complete topography profile were $698 \times 523\text{ }\mu\text{m}^2$; therefore, this area was illuminated by

²⁷ The curvature radius r_c was obtained as the reciprocal value of the local mean curvatures.

a plane wave with a Gaussian amplitude profile with a waist diameter of only $2\omega_0=114\mu\text{m}$ in the modeling. This profile should suppress the diffraction at the edges of the modeling area.

A comparison of only the beam properties (sensor: $1000\mu\text{m}$ diameter, tophat profile; modeling: $66.6\mu\text{m}$ FWHM, Gaussian profile) revealed a scaling factor of about 460 between measurement and modeling results. This factor would considerably reduce the deviations in the average $h\text{ARS}$ level (shift of color scale by $\log_{10} 460 \approx 2.7$).

The spot size in the modeling was limited by two factors: computer memory and WLI scan area. However, increasing the WLI measurement area by applying a lower magnification would additionally limit the resolution of the topography data, which is in particular critical at the pit edges. Nevertheless, the correlation for the three different defects is remarkable.

In addition, the application of the rigorous Finite Difference Time Domain method (FDTD²⁸) as well as of the shot model (Sec.3.1.3) were tested (Fig.6.33). The FDTD modeling result reveals similarities to the measurement or the BKT result only for the general symmetry of the turning points in the $h\text{ARS}$ (label *). The deviations are presumably caused by the reduced simulation volume ($64 \times 64 \times 4\mu\text{m}^3$), necessary to fit the limited memory (32 GB) of the desktop computer for the grid discretization applied. As a consequence, the waist of the Gaussian illumination beam was only $2\omega_0=24\mu\text{m}$, which was too small for a homogeneous illumination of the defect. Moreover, the diffraction of the Gaussian beam shadows sections of the defect scattering close to the specular reflex.

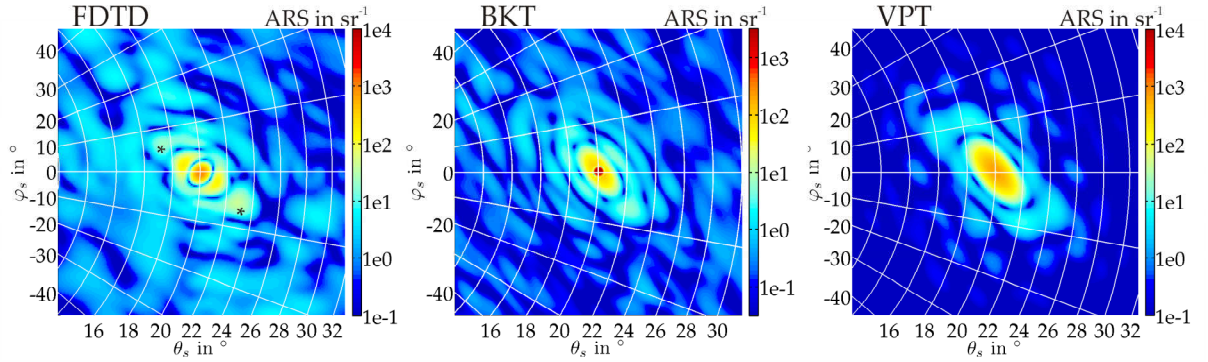


Fig. 6.33.: Modeled $h\text{ARS}$ distributions of the pit C (Figs.6.32 and 6.30) obtained with the FDTD, the BKT, and the VPT method (from left to right). Although the scales are different, the corresponding color scale widths are 5 decades.

The result obtained with the shot model reveals significantly less similarity to the measured $h\text{ARS}$ than the FDTD result. In particular, the poor agreement of the symmetry is evident. At scattering angles beyond the first minimum as well as on the perimeter of the first maximum from the reflex, the correlation of the BKT result is obviously better. It should be mentioned, that the VPT would always predict point symmetric scattering distributions, since, despite minor asymmetries in the optical factor, the PSD function is per definition symmetric.

²⁸ Software: FDTD Solutions (Lumerical Solutions, Inc.) with grid precision 2.

With dimensions of $40.9 \times 20.6 \times 1.6 \mu\text{m}^3$ the defect depth is beyond the validity of the smooth surface approximation. Hence, deviations of the shot model are not surprising. Despite the detailed discrepancies, the positions of the first minima are similar in both models, which is an additional hint for the applicability of Eq. 3.8 to arbitrary defects.

Because of the good correlation between $h\text{ARS}$ model and measurement, the BKT should be suited to investigate the applicability and the limitations of Eq. 3.8 to pits that are not within the smooth surface limitations required by the shot model. Figure 6.34 shows exemplary modeled ARS results in the sensor geometry for circular pits ($D=20 \mu\text{m}$) with varying depths z_0 and edge slope powers m whose topographies are defined by:

$$z(x, y) = -z_0 \left(1 - (2/D)^2 (x^2 + y^2)\right)^{1/m}. \quad (6.8)$$

For an easier comparison, only the in-plane ARS curves ($\varphi=0^\circ$) are plotted to show the variations of the first minima, $\theta_s^{1,\min} = [1.9^\circ, 3.1^\circ]$. The diagrams reveal that the ARS is considerably more altered by the defect depth, whereas the form has less effect. A similar result was stated in [19] for the influence of the particle form on the corresponding ARS distributions.

From the first minima in the modeled ARS, the surface defect diameters were determined and compared to the diameters at the top as well as the FWHM of the pits. The results are summarized the tables in Fig. 6.34, that reveal a maximal uncertainty interval $D = [16.2 \mu\text{m}, 25.2 \mu\text{m}]$. Similar to the experimental results in Sec. 6.4.2, the modeling emphasizes that the correlation to the upper diameter, in particular for low m , is better than at the FWHM. This is somehow surprising, since the average (vertical) phase differences should be close to the FWHM. On the other hand, typical defects are much wider than deep and, hence, the laterally induced phase deviations should provide the highest effect.

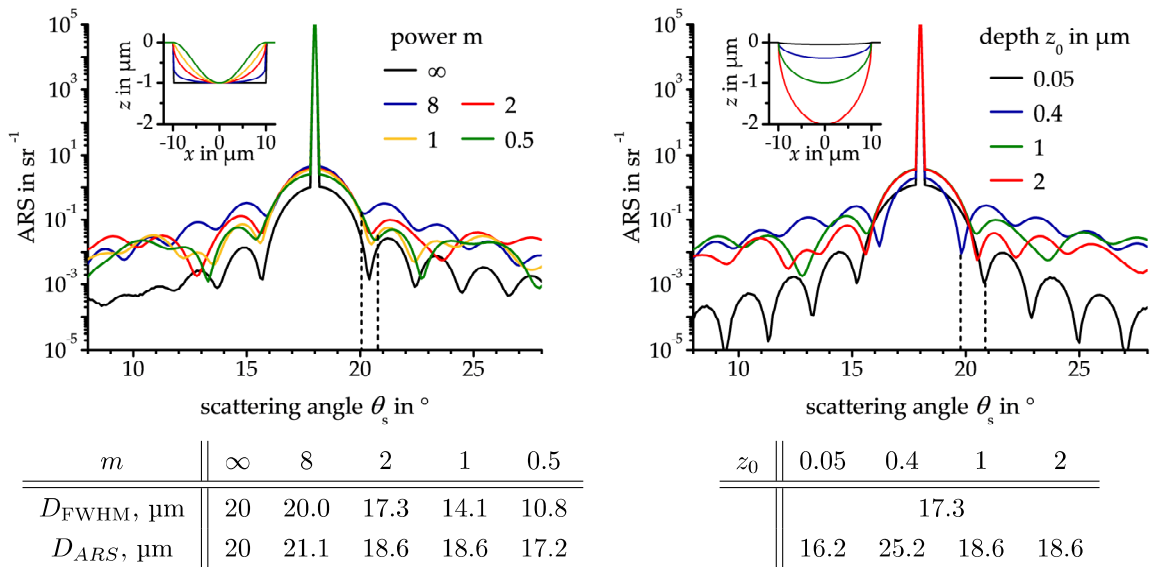


Fig. 6.34.: Exemplary modeling results for a pit ($D=20 \mu\text{m}$) with different edge profiles ($m=2, 4, 8, \infty$; $z_0=1 \mu\text{m}$; left) and different depths ($z_0=0.05 \mu\text{m}, 0.4 \mu\text{m}, 1 \mu\text{m}, 2 \mu\text{m}$; $m=2$; right).

In a modeling with finer steps of z_0 , the highest deviations for the defect diameter correspond to depths for which the first minima almost completely vanish. These are depths close to $z_0 = \frac{N}{2} \frac{\lambda}{\cos \theta_i}$ for the cylindrical pits. For these depths, "global destructive interferences" with local minima of S as a function of z_0 are observed. For ellipsoidal pits, a shift of these interference conditions to higher depths and a reduction of the destructive interference effects occur. Hence, vanishing minima are of reduced concern for non-cylindrical pits.

The statistical evaluation of additional modeling result for (symmetrical) model pits of varying diameters is summarized in Fig. 6.35 (left) to set up a broader data base for the deviations that have to be expected in the determination of defect dimensions. For each box plot given, 200 pits were modeled with depths ranging from 50 nm to 10 μm and profile powers of 0.5, 1, 2, 4, and 8. The box plots reveal that for 80 % (whiskers) of the modeled pits the deviations of the input and the measured diameter do not exceed 22 %.

In addition, the accuracy of the estimation for the base diameter as well as the diameter at the FWHM was analyzed from this database. For $\frac{2}{3}$ of the modeled pits, the correlation is better for the dimensions at the defect base. If only the lower powers $m=0.5, 1, 2$ - which are assumed to be more reliable representations of real world defects - are taken into account, this ratio is even improved to $\frac{5}{6}$. Consequently, in the following investigations the pit diameters were determined at the upper edges in the topography data. Fortunately, these diameters are relevant dimensions for the defect classification according to ISO 10110-7 or OP1.002.

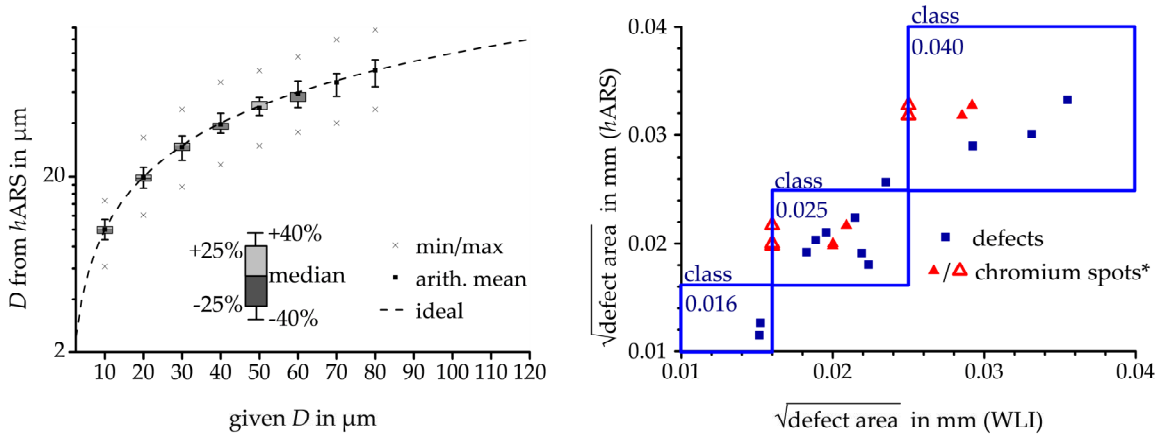


Fig. 6.35.: Left: Box plots summarize expectable deviations for the proposed measurement procedure if applied for pits with the same diameter, but different geometries and depths. Right: Comparison of defect classification results based on WLI topography data and $h\text{ARS}$ evaluation for 12 defects on RG1000, titanium, and silicon surfaces as well as five chromium spots on the reference chart. *) compared to WLI data or the nominal defect classes (solid/open triangles).

The modeling results reveal basic impressions of scattering based defect classification. However, typical defects are neither symmetric, nor do they provide analytical edge profiles. Nevertheless, the uncertainties obtained from the modeling are similar to that of further surface flaws, which were identified and analyzed by means of the combined WLI/sensor set-up.

In the right hand side diagram of Fig. 6.35, defect areas determined from WLI and h ARS are compared and categorized according to ISO 10110-7. Therefore, the minor and major axes were determined at the defect base and the area of a corresponding ellipse was calculated.

Furthermore, the artificial rectangular defects on the classification chart were analyzed as well. For the chromium spots, the classes were overestimated by one class. This misassignment is explainable, since the defects on the reference chart represents the upper bound of the corresponding class. Therefore, small deviations of the axes result in an overestimation of the corresponding defect. On the other hand, a closer look at the defect profiles (Fig. 6.31) reveals that the top of the hump edge (even if the round corners of the defect area are included) are closer related to the stated defect class than the base dimensions, which light scattering is sensitive for. Thus, the classification deviations are more related to deviations of the chromium spots than to uncertainties in the determination of the axes itself.

6.4.4. Concluding remarks

The light scattering based assessment of defects on optical surfaces was theoretically discussed and experimentally demonstrated for measurements with the scattering sensor. In this context, the influences of the substrate roughness and the illumination spot diameter on the sensitivity of defect detection were analyzed and a procedure to adjust the sensitivity was proposed. In addition, the applicability of the BKT to surface defect modeling was experimentally verified by comparison of h ARS modeling and measurement results. This was, in particular, enabled by the topography and scattering data obtained with a combined set-up of the WLI and the scattering sensor.

The basis for the derived defect assessment procedure is the validity of a simple relation between the defect dimensions and the minima in the light scattering distributions, which was analyzed and discussed. Experiments and BKT modeling results revealed an uncertainty in the order of 22 % for the dimensions obtained from the h ARS distributions for arbitrary formed defects. In addition to the defect dimensions, an impression of the relevant optical disturbance induced by the flaw is directly and very fast accessible with the light scattering sensor.

The results presented, set up the base for a thorough defect characterization methodology. Therefore, the surface is scanned and the h ARS at each surface position is evaluated for S , \mathbb{R} , and anisotropy to identify defects and scratches. Image processing routines should be applicable to obtain the shape of the first minimum curve in the h ARS from which the covered surface areas according to ISO 10110-7 / OP1.002 can be determined.

7. Summary

Light scattering based characterization techniques provide advantages which should be exploited for the characterization of optical components. These benefits are, on the one hand, technical aspects such as the non-contact measurement approach, the robustness which is induced by the insensitivity to vibrations, and the potential for fast measurements. On the other hand, scattered light contains valuable information, which is worth to be exploited by advanced light scattering analysis to gather information about its origins and, hence, about the imperfections on optical surfaces in general.

However, the application of light scattering techniques for the quality assessment in optical fabrication processes is still at the beginning, although the techniques provide the advantages mentioned. Therefore, methodologies for the evaluation of optical surfaces were developed in this thesis, which combine tailored measurement, analysis, and modeling techniques with a compact and flexible scattering sensor, developed in the course of this thesis as well. This framework provides an extremely high potential for in-line applications as compared to conventional surface grading techniques or other (semiconductor matrix based) approaches for angle resolved scattering measurements. Hence, the system constitutes the first light scattering based sensor device which is sensitive enough for the quality assessment of optical surfaces with in-line capability. Moreover, a basis was created "to make inexpensive, fast, accurate scattering measurements available in a variety of situations where location, or expense, has prevented it in the past." [J. C. Stover, 31]

The sensor system allows calibrated, angle resolved scattering distributions in a cone of about 9° around the specular beam in the reflection hemisphere to be recorded. Including the near angular limit of 0.3° , this angular range covers a spatial frequency bandwidth of one and a half decade of roughness information. Although this bandwidth is below the more than two decades bandwidth of atomic force microscopy (AFM) or white light interferometry (WLI), it was demonstrated that the obtained roughness data is less influenced by artifacts to which these topography measurements techniques are prone.

The dynamic range of more than 7 decades and the sensitivity down to scattering levels below $5 \times 10^{-5} \text{ sr}^{-1}$ enable surfaces with rms roughness values as low as 0.3 nm to be characterized. This sensitivity was never achieved before by other sensor-like systems. Moreover, the analysis of the uncertainty budget revealed a combined uncertainty of only 5% for roughness values obtained from the sensor measurements. Besides the evaluation of the uncertainty budget, the validity conditions of the vector perturbation theory (VPT) including the inherent far-field properties were analyzed for the specifics of the scattering sensor. The results revealed an upper roughness level of approximately 30 nm

as limit for the application of the VPT for roughness measurement. Thereby, the far field requirements are ensured by the imaging element in the beam preparation system even for a compact sensor configuration with a plane, oblique detector matrix.

The light scattering sensor enabled the extended anisotropy and roughness analysis of surfaces fabricated by diamond turning and different polishing processes. In this context, a novel methodology for the evaluation of directional roughness values determined from 3D angle resolved scattering (ARS) distributions and for the derivation of isotropy parameters was developed and analyzed. This methodology made it possible (i) to analyze and model roughness components of surfaces fabricated by single-point diamond turning with different feed parameters; (ii) to compare the anisotropy properties of diamond turned surfaces and an anisotropically polished cylindrical lens; and (iii) to optimize magnetorheological finishing (MRF) processes. In particular for the evaluation of the MRF process, the fast close-to-process, almost in-situ, measurements provided by the scattering sensor could be exploited to find optimal finishing parameters for the removal of diamond turning marks. In addition, the sensitivity of the MRF process to the relative orientation between MRF processing and turning mark direction was detected by analyzing the roughness and isotropy properties of an entire surface with the sensor.

The extension of the spatial frequency range for roughness measurements with the scattering sensor to two decades ($f \lesssim 0.015 \mu\text{m}^{-1}$ to $1.5 \mu\text{m}^{-1}$) was achieved by the implementation of a second illumination channel and the application of roughness spectra model functions. Conventionally, a stochastically reliable roughness value in a similar bandwidth is only achievable through combination of measurement results obtained from WLI and AFM. The extended measurement and analysis capabilities enabled the study of the roughness evolution of differently thick titanium films. In addition, the substrate induced anisotropy properties were evaluated to define a transition frequency at which thin film roughness would become critical for the optical losses of coated substrates.

A model to describe the angle resolved scattering of a complex notch-filter multilayer system was derived for the first time by comparison of modeled ARS distributions to ARS distributions measured with a goniometer system at different illumination conditions. Therefore, previously derived modeling approaches for highly reflective multilayer systems [5,135] were taken, analyzed, and expanded for the notch filter.

A scattering loss reduction of an order of magnitude was observed if the filter was illuminated from the substrate side. The analysis of both, the roughness evolution and the field distributions in the multilayer stack enabled the explanation of reduced scattering losses. To bridge remaining gaps between the ARS measurement and modeling results, approaches based on a model for thin film bulk scattering and novel, modified thin film roughness correlation models were investigated. However, only a modified correlation model, which indicates a loss of roughness correlation in the uppermost interfaces, could improve the correlation of modeled and measured scattering distributions.

The modeling results provided the basis for the development of scattering sensor ap-

plication scenarios for the quality assessment of notch filters. For example, modifications of the illumination wavelength and the incidence angle were indicated to enable the monitoring of spectral properties in combination with the attenuation, the key performance parameter of the notch filter.

The assessment of digs, scratches, and other defects on optical surfaces using the scattering sensor was theoretically and experimentally demonstrated. In this context, the influences of the substrate roughness and the illumination spot diameter on the sensitivity of defect detection were analyzed and a procedure to adjust the sensor sensitivity was proposed. The basis for the derived defect grading procedure is a relation between the diameter of cylindrical pits in surfaces and the (first) minima in light scattering distributions, whose validity was analyzed and discussed for arbitrary defect geometries. Experiments and Beckmann-Kirchhoff theory (BKT) modeling results revealed an uncertainty of about 22 % for the lateral dimensions of arbitrary formed defects determined from ARS measurements with the scattering sensor. In addition to the defect dimensions, quantitative descriptions of the disturbing optical effects induced by the imperfections are received from the light scattering measurements.

Moreover, the general applicability of the BKT for the modeling of surface defects was experimentally verified by comparison of modeled and measured ARS results. This was enabled by analyzing topography and scattering data that were obtained with a combined set-up of a WLI and the scattering sensor.

The investigation results for the structural properties and the imperfections of optical surfaces presented, demonstrate the opportunities that are enabled by profound scattering analysis methods even for an easy to handle and compact light scattering sensor. This diversity of in-dept investigation scenarios opened up for and by the utilization of the sensor exceeds the state of the art in investigations of such physical effects.

However, possible future work should be dedicated for instance to the implementation of further illumination channels, which enable the coverage of an extended spatial frequency range without the necessity of interpolation, or to the test of novel sensor matrices of a next generation (e.g. sCMOS [200]) to increase the sensitivity. This would, for example, enable the characterization of ultra-smooth mirror substrates designed for application in extreme ultra violet lithography [278].

In order to apply the sensor for the characterization of optical components prior to polishing, the structure-scattering-relationships for ground surfaces would need further investigation. For example, the evaluation of the speckle structure in the ARS [180, 282] could bridge the gap of invertible structure-scattering-relationships between smooth surfaces and rough engineering surfaces. Another promising extension of the scattering sensor concept would be the implementation of polarization sensitive matrix elements [283] to enable the application of a analysis method for subsurface damage [49], which was developed recently with collaboration of the author of this thesis.

Bibliography

- [1] B. J. Griffiths, R. H. Middleton, and B. A. Wilkie, “Light scattering for the measurement of surface finish: a review,” *International Journal of Production Research* **32**, 2683–2694 (1994).
- [2] M. Young, “Scratch-and-dig standard revisited,” *Appl. Opt.* **25**, 1922 (1986).
- [3] L. Feinberg, “Space telescope design considerations,” *Opt. Eng.* **51**, 011006 (2012).
- [4] J. E. Harvey, “Parametric analysis of the effect of scattered light upon the modulation transfer function,” *Opt. Eng.* **52**, 073110–1–12 (2013).
- [5] S. Schröder, T. Herffurth, H. Blaschke, and A. Duparré, “Angle-resolved scattering: an effective method for characterizing thin-film coatings,” *Appl. Opt.* **50**, C164–C171 (2011).
- [6] A. J. Cormier, “Assessment of current scratch standards,” *Proc. SPIE* **805**, 152–159 (1987).
- [7] D. M. Aikens, “Meaningful surface roughness and quality tolerances,” *Proc. SPIE* **7652**, 765217–1–7 (2010).
- [8] “Optics and photonics - test methods for surface imperfections of optical elements,” (ISO 14997:2011) (2011).
- [9] D. M. Aikens, “The truth about scratch and dig,” in “International Optical Design Conference and Optical Fabrication and Testing , OSA Technical Digest (CD),” (2010), pp. 10–12.
- [10] L. R. Baker, “Inspection of surface flaws by comparator microscopy,” *Appl. Opt.* **27**, 4620–4625 (1988).
- [11] A. von Finck, T. Herffurth, S. Schröder, A. Duparré, and S. Sinzinger, “Characterization of optical coatings using a multisource table-top scatterometer,” *Appl. Opt.* **53**, A259–A269 (2014).
- [12] F. D. Orazio Jr., W. K. Stowell, and R. M. Silva, “Instrumentation of a variable angle scatterometer (VAS),” *Proc. SPIE* **362**, 165–171 (1983).
- [13] J. Rifkin, K. A. Klicker, D. R. Bjork, D. R. Cheever, T. F. Schiff, J. C. Stover, F. M. Cady, D. J. Wilson, P. D. Chausse, and K. H. Kirchner, “Design review of a complete angle scatter instrument,” *Proc. SPIE* **1036**, 116–124 (1988).
- [14] F. M. Cady, M. W. Knighton, D. R. Cheever, B. D. Swimley, T. L. Huntldoff, T. F. Schiff, and M. E. Southwood, “A design review of a broadband, three-dimensional scatterometer,” *Proc. SPIE* **1753**, 148–157 (1992).
- [15] C. Amra, D. Torricini, and P. Roche, “Multiwavelength (0.45–10.6 μm) angle-resolved scatterometer or how to extend the optical window,” *Appl. Opt.* **32**, 5462–5474 (1993).
- [16] T. A. Germer and C. C. Asmail, “Goniometric optical scatter instrument for out-of-plane ellipsometry measurements,” *Rev. Sci. Instrum.* **70**, 3688 (1999).
- [17] T. V. Vorburger, E. C. Teague, F. E. Scire, M. J. Mclay, and D. E. Gilsinn, “Surface roughness studies with DALLAS-detector array for laser light angular scattering,” *Journal of Research of the National Bureau of Standards* **89**, 3–16 (1984).

- [18] M. Gebhardt, H. Truckenbrodt, and B. Harnisch, "Surface defect detection and classification with light scattering," *Proc. SPIE* **1500**, 135–143 (1991).
- [19] T. A. Germer, "Multidetector hemispherical polarized optical scattering instrument," *Proc. SPIE* **3784**, 304–313 (1999).
- [20] P. Kadkhoda, W. Sakiew, S. Günster, and D. Ristau, "Fast total scattering facility for 2D inspection of optical and functional surfaces," *Proc. SPIE* **7389**, 73890S–1–8 (2009).
- [21] E. L. Church, H. A. Jenkinson, and J. M. Zavada, "Measurement of the finish of diamond-turned metal surfaces by differential light scattering," *Opt. Eng.* **16**, 360–374 (1977).
- [22] J. Ohtsubo, "Measurement of diamond-turned metal surfaces by light scattering," *Proc. SPIE* **558**, 80–84 (1985).
- [23] Y. Y. Fan and V. M. Huynh, "Light scattering from periodic rough cylindrical surfaces," *Appl. Opt.* **32**, 3452–8 (1993).
- [24] C. Métayer, V. A. Sterligov, A. Meunier, G. Bossis, J. Persello, and S. V. Svechnikov, "Field induced structures and phase separation in electrorheological and magnetorheological colloidal suspensions," *J. Phys.: Condens. Matter* **16**, S3975–S3986 (2004).
- [25] S. Holler, Y. L. Pan, R. K. Chang, J. R. Bottiger, S. C. Hill, and D. B. Hillis, "Two-dimensional angular optical scattering for the characterization of airborne microparticles," *Opt. Lett.* **23**, 1489–91 (1998).
- [26] G. E. Fernandes, Y.-L. Pan, R. K. Chang, K. Aptowicz, and R. G. Pinnick, "Simultaneous forward- and backward-hemisphere elastic-light-scattering patterns of respirable-size aerosols," *Opt. Lett.* **31**, 3034–6 (2006).
- [27] Datasheet Optis GmbH, "OMS 2," <http://www.optis-world.com/products/hardware/OMS.html> (2013-11-14).
- [28] D. Hueser, T. Rinder, and H. Rothe, "Comparison of PSD measurements using stray light sensors with PSD curves evaluated from topography of large AFM scans," *Proc. SPIE* **3426**, 262–272 (1998).
- [29] V. A. Sterligov, E. V. Shun'ko, I. O. Grytsaienko, and L. V. Poperenko, "Fabrication and properties of ITO films treated by excited atomic oxygen," *Appl. Opt.* **51**, 1997–2003 (2012).
- [30] R. Brodmann, O. Gerstorfer, and G. Thurn, "Optical roughness measuring instrument for fine-machined surfaces," *Opt. Eng.* **24**, 408–413 (1985).
- [31] J. C. Stover, V. Skurdal, J. Bender, and P. D. Chausse, "Design review of a hand-held scatterometer," *Proc. SPIE* **1331**, 195–200 (1990).
- [32] J. C. Stover, J. A. Bender, M. L. Bernt, D. L. Bjork, P. D. Chausse, D. R. Cheever, K. Kirchner, and T. F. Schiff, "Modular scatterometer with interchangeable scanning heads," (WO1992000514A1, 1990).
- [33] E. Kawate and M. Hain, "Scatterometer basing on a STAR GEM idea for optical measurements of microlenses," *Proc. SPIE* **8495**, 84950M–1–10 (2012).
- [34] J. C. Stover and E. Hegstrom, "Scatter metrology of photovoltaic textured surfaces," *Proc. SPIE* **7771**, 777109–1–7 (2010).
- [35] Datasheet Light Tec, "Mini-Diff - 3D (hemispheric) scatterometer," http://www.lighttec.fr/applicnotes/Brochure_MiniDiff_March13.pdf (2014-05-05).
- [36] R. Yeo, R. Rykowski, D. Kreysar, and K. Chittim, "The imaging sphere - the first appear-

- ance meter?" Proc. of The 5th Oxford Conference on Spectroscopy pp. 87–103 (2006).
- [37] C. Hahlweg and H. Rothe, "Design of a full-hemispherical spectro-radiometer with high dynamic range for characterization of surface properties using multi-spectral BRDF data from VIS to NIR," Proc. SPIE **5965**, 596519–1–13 (2005).
 - [38] O. G. Rodriguez-Herrera, M. Rosete-Aguilar, and N. C. Bruce, "Scatterometer of visible light for 2D rough surfaces," Rev. Sci. Instrum. **75**, 4820 (2004).
 - [39] A. Okamoto, H. Kuniyasu, and T. Hattori, "Detection of 30-40 nm particles on bulk-silicon and SOI wafers using deep UV laser scattering," **19**, 372–380 (2006).
 - [40] Datasheet KLA-Tencor Corporation, "Candela CS20 - Optical Surface Analyzer," <http://www.kla-tencor.com/compound-semiconductor-manufacturing/candela-cs20.html>.
 - [41] S. Rice, "Reflection of electromagnetic waves from slightly rough surfaces," Commun. Pure Appl. Math. **4**, 353–378 (1951).
 - [42] H. Davies, "The reflection of electromagnetic waves from a rough surface," Proceedings of the IEE-Part IV: Institution Monographs **101**, 209–214 (1954).
 - [43] P. Beckmann, "Scattering by composite rough surfaces," Proc. IEEE **53**, 1012–1015 (1965).
 - [44] E. L. Church and J. M. Zavada, "Residual surface roughness of diamond-turned optics," Appl. Opt. **14**, 1788–95 (1975).
 - [45] A. A. Maradudin and D. L. Mills, "Scattering and absorption of electromagnetic radiation by a semi-infinite medium in the presence of surface roughness," Physical Review B **11**, 1392–1415 (1975).
 - [46] R. Young, "Low-scatter mirror degradation by particle contamination," Opt. Eng. **15**, 516–520 (1976).
 - [47] M. Young, "Objective measurement and characterization of scratch standards," Proc. SPIE **362**, 86–92 (1983).
 - [48] S. Schröder, T. Herffurth, M. Trost, and A. Duparré, "Angle-resolved scattering and reflectance of extreme-ultraviolet multilayer coatings: measurement and analysis," Appl. Opt. **49**, 1503–12 (2010).
 - [49] M. Trost, T. Herffurth, D. Schmitz, S. Schröder, A. Duparré, and A. Tünnermann, "Evaluation of subsurface damage by light scattering techniques," Appl. Opt. **52**, 6579–88 (2013).
 - [50] H. Truckenbrodt, A. Duparré, and U. Schumann, "Roughness and defect characterization of optical surfaces by light-scattering measurements," Proc. SPIE **1781**, 139–151 (1992).
 - [51] T. A. Germer and C. C. Asmail, "Polarization of light scattered by microrough surfaces and subsurface defects," J. Opt. Soc. Am. A **16**, 1326 (1999).
 - [52] S. Maure, G. Albrand, and C. Amra, "Low-level scattering and localized defects," Appl. Opt. **35**, 5573–5582 (1996).
 - [53] A. Duparré, "Light scattering techniques for the inspection of microcomponents and microstructures," in "Optical inspection of microsystems," W. Osten, ed. (Taylor & Francis, Boca Raton, 2007), pp. 103–119.
 - [54] A. Duparré, "Scattering from surfaces and thin films," in "Encyclopedia of modern optics," R. D. Guenther, ed. (Elsevier Academic Press, Amsterdam, 2004), pp. 314–321.
 - [55] J. C. Stover, "SCATTEROMETERS," in "Handbook of Optics II, Part 3," M. Bass, ed. (McGraw-Hill, New York, 1995), chap. 26, pp. 26.1–16, 2nd ed.
 - [56] F. E. Nicodemus, "Directional reflectance and emissivity of an opaque surface," Appl. Opt.

- 4, 767 (1965).
- [57] “Standard practice for goniometric optical scatter measurements,” (ASTM E2387-05) (2011).
 - [58] “Guide for angle resolved optical scatter measurements on specular or diffuse surfaces,” (SEMI ME1392-1109) (2009).
 - [59] J. C. Stover, *Optical Scattering: Measurement and Analysis* (SPIE-Press, Bellingham, WA, 1995), 2nd ed.
 - [60] “Optics and optical instruments - test methods for radiation scattered by optical components,” (ISO 13696:2002) (2002).
 - [61] J. M. Bennett, “Recent developments in surface roughness characterization,” *Meas. Sci. Technol.* **3**, 1119–1127 (1992).
 - [62] J. C. Stover, *Optical Scattering: Measurement and Analysis* (SPIE-Press, Bellingham, WA, 2012), 3rd ed.
 - [63] A. Duparré, J. Ferre-Borrull, S. Gliech, G. Notni, J. Steinert, and J. M. Bennett, “Surface characterization techniques for determining the root-mean-square roughness and power spectral densities of optical components,” *Appl. Opt.* **41**, 154–171 (2002).
 - [64] “Surface texture (surface roughness, waviness, and lay),” (ASME B46.1-2002) (2003).
 - [65] P. Nayak, “Random process model of rough surfaces,” *Journal of Lubrication Technology* **93**, 398–407 (1971).
 - [66] J. M. Elson and J. M. Bennett, “Relation between the angular dependence of scattering and the statistical properties of optical surfaces,” *JOSA* **69**, 31–47 (1979).
 - [67] “Geometrical product specifications (GPS) – surface texture: Areal – part 2: Terms, definitions and surface texture parameters,” (ISO 25178-2:2012).
 - [68] J. C. Stover, S. Schröder, and T. A. Germer, “Upper roughness limitations on the TIS/RMS relationship,” *Proc. SPIE* **8495**, 849503–1–7 (2012).
 - [69] J. C. Stover, “The art of specifying optics for scatter,” *Proc. SPIE* **6291**, 629100–1–9 (2006).
 - [70] J. S. r. B. Rayleigh, “On the dynamical theory of gratings,” *Proceedings of the Royal Society of London. Series A* **LXXIX**, 399–416 (1907).
 - [71] J. S. r. B. Rayleigh, *The theory of sound Vol. II* (1896), 2nd ed.
 - [72] A. V. Vinogradov, N. N. Zorev, I. V. Kozhevnikov, S. I. Sagitov, and A. G. Turyanskii, “X-ray scattering by highly polished surfaces,” *Sov. Phys. JETP* **67**, 1631–1638 (1988).
 - [73] S. Sinha, E. Sirota, S. Garoff, and H. Stanley, “X-ray and neutron scattering from rough surfaces,” *Physical Review B* **38**, 2297–2311 (1988).
 - [74] E. L. Church, H. A. Jenkinson, and J. M. Zavada, “Relationship between surface scattering and microtopographic features,” *Opt. Eng.* **18**, 125–136 (1979).
 - [75] J. M. Bennet and L. Mattsson, *Introduction to Surface Rougness and Scattering* (Optical Society of America, Washington, 1993), 2nd ed.
 - [76] E. L. Church, “Fractal surface finish,” *Appl. Opt.* **27**, 1518–1526 (1988).
 - [77] T. V. Amotchkina, V. Janicki, J. Sancho-Parramon, A. V. Tikhonravov, M. K. Trubetskov, and H. Zorc, “General approach to reliable characterization of thin metal films,” *Appl. Opt.* **50**, 1453–64 (2011).

- [78] J. C. Stover, “Rough surface characterization and comparison of scatter measurements and models,” *Proc. SPIE* **5878**, 58780U–58780U–8 (2005).
- [79] J. C. Stover, S. A. Serati, and C. H. Gillespie, “Calculation of surface statistics from light scatter,” *Opt. Eng.* **23**, 406–412 (1984).
- [80] J. M. Elson and J. M. Bennett, “Vector scattering theory,” *Opt. Eng.* **18**, 116–124 (1979).
- [81] E. L. Church, “The measurement of surface texture and topography by differential light scattering,” *Wear* **57**, 93–105 (1979).
- [82] E. L. Church, “Role of surface topography in x-ray scattering,” *Proc. SPIE* **184**, 196–202 (1979).
- [83] I. V. Kozhevnikov and M. V. Pyatakhin, “Use of DWBA and perturbation theory in X-ray control of the surface roughness,” *Journal of X-ray science and technology* **8**, 253–275 (2000).
- [84] P. Beckmann and A. Spizzichino, *The Scattering of Electromagnetic Waves from Rough Surfaces* (Artech House, Inc., Norwood, 1968 / 1987). Series: Artech House Radar Library.
- [85] J. M. Elson, J. P. Rahn, and J. M. Bennett, “Relationship of the total integrated scattering from multilayer-coated optics to angle of incidence, polarization, correlation length, and roughness cross-correlation properties,” *Appl. Opt.* **22**, 3207–3219 (1983).
- [86] S. Schröder, T. Feigl, A. Duparré, and A. Tünnermann, “EUV reflectance and scattering of Mo/Si multilayers on differently polished substrates,” *Opt. Express* **15**, 808–817 (2007).
- [87] J. E. Harvey, “Total integrated scatter from surfaces with arbitrary roughness, correlation widths, and incident angles,” *Opt. Eng.* **51**, 013402 (2012).
- [88] E. Hecht, *Optik* (Oldenbourg Verlag München, Wien, 2001), 3rd ed.
- [89] P. Beckmann, “II Scattering of light by rough surfaces,” *Progress in optics* **VI**, 55–69 (1967).
- [90] D. Yim and S. Kim, “Optical roughness measurement of ground surfaces by light scattering,” *International Journal of Machine Tools and Manufacturing* **30**, 283–289 (1990).
- [91] M. Ohlídal, “The scattering of light from rough surfaces and its application in surface roughness measurement,” *Manufacturing Engineering/ Vyrobné Inžinierstvo* **4**, 17–20 (2007).
- [92] J. Caron, J. Lafait, and C. Andraud, “Scalar Kirchhoff’s model for light scattering from dielectric random rough surfaces,” *Opt. Commun.* **207**, 17–28 (2002).
- [93] J. Eastman and P. Baumeister, “The microstructure of polished optical surfaces,” *Opt. Commun.* **12**, 418–420 (1974).
- [94] A. Krywonos, “Predicting surface scatter using a linear systems formulation of non-paraxial scalar diffraction,” Ph.D. thesis, University of Central Florida (2006).
- [95] H. Ragheb and E. R. Hancock, “Testing new variants of the Beckmann-Kirchhoff model against radiance data,” *Computer Vision and Image Understanding* **102**, 145–168 (2006).
- [96] V. E. Asadchikov, I. V. Kozhevnikov, Y. S. Krivonosov, R. Mercier, T. H. Metzger, C. Morawe, and E. Ziegler, “Application of X-ray scattering technique to the study of supersmooth surfaces,” *Nuclear Instruments and Methods in Physics Research Section A: Accelerators, Spectrometers, Detectors and Associated Equipment* **530**, 575–595 (2004).
- [97] S. K. Nayar, K. Ikeuchi, and T. Kanade, “Surface reflection: physical and geometrical perspectives,” **13**, 611–634 (1991).

- [98] C. Carniglia, “Scalar scattering theory for multilayer optical coatings,” *Opt. Eng.* **18**, 104–115 (1979).
- [99] J. M. Zavislan, “Angular scattering from optical interference coatings: scalar scattering predictions and measurements,” *Appl. Opt.* **30**, 2224–44 (1991).
- [100] V. Holý, J. Kubena, I. Ohlídal, K. Lischka, and W. Plotz, “X-ray reflection from rough layered systems,” *Physical review B* **47**, 15896–15903 (1993).
- [101] V. Holý and T. Baumbach, “Nonspecular x-ray reflection from rough multilayers,” *Physical Review B* **49**, 10668–10676 (1994).
- [102] D. G. Stearns, D. P. Gaines, D. W. Sweeney, and E. M. Gullikson, “Nonspecular x-ray scattering in a multilayer-coated imaging system,” *J. Appl. Phys.* **84**, 1003–1028 (1998).
- [103] P. Bousquet, F. Flory, and P. Roche, “Scattering from multilayer thin films: theory and experiment,” *J. Opt. Soc. Am.* **71**, 1115–1123 (1981).
- [104] P. Bussemer, K. Hehl, and S. Kassam, “Theory of light scattering from rough surfaces and interfaces and from volume inhomogeneities in an optical layer stack,” *Waves in random media* **1**:4, 207–221 (1991).
- [105] J. M. Elson, “Diffraction and diffuse scattering from dielectric multilayers,” *J. Opt. Soc. Am.* **69**, 48–54 (1979).
- [106] E. Kröger and E. Kretschmann, “Scattering of light by slightly rough surfaces or thin films including plasma resonance emission,” *Zeitschrift für Physik* **237**, 1–15 (1970).
- [107] Implemented by Josep Ferré-Borrull, formerly Fraunhofer IOF, Jena.
- [108] P. H. Berning, “Theory and calculations of optical thin films,” in “Physics of Thin Films,” , vol. 1 G. Hass, ed. (Academic, New York, 1963), pp. 69–121.
- [109] M. Born and E. Wolf, *Principles of Optics* (Camebridge University Press, 2002), 7th ed.
- [110] T. Herffurth, M. Trost, S. Schröder, K. Täschner, H. Bartzsch, P. Frach, A. Duparré, and A. Tünnermann, “Roughness and optical losses of rugate coatings,” *Appl. Opt.* **53**, A351–359 (2014).
- [111] E. G. Johnson, “Simulating the scratch standards for optical surfaces: theory,” *Appl. Opt.* **22**, 4056–4068 (1983).
- [112] “Optics and photonics - preparation of drawings for optical elements and systems - part 7: Surface imperfection tolerances,” (ISO 10110-7:2008) (2008).
- [113] “Optical components for fire control instruments; general specification governing the manufacture, assembly, and inspection of,” (MIL-PRF-13830B) (1997).
- [114] “Optics and electro-optical instruments - optical elements and assemblies - appearance imperfections,” (ANSI/OEOSC OP1.002-2009) (2009).
- [115] T. Rinder and H. Rothe, “Performance limits of ARS sensors based on CMOS photodiode array,” *Proc. SPIE* **4779**, 72–82 (2002).
- [116] P. Williams, D. Lubnau, and D. Elliott, “Generation of fractal images and comparison of their PSDs with several models,” *Twenty-Second Asilomar Conference on Signals, Systems and Computers* **1**, 495–499 (1988).
- [117] M. Blanco, “On clutter modeling and the spectra of two-dimensional Gauss-Markov random signals,” **75**, 228–234 (1982).
- [118] C. A. Mack, “Analytic form for the power spectral density in one, two, and three dimensions,” *Journal of Micro/Nanolithography, MEMS, and MOEMS* **10**, 040501 (2011).

- [119] G. Brown, “Backscattering from a Gaussian-distributed perfectly conducting rough surface,” **26**, 472–482 (1978).
- [120] E. Bahar and M. A. Fitzwater, “Like- and cross-polarized scattering cross sections for random rough surfaces: theory and experiment,” *J. Opt. Soc. Am. A* **2**, 2295 (1985).
- [121] E. Bahar, D. Barrick, and M. A. Fitzwater, “Computations of scattering cross sections for composite surfaces and the specification of the wavenumber where spectral splitting occurs,” **13**, 698–709 (1983).
- [122] E. L. Church and P. Z. Takacs, “Statistical and signal processing concepts in surface metrology,” *Proc. SPIE* **645**, 107–115 (1986).
- [123] E. L. Church and H. Berry, “Spectral analysis of the finish of polished optical surfaces,” *Wear* **83**, 189–201 (1982).
- [124] G. Palasantzas, “Roughness spectrum and surface width of self-affine fractal surfaces via the K-correlation model,” *Physical review B* **48**, 472–478 (1993).
- [125] E. L. Church and P. Z. Takacs, “The optimal estimation of finish parameters,” *Proc. SPIE* **1530**, 71–85 (1991).
- [126] M. G. Dittman, “K-correlation power spectral density and surface scatter model,” *Proc. SPIE* **6291**, 62910R–1–12 (2006).
- [127] D. Rönnow, J. Isidorsson, and G. A. Niklasson, “Surface roughness of sputtered ZrO₂ films studied by atomic force microscopy and spectroscopic light scattering,” *Physical Review E* **54**, 4021–4026 (1996).
- [128] M. Flemming and A. Duparré, “Design and characterization of nanostructured ultrahydrophobic coatings,” *Appl. Opt.* **45**, 1397–1401 (2006).
- [129] E. Spiller, D. G. Stearns, and M. Krumrey, “Multilayer x-ray mirrors: Interfacial roughness, scattering, and image quality,” *J. Appl. Phys.* **74**, 107–118 (1993).
- [130] S. F. Edwards and D. R. Wilkinson, “The surface statistics of a granular aggregate,” *Proceedings of the Royal Society A: Mathematical, Physical and Engineering Sciences* **381**, 17–31 (1982).
- [131] W. Tong and R. Williams, “Kinetics of surface growth: phenomenology, scaling, and mechanisms of smoothening and roughening,” *Annu. Rev. Phys. Chem.* **45**, 401–438 (1994).
- [132] J. M. Elson, J. P. Rahn, and J. M. Bennett, “Light scattering from multilayer optics: comparison of theory and experiment,” *Appl. Opt.* **19**, 669–679 (1980).
- [133] H.-G. Walther, A. Duparré, and G. Schirmer, “Scattering reduction or enhancement by a dielectric single layer,” *Appl. Opt.* **25**, 4527–4529 (1986).
- [134] A. Duparré and H.-G. Walther, “Surface smoothing and roughening by dielectric thin film deposition,” *Appl. Opt.* **27**, 1393–1395 (1988).
- [135] S. Schröder, “Light scattering of optical components at 193 nm and 13.5 nm,” Ph.D. thesis, Friedrich-Schiller-Universität Jena (2008).
- [136] M. Trost, T. Herffurth, S. Schröder, A. Duparré, and A. Tünnermann, “Scattering reduction through oblique multilayer deposition,” *Appl. Opt.* **53**, A197–204 (2014).
- [137] J. V. Grishchenko and M. L. Zhanavskina, “Investigation into the correlation factor of substrate and multilayer film surfaces by atomic force microscopy,” *Crystallogr. Rep.* **58**, 493–497 (2013).
- [138] R. Messier, “Toward quantification of thin film morphology,” *Journal of Vacuum Science*

- & Technology A: Vacuum, Surfaces, and Films **4**, 490 (1986).
- [139] J. Krug, “Power laws in surface physics: the deep, the shallow and the useful,” *Physica A: Statistical Mechanics and its Applications* **340**, 647–655 (2004).
 - [140] C. Amra, J. H. Apfel, and E. Pelletier, “Role of interface correlation in light scattering by a multilayer,” *Appl. Opt.* **31**, 3134–51 (1992).
 - [141] J. M. Elson, “Infrared light scattering from surfaces covered with multiple dielectric overlayers,” *Appl. Opt.* **16**, 2872–2881 (1977).
 - [142] J. Ferré-Borrull, A. Duparré, and E. Quesnel, “Roughness and light scattering of ion-beam-sputtered fluoride coatings for 193 nm,” *Appl. Opt.* **39**, 5854–5864 (2000).
 - [143] C. C. Asmail, J. Hsia, A. Parr, and J. Hoeft, “Rayleigh scattering limits for low-level bidirectional reflectance distribution function measurements,” *Appl. Opt.* **33**, 6084–91 (1994).
 - [144] C. C. Asmail, J. Hsia, and A. Parr, “Rayleigh scattering limits for low-level bidirectional reflectance distribution function measurements: corrigendum,” *Appl. Opt.* **33**, 6084–91 (1994).
 - [145] M. Barilli and A. Mazzoni, “An equipment for measuring 3D bi-directional scattering distribution function of black painted and differently machined surfaces,” *Proc. SPIE* **5962**, 59620L–1–12 (2005).
 - [146] B. H. Zimm, “Apparatus and methods for measurement and interpretation of the angular variation of light scattering; preliminary results on polystyrene solutions,” *The Journal of Chemical Physics* **16**, 1099–1116 (1948).
 - [147] P. P. Debye, “A photoelectric instrument for light scattering measurements and a differential refractometer,” *J. Appl. Phys.* **17**, 392–398 (1946).
 - [148] B. Brice, M. Halwer, and R. Speiser, “Photoelectric light-scattering photometer for determining high molecular weights,” *J. Opt. Soc. Am.* **18**, 768–778 (1950).
 - [149] A. von Finck, “Table top system for angle resolved light scattering measurement,” Ph.D. thesis, Technische Universität Imenau (2013).
 - [150] M. Trost, S. Schröder, C. C. Lin, A. Duparré, and A. Tünnermann, “Roughness characterization of EUV multilayer coatings and ultra-smooth surfaces by light scattering,” *Proc. SPIE* **8501**, 85010F–1–7 (2012).
 - [151] A. von Finck, M. Hauptvogel, and A. Duparré, “Instrument for close-to-process light scatter measurements of thin film coatings and substrates,” *Appl. Opt.* **50**, C321–C328 (2011).
 - [152] M. Trost, T. Herfurth, and S. Schröder, “Verfahren zur hochempfindlichen Streulichtmessung,” (DE102012106322B3, 2012).
 - [153] T. A. Germer and C. C. Asmail, “A goniometric optical scatter instrument for bidirectional reflectance distribution function measurements with out-of-plane and polarimetry capabilities,” *Proc. SPIE* **3141**, 220–231 (1997).
 - [154] C. Hahlweg and H. Rothe, “Non-goniometric scatterometry - A review,” *Proc. SPIE* **6682**, 66820D–1–15 (2007).
 - [155] H. Bennett and J. O. Porteus, “Relation between surface roughness and specular reflectance at normal incidence,” *J. Opt. Soc. Am.* **51**, 123–129 (1961).
 - [156] H. Bennett, “Scattering characteristics of optical materials,” *Opt. Eng.* **17**, 480–488 (1978).

- [157] D. Rönnow and E. Veszelei, “Design review of an instrument for spectroscopic total integrated light scattering measurements in the visible wavelength region,” *Rev. Sci. Instrum.* **65**, 327–334 (1994).
- [158] D. Rönnow and A. Roos, “Stray-light corrections in integrating-sphere measurements on low-scattering samples,” *Appl. Opt.* **33**, 6092–6097 (1994).
- [159] L. Mattsson, “Characterization of supersmooth surfaces by light scattering techniques,” *Proc. SPIE* **1009**, 165–171 (1989).
- [160] S. Gliech, J. Steinert, and A. Duparré, “Light-scattering measurements of optical thin-film components at 157 and 193 nm,” *Appl. Opt.* **41**, 3224–3235 (2002).
- [161] L. X. Cao, T. V. Vorburger, A. George Lieberman, and T. R. Lettieri, “Light-scattering measurement of the rms slopes of rough surfaces,” *Appl. Opt.* **30**, 3221–7 (1991).
- [162] B. M. Nebeker, G. W. Starr, and E. D. Hirleman, “Light scattering from patterned surfaces and particles on surfaces,” *Proc. SPIE* **2638**, 274–284 (1995).
- [163] S. Roy, A. C. Assafr, S. F. Pereira, and H. P. Urbach, “Coherent Fourier scatterometry for detection of nanometer-sized particles on a planar substrate surface,” *Opt. Express* **22**, 304–313 (2014).
- [164] T. Herffurth, S. Schröder, M. Trost, A. Duparré, and A. Tünnermann, “Comprehensive nanostructure and defect analysis using a simple 3D light-scatter sensor,” *Appl. Opt.* **52**, 3279–3287 (2013).
- [165] S. Schröder, T. Herffurth, A. Duparré, and G. Notni, “Vorrichtung und Verfahren zur winkelaufgelösten Streulichtmessung,” (DE102009036383B3, 2009).
- [166] R. Brodmann and G. Thurn, “Roughness measurement of ground, turned and shot-peened surfaces by the light scattering method,” *Wear* **109**, 1–13 (1986).
- [167] D. Yan, J. E. Kaye, S. Balakrishnan, and N. Popplewell, “Surface roughness measurements in finish turning,” *The International Journal of Advanced Manufacturing Technology* **11**, 91–100 (1996).
- [168] S. Wang, C. Quan, C. J. Tay, and H. Shang, “Surface roughness measurement in the submicrometer range using laser scattering,” *Opt. Eng.* **39**, 1597–1601 (2000).
- [169] C. Lukianowicz and T. Karpinski, “Optical system for measurement of surface form and roughness,” *Measurement Science Review* **1**, 151–154 (2001).
- [170] H. H. Tsai and H. P. Feng, “On-line inspection of the surface roughness of workpiece in ultraprecision machining,” *Advanced Materials Research* **126-128**, 744–751 (2010).
- [171] H. H. Tsai and H. P. Feng, “Prediction of the roughness of the an ultra-precision machined surface from light scattering by a photo diode array,” *Journal of Technology* **27**, 21–26 (2012).
- [172] Datasheet OptoSurf GmbH, “Sensor OS 500,” <http://www.optosurf.de/images/Datenblaetter/Produktdatenblatt-1-OS500-Sensor.pdf> (2014-05-05).
- [173] Datasheet Schmitt Industries, Inc., “Lasercheck® surface roughness measurement gages,” <http://www.surface-finish.net/6212/technical-data.html> (2014-05-05).
- [174] Datasheet EMG Automation GmbH, “SORM 3plus - Superfast optical roughness measurement,” <http://www.emg-automation.com/nc/automation/qs-systeme/online-rauheitsmessung-sorm-3plus/action/open-download/download/broschuere-sorm-de/> (2014-05-05).

- [175] B. J. Griffiths, R. H. Middleton, and B. Wilkie, “Three-dimensional surface measurement using light scattering,” *International Journal of Machine Tools Manufacturing* **35**, 141–145 (1995).
- [176] G. J. Ward, “Measuring and modeling anisotropic reflection,” *ACM SIGGRAPH Computer Graphics* **26**, 265–272 (1992).
- [177] S. Lysenko, F. Fernández, A. Rúa, and H. Liu, “Ultrafast light scattering imaging of multi-scale transition dynamics in vanadium dioxide,” *J. Appl. Phys.* **114**, 153514–1–8 (2013).
- [178] O. Apel, C. Görling, U. Leinhos, K. Mann, and B. Schafer, “CHARISMA A new way for angular-resolved scattering measurements,” *Proc. SPIE* **4347**, 569–578 (2001).
- [179] S. Holler, J. C. Auger, B. Stout, Y. L. Pan, J. R. Bottiger, R. K. Chang, and G. Videen, “Observations and calculations of light scattering from clusters of spheres,” *Appl. Opt.* **39**, 6873–87 (2000).
- [180] P. Lehmann and G. Goch, “Comparison of Conventional Light Scattering and Speckle Techniques Concerning an In-Process Characterisation of Engineered Surfaces,” *CIRP Annals - Manufacturing Technology* **49**, 419–422 (2000).
- [181] K. J. Dana and J. Wang, “Device for convenient measurement of spatially varying bidirectional reflectance,” *J. Opt. Soc. Am. A* **21**, 1–12 (2004).
- [182] J. Ren and J. Zhao, “Measurement of a bidirectional reflectance distribution and system achievement based on a hemi-parabolic mirror,” *Opt. Lett.* **35**, 1458–60 (2010).
- [183] E. Kawate and M. Hain, “New scatterometer for spatial distribution measurements of light scattering from materials,” *Measurement Science Review* **12**, 56–61 (2012).
- [184] Datasheet Lambda Research Corporation, “ScatterScope3D™ Overview,” http://secure.lambdaresearch.com/software_products/Scatterometers (2014-05-02).
- [185] R. Guo and Z. Tao, “Experimental investigation of a modified Beckmann-Kirchhoff scattering theory for the in-process optical measurement of surface quality,” *Optik - International Journal for Light and Electron Optics* **122**, 1890–1894 (2011).
- [186] A. Hertzsch, K. Kröger, and M. Großmann, “Optical twist measurement by scatterometry,” *AMA conference* pp. 40–45 (2013).
- [187] S. Wadman and S. Bäumer, “Appearance characterisation by a scatterometer employing a hemispherical screen,” *Proc. SPIE* **5189**, 163–173 (2003).
- [188] H. Kostal, D. Kreysar, and R. Rykowski, “Application of Imaging Sphere for BSDF Measurements of Arbitrary Materials,” *Application note Radiant Zemax, LLC* (2013).
- [189] J. Seewig, G. Beichert, R. Brodmann, H. Bodschwinn, and M. Wendel, “Extraction of shape and roughness using scattering light,” *Proc. SPIE* **7389**, 73890N–1–11 (2009).
- [190] Y. Mukaigawa, K. Sumino, and Y. Yagi, “Rapid BRDF measurement using an ellipsoidal mirror and a projector,” *IPSJ Transactions on Computer Vision and Applications* **1**, 21–32 (2009).
- [191] R. Yeo and D. Kreysar, “The imaging sphere® - the first appearance meter? presentation slides,” .
- [192] A. Kasper and H. Rothe, “Evaluation of in-situ ARS sensors for characterizing smooth and rough surfaces,” *Proc. SPIE* **3426**, 252–261 (1998).
- [193] R. S. Lu and G. Y. Tian, “On-line measurement of surface roughness by laser light scat-

- tering,” *Meas. Sci. Technol.* **17**, 1496–1502 (2006).
- [194] G. Y. Tian, R. S. Lu, and D. Gledhill, “Surface measurement using active vision and light scattering,” *Optics and Lasers in Engineering* **45**, 131–139 (2007).
- [195] K. E. Torrance and E. Sparrow, “Theory for off-specular reflection from roughened surfaces,” *J. Opt. Soc. Am.* **57**, 1105–1114 (1967).
- [196] Datasheet Photon Focus AG, “MV1-D2080 series (CMOS Camera),” http://www.photonfocus.com/upload/flyers/flyer_A5_MV1-D2080_en_2.0.2.pdf (2014-05-05).
- [197] Datasheet Laserex Technologies, “LDM 4,” <http://www.laserex.net/wp-content/uploads/LDM-4-Brochure.pdf> (2014-05-05).
- [198] Datasheet rgb lasersystems, “miniLas FIBER,” http://www.rgb-laser.com/data/data_pdf_datasheet/MiniLas%20data%20sheet%20for%20web.pdf (2014-05-05).
- [199] N. Blanc, “CCD versus CMOS - has CCD imaging come to an end?” *Photogrammetric Week* **01**, 131–137 (2001).
- [200] C. Coates, B. Fowler, and G. Holst, “sCMOS Scientific CMOS Technology - A High-Performance Imaging Breakthrough,” http://www.scmos.com/files/high/scmos_white_paper_8mb.pdf (2009).
- [201] S. A. Taylor, “CCD and CMOS imaging array technologies: Technology review,” Technical Report Xerox Research Centre Europe pp. EPC–1998–106 (1998).
- [202] D. Litwiller, “CCD VS. CMOS: Facts and Fiction,” *Photonics Spectra* pp. 151–154 (2001).
- [203] Datasheet CMOSIS NV, “Cmv4000,” http://www.cmosis.com/products/standard_products/cmv4000 (2014-03-31).
- [204] S. Yang, I. Vayshenker, X. Li, and T. R. Scott, “Optical detector nonlinearity: A comparison of five methods,” Tech. rep., National Institute of Standards and Technology Optical Electronics Metrology Group.
- [205] S. Yang, I. Vayshenker, X. Li, and T. R. Scott, “Accurate measurement of optical detector nonlinearity,” in “NCSL Workshop & Symposium,” (1994), pp. 353–362.
- [206] L. Coslovi and F. Righini, “Fast determination of the nonlinearity of photodetectors,” *Appl. Opt.* **19**, 3200–3203 (1980).
- [207] J. M. Sanz, C. Extremiana, and J. M. Saiz, “Comprehensive polarimetric analysis of Spectralon white reflectance standard in a wide visible range,” *Appl. Opt.* **52**, 6051–6062 (2013).
- [208] I. Bronstein, K. Semendjajew, G. Musiol, and H. Mühlig, *Taschenbuch der Mathematik* (Harri Deutsch, Frankfurt am Main, Thun, 1999), 4th ed.
- [209] “Uncertainty of measurement - part 3: Guide to the expression of uncertainty in measurement,” (GUM:1995, ISO/IEC Guide 98-3:2008) (2008).
- [210] K.-D. Sommer and B. R. L. Siebert, “Praxisgerechtes Bestimmen der Messunsicherheit nach GUM,” *Technisches Messen* **71**, 52–66 (2004).
- [211] G. Meister, A. Rothkirch, B. Hosgood, H. Spitzer, and J. Bienlein, “Error analysis for BRDF measurements at the European goniometric facility,” *Remote Sensing Reviews* **19**, 111–131 (2000).
- [212] F. M. Cady, D. R. Bjork, J. Rifkin, and J. C. Stover, “BRDF error analysis,” *Proc. SPIE* **1165**, 154–164 (1989).
- [213] T. F. Schiff, J. C. Stover, D. J. Wilson, D. S. Brett, M. E. Southwood, and D. R. Bjork,

- “Design review of a unique out-of-plane polarimetric scatterometer,” *Proc. SPIE* **1753**, 262–268 (1992).
- [214] T. Herffurth, “Untersuchungen zu Reflexion und Streulicht von EUV-Komponenten,” diploma thesis, Friedrich-Schiller-Universität Jena (2008).
- [215] B. R. L. Siebert and K.-D. Sommer, “Weiterentwicklung des GUM und Monte-Carlo-Techniken (New developments of the GUM and Monte Carlo techniques),” *Technisches Messen* **71**, 67–80 (2004).
- [216] J. E. Harvey and R. V. Shack, “Aberrations of diffracted wave fields,” *Appl. Opt.* **17**, 3003–3009 (1978).
- [217] J. C. Stover, S. Schröder, A. von Finck, and A. Duparré, “Estimating hemispherical scatter from incident plane measurements of isotropic samples,” *Proc. SPIE* **8495**, 84950F–1–8 (2012).
- [218] J. M. Elson, “Characteristics of far-field scattering by means of surface roughness and variations in subsurface permittivity,” *Waves in Random Media* **7**, 303–317 (1997).
- [219] O. Kienzle, J. Staub, and T. Tschudi, “Light scattering from transparent substrates: Theory and experiment,” *Physical review. B, Condensed matter* **50**, 1848–1860 (1994).
- [220] J. E. Harvey, “Fourier treatment of near-field scalar diffraction theory,” *American Journal of Physics* **47**, 974–980 (1979).
- [221] J. W. Goodman, *Introduction to Fourier Optics* (McGraw-Hill, New York, Singapore, 1996), 2nd ed.
- [222] J. E. Harvey, N. Choi, A. Krywonos, and J. G. Marcen, “Calculating BRDFs from surface PSDs for moderately rough optical surfaces,” *Proc. SPIE* **7426**, 74260I–74260I–9 (2009).
- [223] V. Celli, A. Marvin, and F. Toigo, “Ligth scattering from rough surfaces,” *Physical review B* **11**, 1779–1786 (1975).
- [224] T. V. Vorburger, E. Marx, and T. R. Lettieri, “Regimes of surface roughness measurable with light scattering,” *Appl. Opt.* **32**, 3401–3408 (1993).
- [225] H. Tiziani, “Optical methods for precision measurements,” *Opt. Quantum. Electron.* **21**, 253–282 (1989).
- [226] A. Weckenmann, O. Tan, J. Hoffmann, and Z. Sun, “Practice-oriented evaluation of lateral resolution for micro- and nanometre measurement techniques,” *Meas. Sci. Technol.* **20**, 065103 (2009).
- [227] T. Herffurth, S. Schröder, O. Tan, S. Apel, M. Senoner, and M. Sahre, “Rauheitsbewertung beschichteter Oberflächen,” in “Neue Strategien der Mess- und Prüftechnik für die Produktion von Mikrosystemen und Nanostrukturen, Abschlussbericht DFG SPP 1159,” A. Weckenmann, ed. (Shaker Verlag, 2011).
- [228] L. Coriand, “Roughness, wetting, and optical properties of functional surfaces,” Ph.D. thesis, Friedrich-Schiller-Universität Jena (2012).
- [229] R. Garcia and R. Perez, “Dynamic atomic force microscopy methods,” *Surf. Sci. Rep.* **47**, 197–301 (2002).
- [230] A. Schirmeisen, B. Anczykowski, and H. Fuchs, “Dynamic modes of atomic force microscopy,” in “Springer Handbook of Nanotechnology,” B. Bhushan, ed. (Springer Berlin Heidelberg, 2007), chap. 27, pp. 737–765.
- [231] M. Flemming, “Methoden der Simulation und Charakterisierung von nanostrukturierten

- ultrahydrophoben Oberflächen für optische Anwendungen,” Ph.D. thesis, Technische Universität Imenau (2006).
- [232] L. R. Baker, “Surface imperfections: specimen measurement by microscope and digital camera,” *Opt. Eng.* **40**, 2059–2060 (2001).
- [233] D. Liu, Y. Yang, L. Wang, Y. Zhuo, C. Lu, L. Yang, and R. Li, “Microscopic scattering imaging measurement and digital evaluation system of defects for fine optical surface,” *Opt. Commun.* **278**, 240–246 (2007).
- [234] Z. W. Zhong, L. P. Zhao, and L. J. Wang, “Investigaton of light scattering for scratch detection,” *Proc. SPIE* **7155**, 71552W–1–8 (2008).
- [235] D. Takaki and D. M. Aikens, “Objective scratch and dig measurements,” *Technical Digest Savvy*, <http://www.savvyoptics.com> pp. 1–12 (2012).
- [236] Q. Turchette and T. Turner, “Developing a more useful surface quality metric for laser optics,” *Proc. SPIE* **7912**, 791213–1–10 (2011).
- [237] S. Stokowski and M. Vaez-Iravani, “Wafer inspection technology challenges for ULSI manufacturing,” *AIP Conference Proceedings* **449**, 405–415 (1998).
- [238] K. Takami, “Defect inspection of wafers by laser scattering,” *Materials Science and Engineering: B* **44**, 181–187 (1997).
- [239] A. Chen, V. Huang, S. Chen, C. J. Tsai, K. Wu, H. Zhang, K. Sun, J. Saito, H. Chen, D. Hu, M. Li, W. Shen, and U. Mahajan, “Advanced inspection methodologies for detection and classification of killer substrate defects,” *Proc. SPIE* **7140**, 71400W–1–10 (2008).
- [240] J. C. Stover, “Light scatter metrology of diamond turned optics,” *Proc. SPIE* **5878**, 58780R–1–7 (2005).
- [241] S. N. Shafir, J. C. Lambropoulos, and S. D. Jacobs, “Subsurface damage and microstructure development in precision microground hard ceramics using magnetorheological finishing spots,” *Appl. Opt.* **46**, 5500–5015 (2007).
- [242] S. D. Jacobs, F. Yang, E. M. Fess, J. B. Feingold, B. E. Gillman, W. I. Kordonski, H. Edwards, and D. Golini, “Magnetorheological finishing of IR materials,” *Proc. SPIE* **3134**, 258–269 (1997).
- [243] S. Gliech, R. Wendt, and A. Duparré, “UV-VIS-NIR scatter measurement methods for ultra precision surfaces and coatings,” *Optical Interference Coatings*, Technical Digest p. ThA2 (2007).
- [244] R. Steinkopf, A. Gebhardt, S. Scheiding, M. Rohde, O. Stenzel, S. Gliech, V. Giggel, H. Löscher, G. Ullrich, P. Rucks, A. Duparré, S. Risse, R. Eberhardt, and A. Tünnermann, “Metal mirrors with excellent figure and roughness,” *Proc. SPIE* **7102**, 71020C–1–12 (2008).
- [245] P. Takacs, “Minimizing artifacts in analysis of surface statistics,” *Optical Fabrication and Testing*, Technical Digest p. OTi1D (2012).
- [246] H. El-ghandoor, M. Saady, and A. Ashour, “Analysis of surface roughness using laser optical imaging techniques,” *Journal of Materials Science and Engineering B* **2**, 7–15 (2012).
- [247] C. Amra, “From light scattering to the microstructure of thin-film multilayers,” *Appl. Opt.* **32**, 5481–91 (1993).
- [248] P. Roche and E. Pelletier, “Characterizations of optical surfaces by measurement of scattering distribution,” *Appl. Opt.* **23**, 3561 (1984).

- [249] D. L. Windt, “IMD - Software for modeling the optical properties of multilayer films,” *Computers in Physics* **12**, 360 (1998).
- [250] M. C. Gerchman, “Specifications and manufacturing considerations of diamond machined optical components,” *Proc. SPIE* **0607**, 36–45 (1986).
- [251] J. Qu and A. J. Shih, “Analytical surface roughness parameters of a theoretical profile consisting of elliptical arcs,” *Machining Science and Technology* **7**, 281–294 (2003).
- [252] M. Riedl, *Optical Design Fundamentals for Infrared Systems*, Spie P. Series (SPIE-Press, Bellingham, WA, 2001), 2nd ed.
- [253] P. R. Dumas, D. Golini, and M. Tricard, “Improve figure and finish of diamond turned surfaces with Magneto-Rheological Finishing (MRF),” *Proc. SPIE* **5786**, 296–304 (2005).
- [254] M. Tricard, P. R. Dumas, and G. Forbes, “Sub-aperture approaches for asphere polishing and metrology,” *Proc. SPIE* **5638**, 284–299 (2005).
- [255] W. I. Kordonski and S. D. Jacobs, “Magnetorheological finishing,” *International Journal of Modern Physics B* **10**, 2837–2848 (1996).
- [256] C. Supranowitz, C. Hall, P. R. Dumas, and B. Hallock, “Improving surface figure and microroughness of IR materials and diamond turned surfaces with magnetorheological finishing (MRF),” *Proc. SPIE* **6545**, 65450S–1–11 (2007).
- [257] S. Scheiding, M. Beier, U.-D. Zeitner, S. Risse, and A. Gebhardt, “Freeform mirror fabrication and metrology using a high performance test CGH and advanced alignment features,” *Proc. SPIE* **8613**, 86130J–1–15 (2013).
- [258] D. Golini, “Precision optics manufacturing using magnetorheological finishing (MRF),” *Proc. SPIE* **3739**, 78–85 (1999).
- [259] J. C. Lambropoulos, C. Miao, and S. D. Jacobs, “Magnetic field effects on shear and normal stresses in magnetorheological finishing,” *Opt. Express* **18**, 19713–19723 (2010).
- [260] S. Wan, W. Fong, and Z. Tay, “Process modeling and simulation of vibratory finishing of fixtured components,” 10th International Conference of the European Society for Precision Engineering and Nanotechnology pp. 164–168 (2010).
- [261] C. W. Kum, T. Sato, and S. Wan, “Surface roughness as a function of work done by tangential force in magneto-rheological finishing,” *Advanced Materials Research* **565**, 249–254 (2012).
- [262] C. W. Kum, T. Sato, and S. Wan, “Surface roughness and material removal models for magnetorheological finishing,” *International Journal of Abrasive Technology* **6**, 70–91 (2013).
- [263] Z. Shen, S. Hou, H. Sun, X. Zhao, and Z. Xue, “Local oxidation of titanium thin films using an atomic force microscope under static and pulsed voltages,” *J. Phys. D: Appl. Phys.* **37**, 1357–1361 (2004).
- [264] A. Dasgupta, A. Singh, P. K. Parida, R. Ramaseshan, P. Kuppusami, S. Saroja, and M. Vijayalakshmi, “Structural characteristics of titanium coating on copper substrates,” *Bull. Mater. Sci.* **34**, 483–489 (2011).
- [265] K. H. Guenther, I. Penny, and R. R. Willey, “Corrosion-resistant front surface aluminum mirror coatings,” *Opt. Eng.* **32**, 547–552 (1993).
- [266] A. Duparré, M. Flemming, J. Steinert, and K. Reihs, “Optical coatings with enhanced roughness for ultrahydrophobic, low-scatter applications,” *Appl. Opt.* **41**, 3294–3298 (2002).

- [267] C. A. Mack, “Systematic errors in the measurement of power spectral density,” *Journal of Micro/Nanolithography, MEMS, and MOEMS* **12**, 033016–1–10 (2013).
- [268] R. Canestrari, D. Spiga, and G. Pareschi, “Analysis of microroughness evolution in X-ray astronomical multilayer mirrors by surface topography with the MPES program and by X-ray scattering,” *Proc. SPIE* **6266**, 626613–1–14 (2006).
- [269] L. Peverini, E. Ziegler, T. Bigault, and I. V. Kozhevnikov, “Roughness conformity during tungsten film growth: An in situ synchrotron x-ray scattering study,” *Physical Review B* **72**, 045445 (2005).
- [270] M. Scherer, U. Schallenberg, H. Hagedorn, W. Lehnert, B. Romanov, and A. Zoeller, “High performance notch filter coatings produced with PIAD and magnetron sputtering,” *Proc. SPIE* **7101**, 71010I (2008).
- [271] U. Schallenberg, B. Ploss, M. Lappschies, and S. Jakobs, “Design and manufacturing of high-performance notch filters,” *Proc. SPIE* **7739**, 77391X–1–9 (2010).
- [272] Derived from personal communication with Ralf Schmauder (Institut für Physiologie II, Universitätsklinikum Jena) (2014-01-29).
- [273] H. Petty, “Fluorescence microscopy: established and emerging methods, experimental strategies, and applications in immunology,” *Microsc. Res. Tech.* **70**, 687–709 (2007).
- [274] C. Grèzes-Besset, D. Torricini, H. Krol, M. Zerrad, M. Lequime, and C. Amra, “Angular and spectral light scattering from complex multielectric coatings,” *Proc. SPIE* **8168**, 81680D–1–7 (2011).
- [275] M. Zerrad, M. Lequime, and C. Amra, “Multimodal scattering facilities and modelization tools for a comprehensive investigation of optical coatings,” *Proc. SPIE* **8169**, 81690K–1–13 (2011).
- [276] E. Spiller, *Soft X-ray Optics* (SPIE-Press, Bellingham, WA, 1994).
- [277] G. A. Johansson, M. Berglund, F. Eriksson, J. Birch, and H. M. Hertz, “Compact soft x-ray reflectometer based on a line-emitting laser-plasma source,” *Rev. Sci. Instrum.* **72**, 58–62 (2001).
- [278] M. Trost, S. Schröder, T. Feigl, A. Duparré, and A. Tünnermann, “Influence of the substrate finish and thin film roughness on the optical performance of Mo/Si multilayers,” *Appl. Opt.* **50**, C148–53 (2011).
- [279] M. Opel, “Kamera-basierte winkelaufgelöste Streulichtmessung an optischen Komponenten,” master’s thesis, University of Applied Sciences Jena (EAH) (2014).
- [280] J. H. McLeod and W. T. Sherwood, “A proposed method of specifying appearance defects of optical parts,” *J. Opt. Soc. Am.* **35**, 136–138 (1945).
- [281] J. H. Kim, S. H. Ehrman, G. W. Mulholland, and T. A. Germer, “Polarized light scattering by dielectric and metallic spheres on silicon wafers,” *Appl. Opt.* **41**, 5405–12 (2002).
- [282] M. Ohlidal, “Comparison of the two-dimensional Fraunhofer and the two-dimensional Fresnel approximations in the analysis of surface roughness by angle speckle correlation,” *J. Mod. Opt.* **38**, 2115–2135 (1991).
- [283] S. Junger, W. Tschekalinskij, N. Verwaal, and N. Weber, “Polarization- and wavelength-sensitive sub-wavelength structures fabricated in the metal layers of deep submicron CMOS processes,” *Proc. SPIE* **7712**, 77120F–1–10 (2010).

A. Auxiliary calculations

A.1. Estimation of fluorescence power in laser scanning microscopy

This estimation is based on data provided by Ralf Schmauder [272].

The power of the stimulated radiation that reaches the detector in fluorescence microscopy is about 3×10^{-15} W. The stimulating power density is 10 kW/cm^2 . This corresponds to 7×10^{-6} W in a confocal volume of 300 nm in diameter.

Through scattering in the confocal volume or other re-reflexes in the beam path, a portion of the stimulating light is imaged to the detector. If the confocal volume is highly scattering (Lambertian) and the objective has an acceptance angle of 60° , a solid angle of 0.8 sr is covered. This corresponds to a collected power of about 4×10^{-7} W.

After passing a beam splitter and the emission filter in the microscope, which filters about 2-3 and 5-6 orders of magnitude, respectively, the stimulating light that reaches the detector can still be in the order of 4×10^{-14} W to 4×10^{-16} W.

On the other hand, a scattering loss that is in the order of this transmitted power, as shown for the notch filter, would be critically as well.

A.2. Asymptotic evolution of correlation length

Analytical solutions of the correlation length for the modified PSD model only exist for some specific parameters. However, the asymptotic similarity to the ABC-model can be exploited to translate the parameters $\Omega\nu\eta$ into the parameters ABC [135]. Thereafter, Eq. 3.11 can be utilized to derive the approximate behavior of the correlation length as function of β :

$$\lim_{f \rightarrow 0} \Omega \frac{1 - e^{-2\nu|2\pi f|^\eta d^{2\beta}}}{2\nu|2\pi f|^\eta} = \Omega d^{2\beta} \quad \text{and} \quad \lim_{f \rightarrow 0} \frac{A}{(1 + B^2 f^2)^{\frac{C+1}{2}}} = A \quad \text{implies that} \quad \Omega d^{2\beta} \triangleq A.$$

In a similar way the remaining parameters can be transformed into each other:

$$\lim_{f \rightarrow \infty} \Omega \frac{1 - e^{-2\nu|2\pi f|^\eta d^{2\beta}}}{2\nu|2\pi f|^\eta} = \Omega \frac{1}{2\nu|2\pi f|^\eta} \quad \text{and} \quad \lim_{f \rightarrow \infty} \frac{A}{(1 + B^2 f^2)^{\frac{C+1}{2}}} = \frac{A}{(B^2 f^2)^{\frac{C+1}{2}}} \quad \text{result in}$$

$$C \triangleq \eta - 1 \quad \text{and} \quad B \triangleq 2\pi \left(d^{2\beta} 2\nu \right)^{1/\eta}.$$

Applying these asymptotic identities into Eq. 3.11 reveals the behavior of the correlation length which is stated for example in [131,135]: $\tau_{cor} \propto d^{\beta \frac{2}{\eta}}$.

Kurzfassung

Die in-line Charakterisierung optischer Oberflächen erfordert robuste, berührungslose und schnelle Verfahren mit hoher Sensitivität. Zur Erfüllung dieser Anforderungen bei der Bewertung von Oberflächenrauheit und Defekten waren die Entwicklung einer Streulichtsensorik sowie speziell angepasster Analysemethoden notwendig. Diese Kombination ermöglicht einerseits die Bewertung des durch Oberflächenunvollkommenheiten hervorgerufenen Störlichts. Andererseits können durch modelltheoretische Zusammenhänge Information über die das Streulicht verursachenden Strukturen selbst gewonnen werden.

Das realisierte Sensorkonzept für 3D winkelaufgelöste Streulichtmessungen ermöglicht Rauheitsmessungen an optischen Oberflächen glatter als 0.3 nm in weniger als einer Sekunde. Dabei reicht der erfasste Streuwinkelbereich von weniger als 10° um den spekularen Reflex aus, um Rauheitsspektren in einem Ortsfrequenzbereich von eineinhalb Dekaden zu analysieren. Darüber hinaus wurden Streulichttheorien sowie deren Einsatzgrenzen für die Spezifikationen des realisierten Streulichtensors untersucht.

Die mit neu entwickelten Analysemethoden aus Sensormessungen gewonnenen Strukturinformationen ermöglichen insbesondere eine zeiteffiziente Charakterisierung anisotroper Oberflächenstrukturen. Darauf aufbauend konnten die charakteristischen Strukturen von Fertigungsverfahren wie Diamantdrehen oder magnetorheologischem Polieren untersucht und verglichen werden.

Durch die Implementierung von zwei Beleuchtungskanälen sowie die Anwendung von Rauheitsmodellen konnte die Rauheitsentwicklung von Titanschichten untersucht werden. Insbesondere wurden sowohl der Übergangsbereich von Substrat- zu Schichtrauheit als auch die intrinsische Rauheitsstruktur der Schicht erfasst, wobei sogar eine höhere Datengüte erzielt wurde als mit konventionellen topographiebasierten Verfahren.

Ein Streulichtmodell für ein Notchfilter-Schichtsystem wurde durch Messung und Modellierung von Rauheit und Streulicht erarbeitet. Dabei fiel eine vorteilhafte Reduktion des Streuverlusts bei Beleuchtung des Filters von der Substratseite auf, deren Ursachen aufgeklärt werden konnten. Auf Basis des Modells wurden zusätzlich Anwendungsszenarien für die sensorbasierte in-line Charakterisierung des Filters erarbeitet und demonstriert.

Die Klassifizierung von Oberflächendefekten mittels Streulichtsensor konnte erfolgreich demonstriert werden. Dazu wurden mit einer kombinierten Anordnung von Streulichtsensor und Weißlichtinterferometer charakteristische Streulichtverteilungen mit den zugehörigen Defekttopographien verglichen. Zusätzlich wurden in experimentellen und modelltheoretischen Untersuchungen die Zuverlässigkeit der erarbeiteten Prozedur ermittelt.

Ehrenwörtliche Erklärung

Ich erkläre hiermit ehrenwörtlich, dass ich die vorliegende Arbeit selbstständig, ohne unzulässige Hilfe Dritter und ohne Benutzung anderer als der angegebenen Hilfsmittel und Literatur angefertigt habe. Die aus anderen Quellen direkt oder indirekt übernommenen Daten und Konzepte sind unter Angabe der Quelle gekennzeichnet.

Bei der Auswahl und Auswertung folgenden Materials haben mir die nachstehend aufgeführten Personen in der jeweils beschriebenen Weise entgeltlich/unentgeltlich geholfen:

1. Dr. Luisa Coriand, Tanja Niederhausen, Christian Wiede, Nadja Felde, Anne-Sophie Muntzer, Torsten Leichsenring (alle Fraunhofer IOF, Jena): AFM und WLI Messungen, außer Abb. 6.30
2. Torsten Leichsenring: Untersuchungen zur Anwendung von Belichtungsreihen und zur Implementierung des zweiten Beleuchtungskanal für Rauheitsmessungen im Rahmen einer von mir betreuten Praktikums- und Bachelorarbeit an der Fachhochschule Jena
3. Thomas Stemplewitz (geb. Brückner): Erste Labortests des Sensorkonzepts und erste Rauheitsmessungen im Rahmen einer von mir betreuten Diplomarbeit an der Fachhochschule Jena
4. Matthias Hauptvogel und Matthias Opel (Fraunhofer IOF, Jena): Implementierung einer Programmbibliothek zur Ansteuerung der CMOS-Matrix
5. Matthias Opel (Fraunhofer IOF, Jena): Implementierung einer speziellen Realisierung des Sensorkonzepts für ARS Messungen in Transmission
6. Christian Wiede (Fraunhofer IOF, Jena): Spektralphotometermessungen, Abb. 6.16 und 6.18
7. Dr. Sergiy Yulin (Fraunhofer IOF, Jena): XRD-Messungen an Titanschichten
8. Thomas Müller (Fraunhofer IOF, Jena): Herstellung von Titanschichten
9. Ralf Steinkopf (Fraunhofer IOF, Jena): Herstellung diamantgedrehter Oberflächen
10. Matthias Beier, Roman Loohse, Marcus Trost (Fraunhofer IOF, Jena): Herstellung MRF bearbeiteter Nickeloberflächen
11. Dr. Stefan Jakobs und Jan Broßmann (Optics Balzers Jena GmbH): Bereitstellung des Notchfilters
12. Ulf Hallmeyer und Birgit Walter (Hellma Optik Jena GmbH): Bereitstellung des Defektnormals, der Zylinderlinse und von Substraten

Teilergebnisse der vorliegenden Arbeit wurden bereits in den nachfolgend genannten Artikeln veröffentlicht:

- T. Herffurth, S. Schröder, M. Trost, A. Duparré, and A. Tünnermann, "Comprehensive nanostructure and defect analysis using a simple 3D light-scatter sensor," Appl. Opt. 52 , 3279–3287 (2013).
Grundlagen des Streulichtensors, Rauheitsmessungen an ausgewählten Proben sowie Untersuchungen von Defekten
- M. Trost, T. Herffurth, S. Schröder, A. Duparré, M. Beier, S. Risse, A. Tünnermann, and N. Böwering "In situ and ex situ characterization of optical surfaces by light scattering techniques," Opt. Eng. 53, 092013-1-6 (2014).
Untersuchungen von MRF-polierten Oberflächen
- T. Herffurth, M. Trost, S. Schröder, K. Täschner, H. Bartzsch, P. Frach, A. Duparré, and A. Tünnermann, "Roughness and optical losses of rugate coatings," Appl. Opt. 53 , A351–359 (2014).
Vorstellung und Anwendung des kombinierten PSD Wachstumsmodells sowie Anwendung des Modells für Volumenstreuung in Schichtsystemen

Weitere Personen waren an der inhaltlich-materiellen Erstellung der vorliegenden Arbeit nicht beteiligt. Insbesondere habe ich hierfür nicht die entgeltliche Hilfe von Vermittlungs- bzw. Beratungsdiensten (Promotionsberater oder andere Personen) in Anspruch genommen. Niemand hat von mir unmittelbar oder mittelbar geldwerte Leistungen für Arbeiten erhalten, die im Zusammenhang mit dem Inhalt der vorgelegten Dissertation stehen.

Die Arbeit wurde bisher weder im In- noch im Ausland in gleicher oder ähnlicher Form einer anderen Prüfungsbehörde vorgelegt.

Die geltende Promotionsordnung der Physikalisch-Astronomischen Fakultät ist mir bekannt.

Ich versichere ehrenwörtlich, dass ich nach bestem Wissen die reine Wahrheit gesagt und nichts verschwiegen habe.

Jena, den

Tobias Herffurth

Danksagung

An dieser Stelle möchte ich all denjenigen danken die direkt oder auch indirekt zur Entstehung dieser Arbeit beigetragen haben.

Herrn Prof. Dr. Andreas Tünnermann gilt mein Dank für die motivierenden Diskussionen während der Betreuung in meiner Promotionszeit. Seine konstruktive Kritik und seine fachlichen Anregungen waren wesentliche Voraussetzung für das Zustandekommen dieser Arbeit.

Mein besonderer Dank gilt Frau Dr. Angela Duparré, der Leiterin der Gruppe Oberflächen und Schichtcharakterisierung am Fraunhofer IOF. Sie gab mir die Möglichkeit zur Bearbeitung dieses interessanten Themas unter hervorragenden Bedingungen und hat mich während der Arbeit am Thema durch stete Verbesserungsvorschläge unterstützt und es immer wieder geschafft, mich mit Ideen und Impulsen neu zu motivieren.

Ebenso möchte ich Dr. Sven Schröder, Marcus Trost, Matthias Hauptvogel und Dr. Alexander von Finck danken, die stets ein offenes Ohr und Auge für die Feinheiten von Streulicht hatten und in geduldigen Gesprächen hilfreich zu dieser Arbeit beitrugen.

Mein Dank gilt außerdem den Kollegen Dr. Luisa Coriand, Nadja Felde, Christian Wiede und Dr. Sergiy Yulin die durch zahlreiche Messungen mit AFM, WLI, Spektralphotometer, und XRD sowie den zugehörigen Auswertungen ihren Beitrag zu dieser Arbeit geleistet haben. Weiterhin danke ich den Mitarbeitern am Fraunhofer IOF sowie der gesamten Abteilung „Optische Systeme“ unter Leitung von Dr. Gunther Notni für das angenehme Arbeitsklima.

Bedanken möchte ich mich auch bei den Kollegen und Partnern die durch die Fertigung und Bereitstellung von Testproben die Arbeit in der vorliegenden Form ermöglicht haben: Thomas Müller, Ralf Steinkopf, Matthias Beier und Roman Loohe, (Fraunhofer IOF, Jena); Dr. Stefan Jakobs und Jan Broßmann (Optics Balzers Jena GmbH); sowie Ulf Hallmeyer und Birgit Walter (Hellma Optik Jena GmbH).

Mein herzlichster Dank gilt meiner Partnerin Jana und meiner Familie für den Zusammenhalt und die Kraft, die ich immer wieder neu aus allem, was wir gemeinsam geschaffen und geschafft haben, gewinnen konnte.